Title
High Frequency Dynamics of Magnetic Tunnel Junctions

Author
Rajapakse, Rajapaksayalage Nayana

Publication Date
2020

Peer reviewed|Thesis/dissertation

UNIVERSITY OF CALIFORNIA

Los Angeles

High Frequency Dynamics of Magnetic Tunnel Junctions

A dissertation submitted in partial satisfaction

of the requirements for the degree

Doctor of Philosophy in Physics

by

Rajapaksayalage Nayana Rajapakse

2020

ABSTRACT OF THE DISSERTATION

High Frequency Dynamics of Magnetic Tunnel Junctions

by

Rajapaksayalage Nayana Rajapakse
Doctor of Philosophy in Physics
University of California, Los Angeles, 2020
Professor HongWen Jiang, Chair

Magnetism has been utilized since ancient civilizations to build tools for day to day life for example, magnetic compass. Understanding of nature behind magnets has ever since evolved passing significant milestones such as, discovery of interplay between magnetism and electricity leading to invention of electric motor and dynamo and, microscopic insight developed following discovery of quantum mechanics. About twenty years ago we passed arguably the most recent milestone with the prediction of the ability to manipulate a nano sized magnet with the aid of the spin of an electronic current. With the advent of magnetic tunnel junctions (MTJ), one of the main applications of this has been spin transfer torque nano oscillators (STNO) that have attracted great attention. Recently, a new emerging field regarding magnetic skyrmions in MTJs has shown even more promising aspects such as higher energy efficiency for real world applications. In the first half of this thesis, we present a tri-layer MTJ based STNO offering 6 GHz microwave emission for both current polarities at zero external magnetic field which is the highest frequency achieved in absence of any bias field to-date, to the best of our knowledge. We have investigated into spin dynamics of this STNO discussing about out of plane (OOP) precessions along with micromagnetic simulations. In the second half of this thesis, we present observation of skyrmionic signature in an MTJ at cryogenic temperature producing random telegraph signal (RTS). We have studied the dependencies of this RTS upon various physical parameters. RTS seen in MTJs involving

ferromagnetic states has attracted attention in the research community as it is an ideal candidate to realize neuromorphic computers which are inspired on human brain offering tremendous improved performance in specific tasks over conventional boolean computing. We believe this investigation into RTS involving skyrmionic states in an MTJ will further electrify this on going expedition.

The dissertation of Rajapaksayalage Nayana Rajapakse is approved.

Brian Christopher Regan

Greg Carman

HongWen Jiang, Committee Chair

University of California, Los Angeles

2020

To my Parents

Table of Contents

List of Figures

Preface

I developed the passion for physics in middle school and since then I am lucky to have met many people in my life who have inspired me, influenced me, guided me and been there for me whenever I needed help. Herewith I would like to make this an opportunity to express my sincere gratitude for those people who have made an impact in my adventure so far making this thesis possible.

I began to see myself as a physicist when I met Sunil De Alwis, my middle school science teacher whom without any doubt the best teacher I have had in my life. I am deep heartedly thankful to you for setting the tone of my life at such an early stage. The guidance I was privileged to receive from my teachers during my undergraduate studies at University of Colombo, Sri Lanka proved to be priceless that molded me to a prospective student allowing to get admitted to UCLA. For mentoring and developing me as a physicist, herewith I want to thank Dr. S.R.D. Rosa, Dr. W.M.K.P. Wijayaratna, Dr. D.D.N.B. Daya, Dr. R.V. Coorey, Dr. S. Jayanetti, Dr. U. Sonnadara, Dr. C.M. Edirisinghe, Dr. M.K. Jayananda, Dr. I.M.K. Fernando, Dr. T.R. Ariyaratne and Dr. K.A.I.L. Gamalath.

I would like to thank my PhD adviser at UCLA Dr. HongWen Jiang for the immense support given during past six years for teaching, guiding, motivating and mentoring me to develop as a physicist. I am very grateful for your help, understanding, patience and kindness during difficult times when I found myself struggling both as a PhD student and a person.

I joined my research lab in early 2015 with no prior knowledge of spintronics and magnetic tunnel junctions which became the primary focus of my thesis. I thank Dr. Zhongming Zeng for helping me out to learn the material fast and guiding me throughout the past six years. In addition, I express my gratitude towards my thesis committee members, Dr. Brian Christopher Regan, Dr. Karoly Holczer and Dr. Greg Carman for their precious time, guidance and valuable suggestions since my advancement to candidacy in 2016.

During my time in lab, I am lucky to have had the assistance of my fellow labmates in learning lab procedures and building experimental setups. I would like to thank Nicholas

Evan Penthorn, Blake Freeman, Joshua Schoenfield and John Dean Rooney in helping me with learning, dicing wafers, wirebonding, plasma etching, cryogenic refrigerator maintenance, MATLAB instrumentation control and much more without which my experiments would not have been possible. I want to deliver my special thanks to Nicholas Evan Penthorn for collaborating with me for the skyrmion project mainly taking care of micromagnetic simulations. In addition, I want to express my sincere gratitude towards Niels Thompson and Gerald Yan for their valuable help in building the homemade skyrmion cryogenic setup and its electromagnet expediting the process for its timely completion.

When I first arrived in Los Angeles, I was a complete stranger to the United States also was about to start a brand new life where I would be living at such a distance from home for the first time in my life. I consider myself very lucky that I met wonderful new friends Amila Ariyarathne, Dilhara Ranasinghe and Dayan Wickramarathne at UCLA who helped me during transition and provided support throughout this time so far. I want to express my heartiest gratitude to my best friends in Sri Lanka Osanda Sakalasooriya and Ishara Diaz for all the support provided regardless being thousands of miles away. Thank you for all the long conversations we had that I desperately needed when the times were tough and I found myself emotionally struggling. I also express my heartiest gratitude towards UCLA Dashew center and specially its Global Siblings Program from which I made hundreds of long lasting friendships leaving my time at UCLA memorable.

Last but not least, I want to mention, I am in forever debt to my wonderful parents, Wimaladasa Rajapakse and Indrani Rajapakse for all the kind help since the day I was born. Thank you for raising me and being there for me through all hardships in my life so far.

Vita

2008–2013	B. Sc. (Physics), University of Colombo, Sri Lanka.
2013–2020	Ph. D. candidate (Physics), University of California Los Angeles.
2013–2017	Teaching Assistant, Department of Physics and Astronomy, UCLA.
2018–2020	Graduate Student Researcher, Department of Physics and Astronomy, UCLA.

Publications

"High Frequency Microwave Emission of a Tri-Layer Magnetic Tunnel Junction in the Absence of External Bias-Magnetic Field" **R. Nayana Rajapakse**, Z. M. Zeng and H. W. Jiang - arXiv: 2001.04539 - submitted to PR Applied (in review).

"Random Telegraph Signal Between Topologically Distinct States in a Magnetic Tunnel Junction" **R. Nayana Rajapakse**, N. E. Penthorn, X. Hao, Z. Wang, Y. Huai and H. W. Jiang - in preparation

CHAPTER 1

Introduction

1.1 Background

Use of charge of an electron has been exploited for centuries starting from electrical circuits to electronic circuits in the later twentieth century with the advent of semiconductor devices. Spintronics is a relatively new emerging field where this prevailing concept of charge based manipulation is extended to utilize the intrinsic spin of the electron as well. With more control on electron transport, this has paved way to promising novel avenues to achieve groundbreaking real world applications in computer magnetic universal memory, microwave communication, magnetic and RF sensors, unconventional neuromorphic computing and much more.

1.1.1 Giant Magnetoresistance

The key idea for spintronic devices is to make use of the spin dependent transport of electrons through magnetic materials. Mutual interaction of the spin of an electron current with local magnetic moments of the medium creates variations in the transport rate hence causing changes in its electrical resistance which can then be integrated into existing electronic circuit design concepts. Dependence of electrical resistance of a magnetic material subjected to an external magnetic field was first discovered about 150 years ago by W. Thomson and L. Kelvin which was named as anisotropy magnetoresistance (AMR) and had been used in applications for example, early magnetic read heads of computer hard disks. In 1988 two research groups lead by Albert Fert [1] and Peter Grünberg [2] independently

discovered very large magnetoresistance effects in Fe/Cr multilayers which was then coined the term, giant magnetoresistance (GMR) reflecting its significant improvement over AMR. A GMR device is a multilayer device with alternating layers of a ferromagnetic metal (for example, Fe or Co) and a non- magnetic metal (for example, Cr or Cu) with layer thickness in the order of a couple of nanometers. In such devices electrical resistance depends on the relative magnetization orientations of adjacent ferromagnetic layers (separated by non-magnetic layers) due to spin-dependent scattering [21, 22, 23]. The resistance is low where the magnetizations are parallel while it is high when neighboring magnetizations are anti-parallel. The first reported experimental results on GMR are shown in Fig. 1.1. Fig. 1.1.a presents GMR observed on an Fe/Cr/Fe multilayer structure (more than three layers) measured at 4.2 K showing a change in magnetoresistance up to 80%. Fig. 1.1.b presents GMR observed on an Fe/Cr/Fe tri-layer measured at room temperature. This first report of GMR for a tri-layer device at room temperature produced only 1.5% of a change in resistance which was significantly improved in subsequent attempts.

Discovery of GMR had an instant impact on technological applications that it facilitated high density magnetic storage devices i.e. computer hard disks, Fig. 1.1.c (image after [3]), which was otherwise impossible with the prevailing AMR sensors. Albert Fert and Peter Grünberg shared the Nobel Prize for Physics in 2007 for their pioneering work that reignited the purse in magnetoresistance devices [24].

1.1.2 Spin Transfer Torque

Initially, the magnetization of ferromagnets of GMR devices were manipulated with external magnetic fields which had its own drawbacks mainly regarding scalability of the devices. In 1996 a ground breaking theoretical prediction was made by J. C. Slonczewski [25] and L. Berger [26] proposing to use spin momentum transfer of a spin polarized electron current to control the magnetization of a ferromagnet. The basic concept of their prediction is as follows. In general, individual spins of electrons in an electric current are arbitrary oriented leaving a zero net spin polarization. This is directly analogous to the polarization concept of

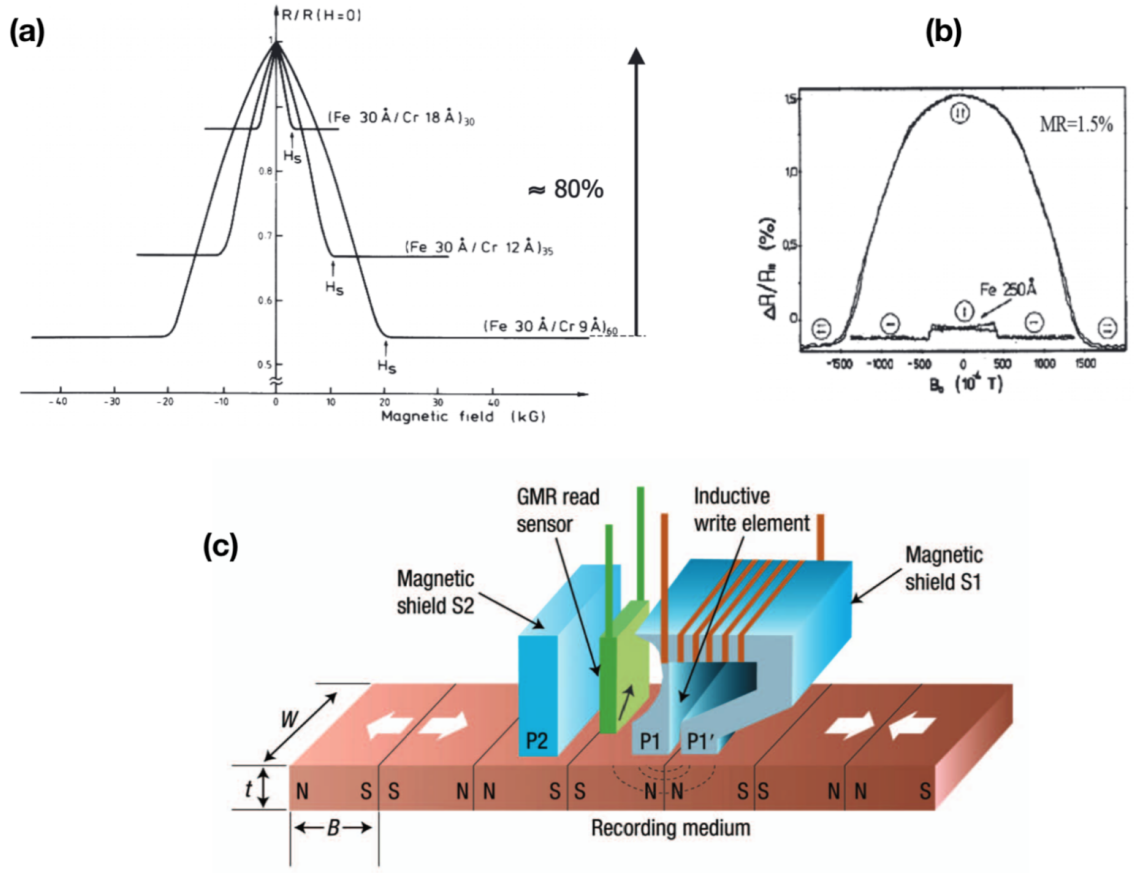

Figure 1.1: Giant Magnetoresistance (GMR) (a) First out of the two historic reports on GMR presenting the observed giant change in resistance on magnetic field of a Fe/Cr multilayer structure at 4.2 K (after M. N. Baibich et al. 1988 [1]) (b) Second out of the two historic reports on GMR presenting the observed change in resistance on magnetic field of a Fe/Cr/Fe tri-layer structure at room temperature. (after G. Binash et al. 1989 [2]) (c) Direct application of GMR in a computer hard disk drive leading to much higher storage density than that by prevailing AMR senses (after C. Chappert et al. 2010 [3]); one of the main influences behind the Nobel price for physics in 2007 shared by Albert Fert and Peter Grünberg.

electromagnetic waves. However, when such spin unpolarized electron current passes through a ferromagnet, the spins of the electrons tend to align with latter's magnetization leaving a net spin polarization. When these spin polarized electrons enter a second neighboring ferromagnet, spin momentum carried by electrons will be transferred to the magnetic moment of the latter exerting a torque which was named spin transfer torque (STT). This phenomenon is illustrated in Fig. 1.2.a. (image after [3]). Furthermore, as an extension to this formalism, GMR can be thought of as the reaction of the STT as required by Newton's third law in which case, STT and GMR can be considered as the two sides of the same coin. This newly suggested STT in nature would either reinforce or counteract the intrinsic damping depending on the direction of the current and can be visualized as illustrated in Fig. 1.2.b where the image is adapted from [4]. With the presence of magnetic anisotropy, STT is neither exactly parallel nor anti-parallel to the damping torque (i.e., not always collinear) however, still can be understood as either strengthening or weakening the damping effect on average per cycle. When the direction of the electric current is such that STT adds on to damping effect, the magnetization (starting with a tilt away from the equilibrium) would be brought back to its equilibrium. For the other current direction, STT would counteract the damping effect and can lead to three different outcomes as shown in Fig. 1.2.c. For low current, magnitude of STT would be less than that of damping leaving a net damping effect that would bring the magnetization back to its equilibrium. As the current is increased, magnitude of the STT will be increased as well comparable to that of damping eventually canceling it out. In this situation magnetization will have a persisting tilt angle away from equilibrium hence undergoing Larmor precessions. In this precessional regime, energy supplied by STT is dissipated through damping on average. When the current is further increased, STT will rotate the magnetization to a higher angle leading to a complete reorientation referred to as a switching event.

Soon following these predictions, first experimental evidence were reported on STT in point-contact nano devices (point electrode in contact with a thin film) [27, 28] and in spin valves (a tri-layer pillar device with two ferromagnets sandwiching a non-magnetic spacer)

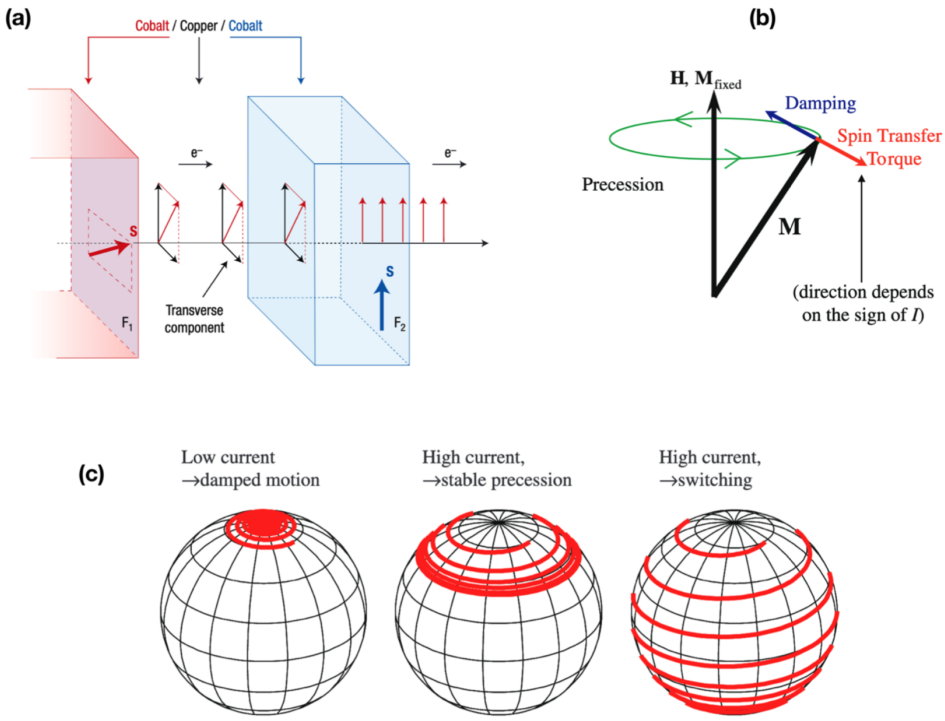

Figure 1.2: Spin transfer torque (STT) as a novel way of magnetization manipulation. (a) Spin transfer torque by an electron current (after C. Chappert et al. 2010 [3]). Electrons passing through the first ferromagnet get spin polarized and enter the second ferromagnet exerting a torque on the latter's magnetization. In attempt to modify the spin of the incoming electrons, second ferromagnet experiences a torque as the reaction (Newton's third law). (b) Spin transfer torque acting on a magnetization in the context of other torques. (after D. C. Ralphs and M. D. Stiles 2008 [4]). For a specific current direction, STT can counteract damping bringing the magnetization away from the local magnetic field resulting in Larmor precessions of the magnetization around the local field. (c) Possible outcomes of STT acting on a magnetization as an anti-damping (counteracting the damping) torque (after D. C. Ralphs and M. D. Stiles 2008 [4]). For illustration purposes, the evolution of the magnetization starting from a finite tilt away angle for different current (hence STT) magnitudes are shown.

[29, 30]. Subsequently more comprehensive observations and studies were reported on STT induced magnetization switching and steady state precessions in microwave frequency range paving way to extensive research in the two decades to follow.

1.2 Magnetic Tunnel Junctions

Following the discovery of GMR in 1988 in Fe/Cr multilayers, a more practically favorable design named spin valve was invented with sufficient GMR [31]. A spin valve can conceptually be considered as a tri-layer device where two ferromagnets sandwiching a non-magnetic metal. Coercivity field (magnetic field required to switch the magnetization of a ferromagnet) of one of the ferromagnets is made to be higher than that of the other where the former is referred to as the fixed layer while the latter is referred to as the free layer. As suggested by the names, under a moderate magnetic field, the magnetization of the free layer can be manipulated while that of the fixed layer left unaffected. This extra stiffness for the fixed layer is achieved by increasing its physical size and having it magnetically pinned to additional layers. Consisting of just three active layers (free, fixed and the spacer layers), a spin valve is the most minimal form of a GMR device producing low and high resistance states when the magnetizations of the two ferromagnets are in parallel and anti-parallel respectively.

However, these metallic spin valves produced low electrical resistance in general and specifically low GMR ratio (ratio between the two resistances corresponding to parallel and anti-parallel configurations) leading to poor signal to noise ratio for applications. Due to these reasons spin valves were eventually replaced with magnetic tunnel junctions (MTJ) where the non-magnetic spacer between the ferromagnets is now an insulator instead of a metal. First MTJs were made with AlO (alumina) as the insulating barrier [32, 33] after which MgO was adopted [34, 35]. AlO being amorphous in nature had less performance compared to crystalline MgO where the crystal alignment was possible which led to improvement in performance. This also enabled direct theoretical modeling for MgO based MTJs allowing both experimental and theoretical research to progress in unison [36, 37]. In these

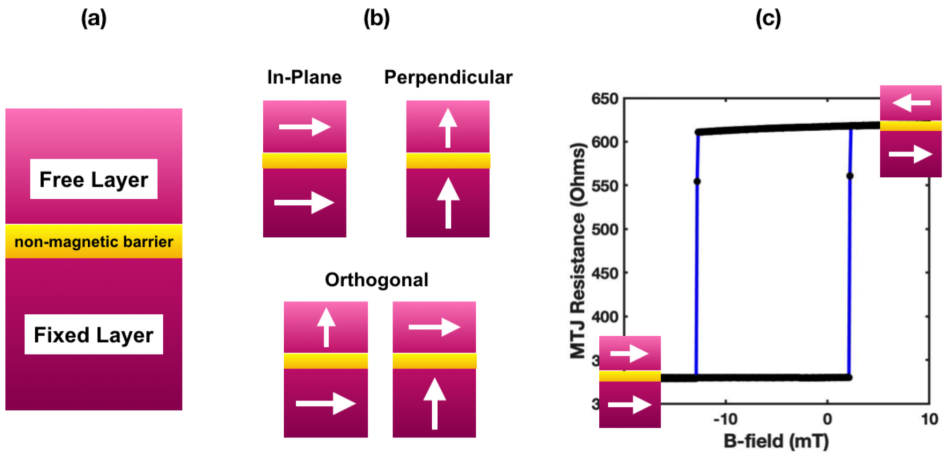

Figure 1.3: Anatomy of a magnetic tunnel junction (MTJ). (a) Three active layers of a magnetic tunnel junction where top and bottom ferromagnetic layers sandwiching the non-magnetic middle insulating layer. Coercivity field of the fixed layer is engineered to be greater than that of free layer by increasing its physical size and having it pinned to adjacent magnetic layers (not shown). Due to this reason, at moderate magnetic fields, magnetization of the free layer can be manipulated while that of the fixed layer left unaffected. (b) Different magnetization structural designs for MTJs where each free and fixed layers can possess either an in-plane or a perpendicular (out-of-plane) easy-axis. In-plane and perpendicular structures are those with both free and fixed layer magnetizations are in-plane and perpendicular to plane respectively. Orthogonal structures are in which free and fixed layer magnetizations are mutually perpendicular and can have two designs as shown. (c) Easy-axis magnetoresistance loop for an in-plane device. Low and high resistance states are when the two magnetizations are in parallel (P-state) and in anti-parallel (AP-state) respectively as demonstrated with insets.

MTJs electrical current is due to a quantum mechanical tunneling process [38] producing a higher device resistance and significant differentiation between parallel and anti-parallel resistance states. Since this magnetoresistance is coursed by a spin dependent tunneling compared to spin dependent scattering in GMR, this was subsequently named as tunnel magnetoresistance (TMR).

Fig. 1.3 presents the fundamentals of an MTJ where those for a spin valve will be similar except the difference of having a metallic spacer between the two ferromagnets as shown in Fig. 1.3.a. Initial spin valves and MTJs had in-plane anisotropy induced by shape for both fixed and free layers however, with new techniques to induced perpendicular anisotropy [39, 40] allowed multiple structural designs as indicated in Fig. 1.3.b. Here each layer can either have in-plane or perpendicular anisotropy leading to four different configurations. When both layers have in-plane anisotropy the devices are called in-plane devices while devices with both layers possessing perpendicular anisotropy are called perpendicular devices. The devices with layers having magnetizations mutually perpendicular are called orthogonal devices and can be in two different structures as seen in the bottom panel of Fig. 1.3.b. Each of these structures have their own spin-dynamics properties that vary both qualitatively and quantitatively. Fig. 1.3.c. presents an example easy-axis magnetoresistance loop for an in-plane device where the device resistance is measured under a fixed bias current as the applied magnetic field is varied alone the free layer's easy-axis. Insets are included to demonstrate the magnetization configuration for P and AP-states. Higher resistance state (AP-State) corresponds to where the free layer magnetization is anti-parallel (AP) to that of the fixed layer while the lower resistance state (P-State) corresponds to where the free layer magnetization is parallel to that of the fixed layer.

1.3 Applications

Magnetic tunnel junctions have drawn tremendous attention for the last decade due to its promising applications in computer and communication technology. A basic way to have an idea about what it has to offer is to compare it with the working regions of a conventional

transistor. A transistor has three regions namely cutoff, active (or linear) and saturated region. Among these options, transistors are employed in cutoff and saturated regions to implement binary circuits for boolean computing while the active or the linear region is utilized to implement other applications including oscillators. Compared to a transistor's cutoff and saturated states, P and AP-states of an MTJ can be utilized to implement binary "bit-0" and "bit-1" which can be switched back and forth as shown in Fig. 1.2.c third panel. On the other hand, for oscillators, active region of a transistor can be compared to the stable precessional region of an MTJ as shown in the second panel of Fig. 1.2.c. Recently a new interest in research has started to emerge involving magnetic skyrmions in ferromagnetic systems where whirl of spin configurations are stabilized using breaking of inversion symmetry. Although this field took off starting with work done on thin magnetic films [41, 42], MTJs were considered later on and have shown to be a promising candidate for skyrmion applications [43, 10]. A brief introduction for each of these applications are presented as follows.

1.3.1 Spin Transfer Torque Magnetic Memory

After the discovery of GMR and invention of spin values, prototype magnetic memories (for computer applications) were made where bits stored in spin valves were switched using the Oersted field generated by the bit and word lines of the memory architecture [44]. However this suffered with significant scaling problems and was not pursued much until the prediction [25, 26] and experimental demonstration of STT [27, 28, 29, 30]. Since then STT has been used to switch bits stored in spin valves (eventually MTJs) which solved the prevailing scaling problem significantly as STT is a local effect in contrast to an external field manipulation. Successful realization of a spin transfer torque magnetic random access memory (STT-MRAM) can potentially replace existing dynamic random access memory (DRAM) of computers. Since STT-RAM being non-volatile (does not require power to hold up memory) and offering comparable switching speeds with existing DRAM, will be able to replace both RAM and main storage (example, hard disk or solid state drive) of a conventional computer

leading the path to a universal memory directly integrated to the central processing unit (CPU) [45]. This offers the opportunity to eliminate limitations of existing Von-Neumann architecture where data transfer speed between CPU and RAM has become the bottleneck for speed. Furthermore, a non-volatile working memory directly contributes towards energy efficiency leading to longer battery life on consumer electronic devices or to reduce device physical size by using a smaller battery.

Basic operation of an MTJ for memory application is illustrated in Fig. 1.4. P-state and AP-states can be utilized to represent "bit-0" or "bit-1" (or vice-versa by choice) in between which the device can be switched with current pulses with different polarities as shown in Fig. 1.4.a. To switch from AP to P-state, a pulse of electrons traveling from fixed to free layer is used where electrons will first get spin polarized along the fixed layer and then exert a torque in the same direction upon entering the free layer. On the other hand, to switch from P to AP-state, an electron pulse where electrons traveling from free layer to fixed layer is used. In this situation electrons reflected back in to the free layer from the fixed-layer/spacer interface (which is a hard reflection) will carry spin momentum opposite in direction to fixed layer's magnetization that will rotate free layer magnetization to the AP-state. Fig. 1.4.b illustrates multiple MTJs used in a memory grid of word and bit lines. To record a bit, a high current pulse above the switching critical current (device dependent) is used while to readout a bit, a low test current is used to probe device resistance.

1.3.2 Spin Transfer Torque Oscillators

Other valuable use of MTJs is as a spin transfer nano oscillator (STNO) [25, 26, 46, 5]. As shown in Fig. 1.2.b, STT can counteract the intrinsic damping torque for the right current direction allowing a persistent tilt angle. In such situation the magnetization of the free layer will undergo Larmor precessions as demonstrated in the middle panel of Fig. 1.2.c. In these precessions the energy dissipated by damping will be replaced by the energy input from STT on average. These precessions are usually in the microwave range (a couple of GHz) during which the angle between free layer and fixed layer magnetizations is continuously

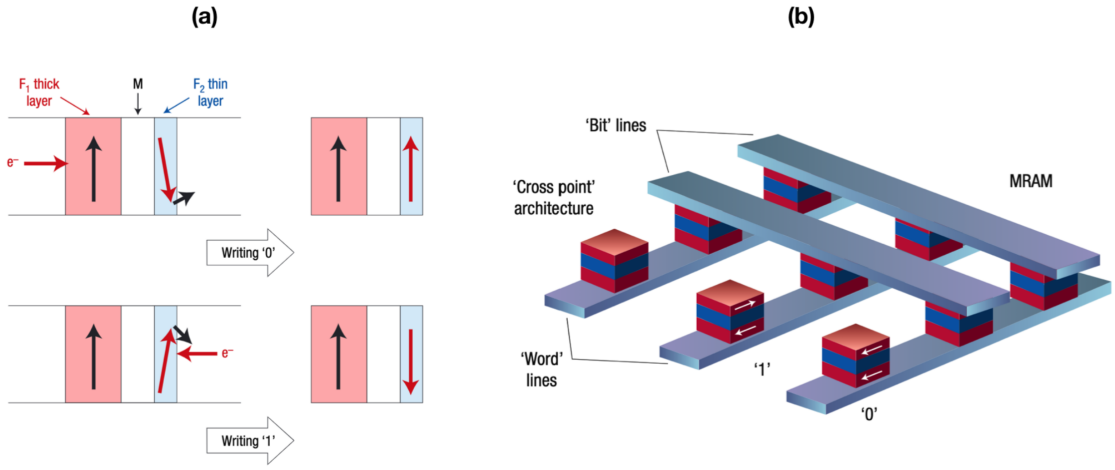

Figure 1.4: Controlling magnetic bits from spin transfer torque for magnetic random access memory (MRAM). (after C. Chappert et al. 2007 [3]) (a) Switching of the free layer magnetization from anti-parallel (AP) to parallel (P) (top panel) and from P to AP (bottom panel). In the top panel, when electrons pass through the fixed layer to a free layer (in AP-state), a spin torque in the direction of fixed layer magnetization is exerted on the free layer leading to a 180 degree rotation into P-state. To switch from P to AP-state (bottom panel), an electron current in the opposite direction is required where the reflected (a hard reflection) electrons from the fixed-layer/spacer interface will exert a spin torque on the free layer in the opposite direction leading to a P to AP switching. (b) Conceptual design of an MRAM with multiple STT devices probed with word lines and bit lines. AP-state with high resistance can be assigned 'bit-1' while the P-state with lower resistance can be assigned 'bit-0' (by choice). To write a bit, a high current pulse (above the critical current) is used while to readout, a small test current is used to probe the resistance.

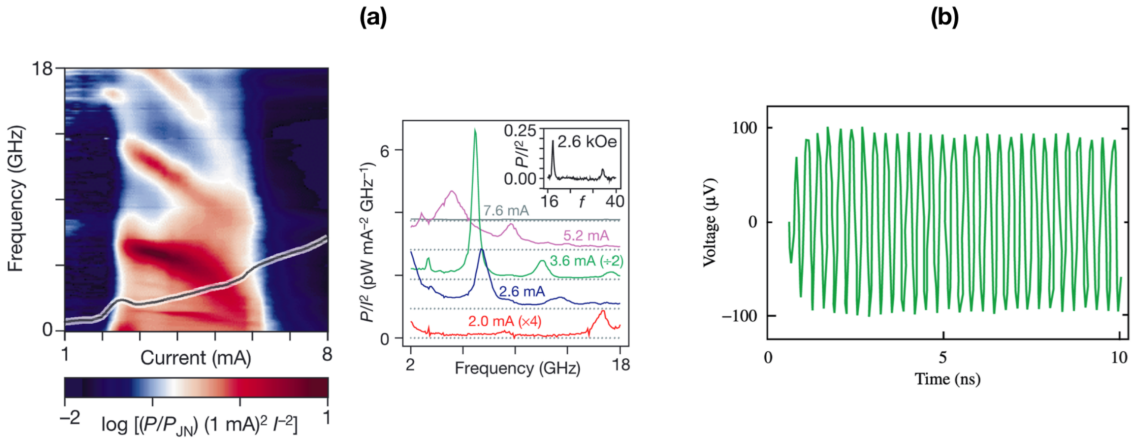

Figure 1.5: Microwave generation of a spin transfer nano oscillator (STNO). (a) First report of microwave emission from an STNO measured in frequency domain. (after S. I. Kiselev et al. 2003 [5]) (b) First report of microwave emission from an STNO in time domain. (after I. N. Krivorotov et al. 2005 [6])

changing. This change in relative orientation of the magnetizations of free and fixed layers will be reflected in the device resistance due to TMR and will generate an oscillatory voltage signal due to the applied current (Ohms law) which can then be harvested as the microwave signal produced by the MTJ.

Fig. 1.5 presents the first observations of microwave generation of STNOs. Fig. 1.5.a is the first report of microwave emission recorded in frequency domain [5] while Fig. 1.5.b is the first microwave emission recorded in time domain [6]. Both work were reported on metallic spin valves but, MTJs producing microwave hold qualitative similar characteristics in general with much higher emission power. Initial STNOs required an external bias field for operation which was not favorable from a practical point of view. As the time progressed, with help of anisotropy engineering, operation of STNOs in absence of any external bias field were theoretically predicted [47, 48] and were realized [13, 17, 19, 14]. In fact, first of the two projects in this dissertation is a report of highest frequency achieved to date by an STNO without a bias field.

1.3.3 Magnetic Skyrmion Based Applications

Skyrmions were first proposed way back in 1962 by T. H. R. Skyrme in particle physics as a topologically stable solution to a certain field configuration [49]. A magnetic skyrmion is a nano scale spin texture that can be induced in magnetic materials that agrees with the topological properties of the original skyrmion predicted in particle physics. Such a magnetic skyrmion is localized whirl of the material spin configuration that mainly appears in two different types namely, Neel-type and Bloch type as shown in Fig. 1.6.a. (image adapted after [7]). In such circular skyrmions, magnetization at the center either points down or up and rotates to point in the opposite direction as moving radially outwards. In a Neel-type skyrmion this rotation is parallel to the radius (in comparison to a Neel-type domain wall) while for a Bloch-type skyrmion, this rotation is perpendicular to the radius (in comparison to a Bloch-type domain wall). Skyrmions possess an important characteristic topological charge that is quantized hence having the advantage of additional stability under topological protection. That is, for a continuous transition between two topologically distinct states (for example between a skyrmion and ferromagnetic state) is not possible with a continuous rotation of the local magnetization [50]. However in real systems where the medium size is finite, complete topological protection is not present instead, different states are separated by a finite energy barrier still offering high stability compared to topologically trivial states [9, 51].

Initial observations of magnetic skyrmions were made in single crystals [41, 42] and was explained by an asymmetric exchange action namely Dzyaloshinskii–Moriya interaction (DMI) [52, 53] which is originating from the absence of inversion symmetry in the crystal lattice due to spin-orbit coupling. Later on, it was discovered that skyrmions can be induced in ultrathin magnetic films epitaxially grown on heavy metals (for example Ir or Pt) where DMI is induced at the interface (interfacial-DMI) [9, 54]. Spacial distribution of magnetic skyrmions on such a thin film does depend on the strengths of DMI, exchange constant and any applied magnetic field leading three possible configurations namely, individual skyrmions, skyrmion lattice and spin spirals [55]. With minimal conditions individual

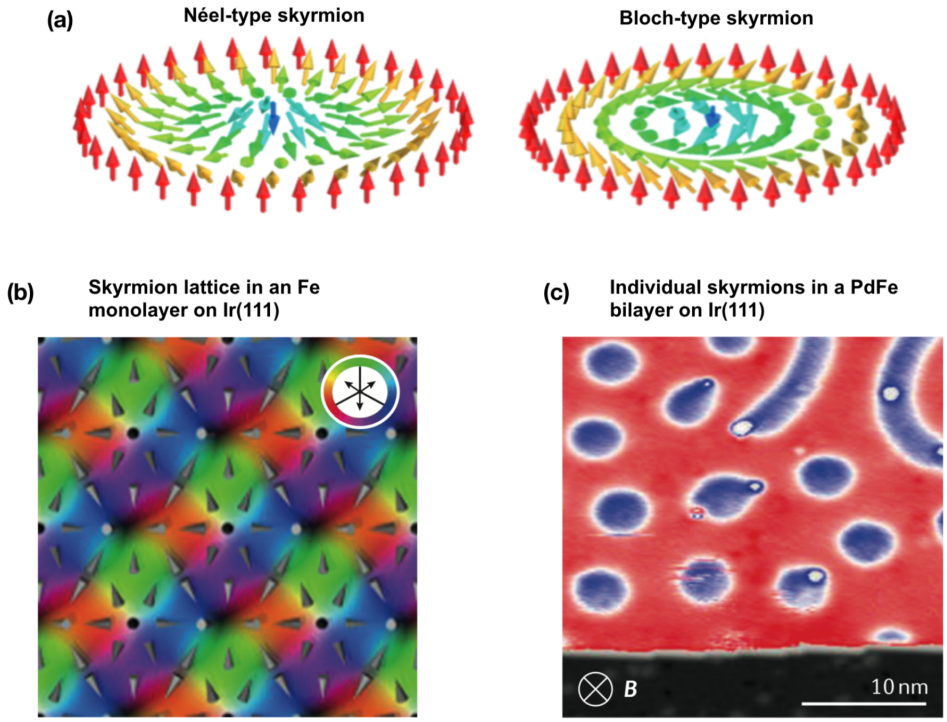

Figure 1.6: Magnetic skyrmions (a) Main two types of magnetic skyrmions, Neel-type and Bloch- type named reflecting the Neel-type and Bloch-type domain walls in the radial direction. (after K. Everschor 2012 [7]) (b) A Skyrmion lattice imaged with a spin polarized scanning tunneling microscope. The lattice is hosted on a monolayer of Fe grown on Ir(111). (after R. Wiesendanger et al 2016 [8]) (c) Individual skyrmions, hints of skyrmion lattice and spin spirals (top right corner) on a PdFe bilayer on Ir(111) imaged with a spin polarized scanning tunneling microscope. (after N. Romming et al 2013 [9])

skyrmions are formed and as those skyrmions are forced to pack closer to each other (for example by increase of DMI) individual skyrmions will first form a lattice and then eventually converting in to spin spirals. In Fig. 1.6.b., a skyrmion hexagonal lattice formed on a single layer of Fe grown in Ir(111) is presented where the observation was made by a spin polarized scanning tunneling microscope [8]. Fig. 1.6.c., presents an example of coexistence of individual skyrmions, some hints of a lattice and spin spiral which was observed on PdFe bilayer on Ir(111) again with a spin polarized scanning tunneling microscope [9].

Over the past decade, magnetic skyrmions have gained much attention for spintronic applications due to their energy efficient manipulation with smaller current densities compared to domain walls in ferromagnetic systems [56, 57]. Utilization of skyrmions for spintronic applications such as racetrack memory [58, 59, 60], logic gates [61], and artificial synapses for neuromorphic computing [62] have already been considered and have shown promising results. For such systems, MTJs have been considered as a solution to detection and creation of skyrmions. Computational studies have been reported on sole use of an MTJ to host and manipulate skyrmion states where it was shown to be more energy efficient by at least one order of magnitude compared to state-of-the-art STT magnetic memories [43].

Even though DMI has been a key ingredient of facilitating skyrmions in magnetic systems, evidence has been reported on the possibility of skyrmion creation and stabilization in confined ferromagnetic devices without any DMI present [63, 64]. Recently experimental observation of magnetic skyrmion signature at 4.2 K was reported [10] in a commercially available (Avalanche Technologies) MTJ with the structure shown in Fig. 1.7.a where no DMI is present. In this work the skyrmionic state was successfully created and manipulated with microwave current or with nanosecond range current pulses. Electrical detection of the skyrmion has been done in terms of DC resistance measurements and breathing modes [65] appearing on resonance spectrum. Under an RF stimulant (either microwave current or fast pulses) skyrmionic state is created inducing stepwise features in the magnetoresistance curve during AP to P-state transition as shown in Fig. 1.7.b. These step resistance values falling between AP-state resistance (highest) and P-state resistance (lowest) are called intermediate

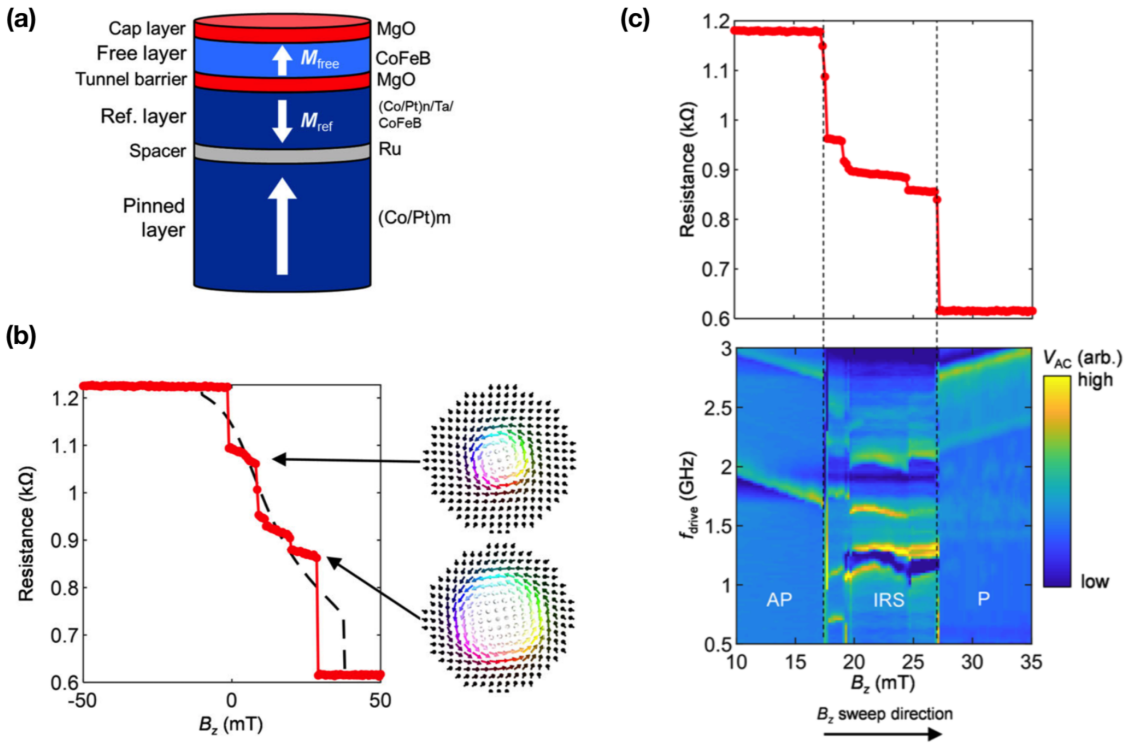

Figure 1.7: Experimental evidence of skyrmion signature in a magnetic tunnel junction without DMI. (after N. Penthorn et al. 2019 [10]) (a) Perpendicular MTJ design with a free layer lacking any heavy metal interface for interfacial-DMI. (b) Perpendicular magnetoresistance curve for AP to P transition of the device under an RF stimulant producing intermediate resistance states (IRS) in contrast to an otherwise abrupt transition. Insets demonstrate the suggested skyrmion formation responsible for IRS as produced by micromagnetic simulations. (c) Skyrmion signature in the resonance spectrum in the context of the magnetoresistance curve. For the regions of AP and P-states, Kittel like FMR lines are present while in the range corresponding to the IRS, skyrmion breathing mode like signature is present proving indirect evidence (compared to direct imaging) of the formation of a magnetic skyrmion.

resistance states (IRS) and have been formed only during AP to P transition. Resonance measurements conducted with simultaneously monitoring of DC resistance has shown appearance of skyrmion breathing modes directly corresponding to the IRS regions appearing on the magnetoresistive loop as shown in Fig. 1.7.c. When the device is in the ferromagnetic region (P or AP state), Kittel like modes are present and while during IRS, breathing modes are present. Micromagnetic simulations have reproduced these features with formation of a Bloch-type skyrmion that is shown to stabilize without DMI but with the aid of spatially non-uniform stray field originating from the fixed layer. Snapshots of simulated skyrmions are shown in the insets of Fig. 1.7.b, where the core size is dependent on the applied magnetic field changing the z-component of the residual magnetization causing the observed IRS.

The second out of the two projects presented in this thesis is based on this experiment where the work has been extended to higher temperatures (77 K and above). We have observed stochastic effects regarding formation of IRS with presence of random telegraph signal (RTS). RTS has been observed involving skyrmions [9] where the signal was generated due to switching between a skyrmion and a ferromagnetic state on a 2D film probed with a spin polarized scanning tunneling microscope. Motivated by these results we explored into the presence of RTS in our MTJ system which is presented in the second half of this thesis.

CHAPTER 2

Theoretical Background

2.1 Magnetoresistance

Magnetoresistance is the dependence of electrical resistance of a material on an external magnetic field. There are mainly three types of magnetoresistance phenomena namely, anisotropy magnetoresistance (AMR), giant magnetoresistance (GMR) and tunnel magnetoresistance (TMR). In the dawn of spintronics era, GMR devices had already taken off and eventually got replaced by TMR devices for their higher performance.

2.1.1 Giant Magnetoresistance

Giant magnetoresistance (GMR) is observed when two ferromagnets are separated by a thin nonmagnetic metallic spacer. GMR devices produce different resistance states depending on the relative magnetization orientations of their ferromagnets and can be explained by spin dependent scattering [21, 22, 23]. Electric current consisting of electrons with spin up and down can pass through the structure as demonstrated in Fig. 2.1. Depending on the relative alignment of an electron's spin to the magnetization of the path, it will experience a low (high) resistance if the spin is parallel (anti-parallel) to the local magnetization. The total electric current can be considered as the summation of the two parallel channels of spin up and spin down electrons that independently pass through the setup.

Fig. 2.1.a., illustrates such two channels of electrons traversing through a configuration where both ferromagnets are magnetized in the same direction (up). In such configuration spin up electrons will experience lower resistance (R_{low}) in both ferromagnets while spin

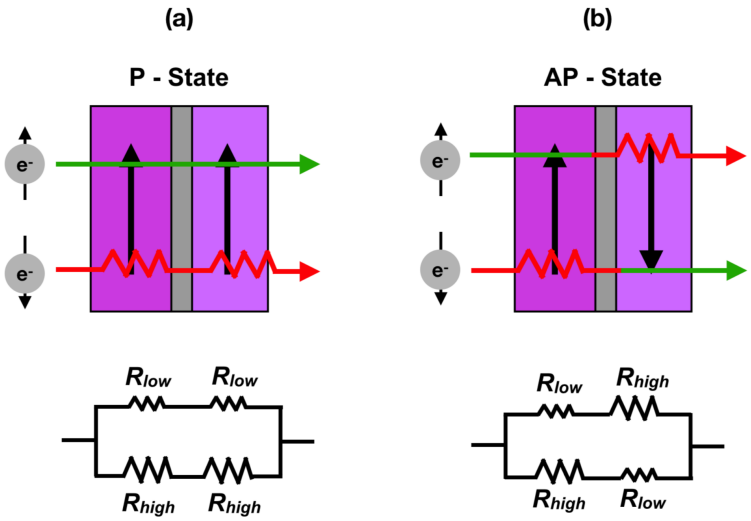

Figure 2.1: Dual career channel illustration for giant magnetoresistance. (a) Magnetizations of the two ferromagnets sandwiching the non-magnetic metallic spacer are parallel and pointed up. For this configuration, spin up and down electrons will experience a lower resistance (R_{low}) and higher resistance (R_{high}) respectively. Beneath the ferromagnet layout is the equivalent circuit diagram representing conduction channels from each spin up and down electrons. (b) Same as (a) but for AP configuration where the magnetizations of the two ferromagnets are in anti- parallel orientations.

down electrons will experience higher resistance (R_{high}) due to spin dependent scattering at the interfaces. As shown in the four resistor circuit diagram, these two parallel electron channels can be modeled resulting an equivalent resistance of

$$R_P = \frac{2R_{low}R_{high}}{R_{low} + R_{high}} \tag{2.1}$$

where R_P is the total resistance for this parallel configuration or i.e. P-state. For the anti- parallel configuration or i.e. AP-state, as shown in Fig 2.1.b, each spin up and spin down channel will experience both high resistance and low resistance depending on the immediate surrounding (local) magnetization. The equivalent circuit diagram is shown below the configuration which produces a total resistance (R_{AP}) of

$$R_{AP} = \frac{R_{low} + R_{high}}{2} \tag{2.2}$$

which is greater than R_P. The efficiency of a GMR device is conventionally quantified as the percentage amount (GMR %) of resistance change it can produce compared to its low resistance configuration as shown below.

$$GMR\ \% = \frac{R_{AP} - R_P}{R_P} \times 100\% \tag{2.3}$$

2.1.2 Tunnel Magnetoresistance

GMR discussed in the previous section is for devices where two ferromagnets are separated by a nonmagnetic metallic spacer and are referred to as spin valves (SV). In contrast, magnetic tunnel junctions (MTJ) are where the two ferromagnets are separated by a thin insulating barrier. In an MTJ, the current flow is due to a quantum mechanical tunneling process of electrons through the insulating barrier from one ferromagnet to the other. Therefore the corresponding magnetoresistance is referred to as tunnel magnetoresistance (TMR). TMR was first discovered by Michel Julliere in 1975 [38] and explained with a spin dependent tunneling model as follows.

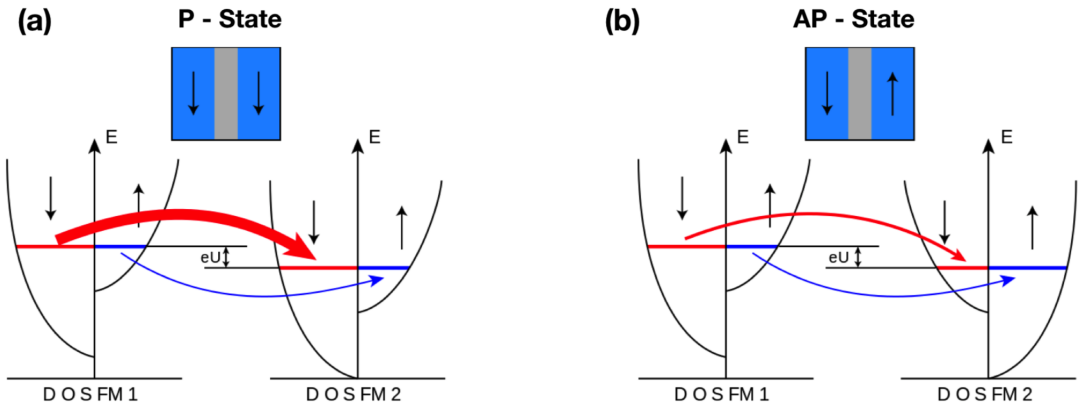

Figure 2.2: Spin polarized tunneling (SPT) between the two ferromagnets via the insulating barrier in a magnetic tunnel junction (after D. Petukhov et al. 2016). (a) Parallel (P) state where both magnetizations are pointing downwards (without loss of generality). Thick red arrow represents the significant tunneling between the spin down electron states where the thin blue arrow represents that for between spin up electron states. The former dominates over the latter as the rate is proportional to the product of the corresponding density of states (DOS) in the two ferromagnets. Total current is proportional to the summation of these two tunneling rates. (b) Similar to (a) but for anti-parallel (AP) state. Both tunneling rates have lower magnitude as the product of DOS being smaller compared to the case regarding the thick red arrow for P-state. As a result the total tunneling rate (current) for AP-state is lower than that for P-state resulting in a higher resistance.

Spin polarized tunneling (SPT) arrises due to different tunneling rates of spin up and spin down electrons through the barrier. This model is based on two assumptions first, spin up (down) electrons from the first ferromagnet can only tunnel into spin up (down) states in the second ferromagnet implying that the total tunneling current consists of two independent spin channels. Second, the tunneling rate for each channel is proportional to the product of corresponding density of states (DOS) in the two ferromagnets. These two assumptions are summarized in Fig. 2.2. For P-state, as shown in Fig. 2.2.a, for both ferromagnets spin down state is the majority state hence the corresponding product of DOS (hence tunneling rate) is larger compared to that for spin up state which is the minority state in both ferromagnets. In the meantime, as seen in Fig. 2.2.b., for AP-state, for both spin channels, tunneling is between from a majority state to a minority state or vice-versa. The net tunneling rate is the summation of those for each spin channel and since the spin down channel in P-state (Fig. 2.2.a) significantly dominates over the rest, the final tunneling rate for P is larger than that for AP which qualitatively explains $R_{AP} > R_P$. After establishing this qualitative picture, a quantitative analysis can be carried out as follows. The net spin polarization (P) of the resulting tunneling current can be written as

$$P = \frac{I^{\uparrow} - I^{\downarrow}}{I^{\uparrow} + I^{\downarrow}} \tag{2.4}$$

where $I^{\uparrow}$ and $I^{\downarrow}$ are contributions to the current from spin up and spin down electrons respectively. Using the assumption that the tunneling rate is proportional to the product of corresponding DOS, the current densities (J_P and J_{AP}) resulting from P and AP states respectively can be written as,

$$J_P \; \alpha \; D_1^{\uparrow} D_2^{\uparrow} - D_1^{\downarrow} D_2^{\downarrow} \qquad J_{AP} \; \alpha \; D_1^{\uparrow} D_2^{\downarrow} + D_1^{\downarrow} D_2^{\uparrow} \tag{2.5}$$

where $D_1^{\uparrow}$ and $D_1^{\downarrow}$ are the DOS for spin up and spin down at the Fermi level of the first ferromagnet respectively. Similarly $D_2^{\uparrow}$ and $D_2^{\downarrow}$ are those defined for the second ferromagnet. Following these relations, spin polarization P_i can be written as,

$$P_i = \frac{D_i^{\uparrow} - D_i^{\downarrow}}{D_i^{\uparrow} + D_i^{\downarrow}} \tag{2.6}$$

Then using the definition for TMR,

$$TMR \;=\; \frac{R_{AP} - R_P}{R_P} \;=\; \frac{J_P - J_{AP}}{J_{AP}} \tag{2.7}$$

Julliere's formula can be obtained.

$$TMR \;=\; \frac{2P_1P_2}{1 - P_1P_2} \tag{2.8}$$

2.2 Effective Magnetic Field

The magnetic field that governs the magnetization dynamics is the local effective field that consists of many components namely, external field, demagnetization (magnetostatic) field, anisotropy field, exchange field and dipole field. Each of these fields contribute to the total energy of the ferromagnet as follows,

$$E_{tot} \;=\; E_Z + E_{dem} + E_{an} + E_{ex} + E_{dip} \tag{2.9}$$

where, E_{tot}, E_Z, E_{dem}, E_{an}, E_{ex} and E_{dip} are total magnetic energy, Zeeman (from external field) energy, demagnetization energy, anisotropy energy, exchange energy and dipole energy respectively. The corresponding field for each energies can be derived as the negative partial derivative of the energy component of interest with the magnetization.

$$\overrightarrow{B}_i = -\mu_0 \frac{\partial E_i}{\partial \overrightarrow{M}} \tag{2.10}$$

Each of these Energies (magnetic fields) has their own origin and can be summarized as follows.

2.2.1 Zeeman Energy

Zeeman Energy is generated due to the coupling of the magnetization with any externally applied field. The Zeeman energy is minimized when the magnetization is aligned with the external field. To be specific, the expression is given as follows,

$$E_z = -M_S V \overrightarrow{B}_{app} \cdot \hat{m} \tag{2.11}$$

where, E_Z, M_S, V, B_{app} and $\hat{m}$ are Zeeman energy, saturation magnetization of the ferromagnet, volume of the ferromagnet, applied external field and the unit magnetization vector of the ferromagnet. This equation is given under the single domain picture and for a spatially non-uniform magnetization this can be applied to an infinitesimal volume element upon which a volume integration is performed. Dipole energy term, E_{dip} arises due to any magnetic stray field from neighboring ferromagnets. The dipole/stray field can thus be added to the external applied field in which case the dipole energy term will be absorbed in to Zeeman energy.

2.2.2 Demagnetization Energy

Demagnetization energy is generated by the demagnetization field which has a magnetostatic origin related to the physical shape of the magnet. Magnetic flux density or simply speaking magnetic field, B can be written as $B = \mu_0(M + H_{dem})$ and is subjected to $\nabla \cdot B = 0$ as required by Maxwell's laws. Here M and H_{dem} are magnetization and demagnetization fields respectively where the role of the demagnetization field is to counteract the magnetization. The demagnetization energy corresponding to this interplay between magnetization and demagnetization field can be written as,

$$E_{dem} = -\frac{1}{2}\mu_0 M_s V \overrightarrow{H}_{dem} \cdot \hat{m} \tag{2.12}$$

While an exact calculation of the demagnetization field for an arbitrary shape is challenging, most of the devices studied can be categorized under the class of ellipsoids. Calculation

of the demagnetization energy for an ellipsoid takes the following form,

$$\overrightarrow{H}_{dem} = -M_s N \cdot \hat{m} \tag{2.13}$$

Here N is the demagnetization tensor containing the geometrical properties of the ellipsoid. The tensor N is diagonal in the basis of the Cartesian axes of the ellipsoid with unit trace leaving H_{dem} in the form of,

$$\overrightarrow{H}_{dem} = -M_s \left(N_{xx} m_x \hat{x} \; + \; N_{yy} m_y \hat{y} \; + \; N_{zz} m_z \hat{z} \right) \tag{2.14}$$

with $N_{xx} + N_{yy} + N_{zz} = 1$ (unit trace). Geometries of interest for real world devices are mainly thin films, circular disks or are elliptical disks where each case can be considered as a certain limit of an ellipsoid.

2.2.3 Anisotropy Energy

Magnetic anisotropy is an energy component arising from shape anisotropy, magneto- crystalline anisotropy, interfacial perpendicular anisotropy and magneto-elastic anisotropy. Anisotropy energy is the excess energy cost to orient the magnetization of the ferromagnet in a direction away from its easy axis where easy-axis is the axis the magnet naturally favors to have magnetized. All the work studied in this thesis have dealt with devices possessing uniaxial anisotropy, i.e., containing only one easy axis. For uniaxial anisotropy the energy term E_{an} can be given by,

$$E_{an} = K_{an} V \left[1 - (\hat{u}_k \cdot \hat{m})^2 \right] \tag{2.15}$$

where K, V, $\hat{u}_k$ and $\hat{m}$ are uniaxial anisotropy volume density, volume of the ferromagnet, unit vector along its easy axis and unit magnetization of the ferromagnet respectively. As can be seen from the equation, anisotropy energy is minimum when the magnetization is along the easy axis (both directions). The corresponding anisotropy field is,

$$B_{an} = \frac{2K_{an}}{M_s} \tag{2.16}$$

The devices studied in this thesis possess perpendicular magnetic anisotropy (PMA) where the easy axis is perpendicular the magnetic layer (disk). Anisotropy energy arising from PMA consists of a bulk effect and surface effect which can be expressed as

$$E_{\perp} = \left(K_V^{\perp} V + K_s^{\perp} A\right)\left[1 - (\widehat{u}_{\perp} \cdot \widehat{m})^2\right] \tag{2.17}$$

where $K_V^{\perp}$, $K_s^{\perp}$, V, A, $\widehat{u}_{\perp}$ and $\widehat{m}$ are bulk contribution, surface contribution, volume of the ferromagnet, surface area of the responsible surface, unit vector along the perpendicular easy axis, and unit magnetization respectively. In a device, PMA can be realized either by well designed material heterostructure (ex. Co/Pt) or engineering material interfaces such as CoFeB/MgO. In the latter case PMA relies on the surface contribution hence for that to dominate over bulk effects (which otherwise promotes an in-plane easy axis), a smaller layer thickness is required.

2.2.4 Exchange Energy

Exchange energy dominates over other energies at short ranges hence tends to align neighboring spins. The origin of this energy is Pauli exclusion principle and in a microscopic picture the energy associated, E_{ex} can be written as,

$$E_{ex} = J_{ex}\left(\overrightarrow{S}_1 \cdot \overrightarrow{S}_2\right) \tag{2.18}$$

where J_{ex}, S_1 and S_2 are exchange constant, and the two spins of the neighboring atoms respectively. To build the macroscopic picture, the given equation can be summed up for each set of 6 neighbor pairs (as the effect is short ranged) and can be given as,

$$E_{ex} = A\left|\nabla \overrightarrow{M}\right|^2 \tag{2.19}$$

where A and M are the exchange stiffness and the magnetization vector respectively.

2.3 Magnetization Dynamics in a Ferromagnet

In equilibrium configuration, magnetization aligns with the local effective field to minimize the energy where the local effective field consists of demagnetization field, anisotropy field, dipolar stray field and external field as described in the preceding section. If the magnetization is brought away from this equilibrium, it will experience a net torque τ according to $\tau = M \times B$ where M and B are the magnetization vector and the local effective field respectively. In an ideal medium without dissipation, this will make the magnetization to undergo persistent precessions which are well known as Larmor precessions as shown in Fig. 2.3.a. However, in real world materials, this precessional energy is dissipated to other internal degrees of freedom mainly due to spin- orbit interaction. In this case, as shown in Fig. 2.3.b., unless an external course is maintaining magnetization's tilt-away angle, it would gradually lose energy spiraling inwards eventually settling back to its equilibrium position. The equation of motion describing this is the well known Landau-Lifshitz-Gilbert (LLG) equation and is as follows,

$$\frac{d\overrightarrow{M}}{dt} = -\gamma_0^{'}\overrightarrow{M} + \overrightarrow{H}_{eff} - \frac{\lambda}{M_S}\overrightarrow{M} \times \left(\overrightarrow{M} \times \overrightarrow{H}_{eff}\right) \tag{2.20}$$

where M, M_S, H_{eff}, $\gamma_0^{'}$ and λ are magnetization vector, saturation magnetization, local effective field, gyromagnetic ratio and Landau-Lifshitz damping parameter respectively. Here, the first term on the right hand side represents the precessional torque from the external field while the second term represents the damping torque as seen in Fig. 2.3.b. However the most common format used in the community is the following which is mathematically identical to the original version with the shown relations, where, α is the Gilbert damping parameter.

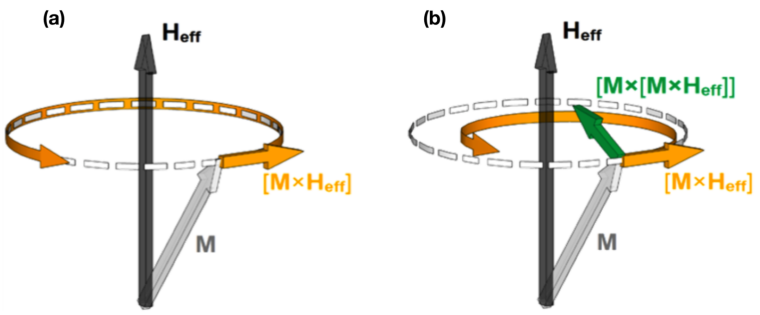

Figure 2.3: Lamer precessions of a magnetic moment. (after A. Makarov et al. 2014) (a) Lamar precession in the absence of any damping. The tip of the magnetization traverses alone a circular path representing a constant energy trajectory. (b) Lamer precession with damping in a dissipative medium. Damping torque tends to bring the magnetization towards its equilibrium position. Unless it is counteracted with an external torque, the precessing magnetic moment will lose its energy to internal degrees of freedom spiraling inwards to settle aligned with local effective field.

$$\frac{d\vec{M}}{dt} = -\gamma_0 \vec{M} \times \vec{H}_{eff} + \frac{\alpha}{M_s}\left(\vec{M} \times \frac{d\vec{M}}{dt}\right) \qquad \gamma_0' = \frac{\gamma}{1+\alpha^2} \qquad \lambda = \frac{\gamma_0 \alpha}{1+\alpha^2} \tag{2.21}$$

With the theoretical formulation of spin transfer torque (STT) additional terms can be incorporated in to the above equation of motion for a more complete picture. Spin transfer torque is generated when a spin polarized current is modified by a magnetic layer [25, 26] as illustrated in Fig. 2.4.a. This occurs whenever the incident spin polarization is tilted away from the magnetization of the subject (i.e., neither parallel nor anti- parallel). The magnetic layer acts like a spin polarizer that modifies the polarization of the incident electrons to be aligned with its magnetization exerting a torque. Following Newton's third law there will be an equal and opposite reaction on the magnetic layer which can be understood as the spin transfer torque. Mathematical calculations [25, 26] from its first predictions shows it takes the form with given term definitions,

$$\frac{d\overrightarrow{M}_{st}}{dt} = \eta(\theta)\frac{\mu_B I}{eV}\widehat{M}\times\left(\widehat{M}\times\widehat{M}_{fixed}\right), \quad \eta(\theta) = \frac{q}{(A+B\cos\theta)}, \quad \cos(\theta) = \widehat{M}\cdot\widehat{M}_{fixed} \tag{2.22}$$

μ_B - Bohr Magneton

I - Current

e - magnitude of elementary charge

V - volume of the ferromagnet (free layer)

$\widehat{M}$ - unit magnetization vector of the free layer

$\widehat{M}_{fixed}$ - unit vector in the direction of the incident spin polarization

θ - angle between incident spin polarization and free layer magnetization

q, A *and* B - constants containing information about device structure

This spin transfer torque in the context of other torques is illustrated in Fig. 2.4.b. The direction of the STT does depend on the sign (direction) of the current and can either be opposite in direction (anti-parallel) to the damping torque or aligned (parallel) with the damping torque. In the former case, STT counteracts the damping and with sufficient magnitude would cancel it out maintaining a finite tilt angle leading to persistent precessions. On the other hand when STT is parallel to the damping torque it simply adds on to it increasing the effective damping.

Apart from this interesting STT term [25, 26], there is another term (comparatively less in magnitude) originating from the spin transfer. It is referred to as field like torque (FLT) due to its resemblance of the precessional torque term from the external field. The expression for FLT is given as follows,

$$\frac{d\overrightarrow{M}_{\perp}}{dt} = \eta_{\perp}(\theta)\frac{\mu_B I}{eV}\left(\widehat{M}\times\widehat{M}_{fixed}\right) \tag{2.23}$$

Here the symbols carry corresponding definitions to those in the expression for STT. FLT is not significant in GMR devices (spin valves) however can reach up to magnitudes about

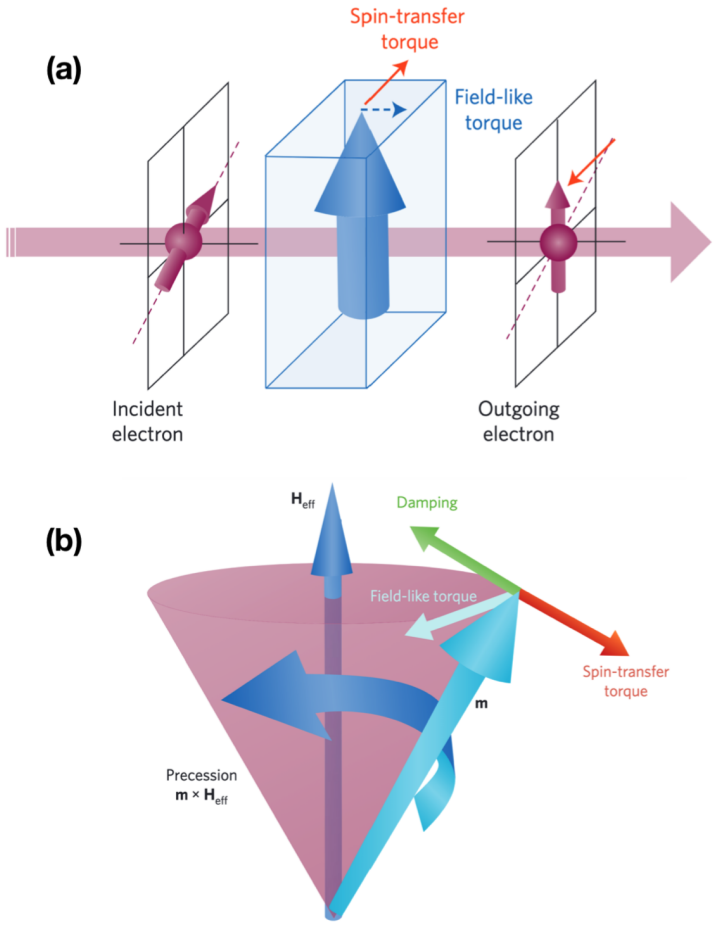

Figure 2.4: Effect of spin transfer torque (after A. Brataas et al. 2012) (a) An example of spin polarized current of electrons entering a magnetized ferromagnet. In general the spin polarization of the electron current is not aligned with the ferromagnet's magnetization direction causing a torque on the latter. For an ideal ferromagnet, the leaving electron current will be spin polarized in the same direction as the former while exerting two kinds of torques, spin transfer torque (STT) and field like torque (FLT) as shown. (b) Complete picture of the torques acting on the magnetization precession. Direction of the STT and FLT depends on the sign of the current. In the diagram, the sign of the current is such that STT opposes the damping torque maintaining a finite tilt-away angle facilitating persistent precessions. For the other current direction, STT will add on to the damping torque and persistent precessions are not possible.

10% of the STT for TMR devices (MTJs). Fig. 2.4.b. summarizes all the torques acting on the magnetization of a ferromagnet (free layer in a device) at a point away form equilibrium. With all these terms (Slonczewski STT and FLT terms) included, Landau-Lifshitz-Gilbert-Slonczewski (LLGS) equation can finally be written as follows.

$$\frac{d\overrightarrow{M}}{dt} = -\gamma_0 \overrightarrow{M} \times \overrightarrow{H}_{eff} + \frac{\alpha}{M_s}\left(\overrightarrow{M} \times \frac{d\overrightarrow{M}}{dt}\right) - \eta(\theta)\frac{\mu_B I}{eV}\widehat{M} \times \left(\widehat{M} + \widehat{M}_{fixed}\right) - \eta_{\perp}(\theta)\frac{\mu_B I}{eV}\left(\widehat{M} \times \widehat{M}_{fixed}\right) \tag{2.24}$$

2.4 Perpendicular Magnetic Tunnel Junction

Initial spin valves and magnetic tunnel junctions possessed shape induced in-plane anisotropy therefore had in-plane magnetized free and fixed layers. LLGS equation predicts that critical current for current induced switching is less for perpendicular devices compared to in-plane devices [25, 26]. This motivation led to the invention of perpendicular spin valves [39, 66] and MTJs [67, 68, 69, 70, 71, 72, 73, 74] where interfacial effects between different materials are exploited to induce a perpendicular easy-axis. It had also been shown that STNOs based on orthogonal structures (one layer in-plane and the other perpendicular) could produce stable microwave precessions [17] even in the absence of any external bias magnetic fields that had been required by complete in-plane structures. Both projects reported in this thesis involve MTJs with perpendicular anisotropy. Therefore herewith, I decided to include a summarized description of MTJs with perpendicular anisotropy to set the theoretically background for later reference.

First perpendicular CoFeB/MgO based MTJ that simultaneously offered high thermal stability, low critical current for current induced switching and high TMR was first reported in 2010 by S. Ikeda et al. [40]. This work received great attention as it used same materials, CoFeB and MgO, which were used to realize then state-of-the-art in-plane MTJs. Even to date, this material combination has proven its great potential in perpendicular MTJs for overall performance. Figure 2.5 presents the key finding of the work by S. Ikeda et al. 2010.

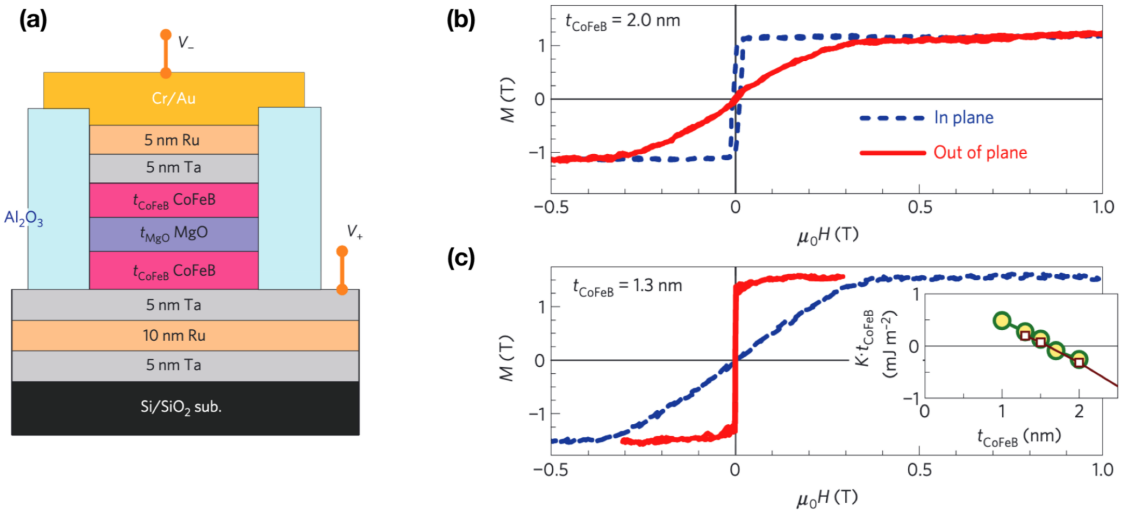

Figure 2.5: Perpendicular MTJ realized with IPMA by S. Ikeda et al. 2010 (a) CoFeB/MgO/CoFeB based MTJ structure where the thickness of the CoFeB layers are varied to induce the perpendicular easy-axis. (b) In-plane and out-of-plane magnetization curves for a CoFeB layer with thickness 2.0 nm. Abrupt transition in the in-plane curve holds evidence for an in-plane easy axis. (c) In-plane and out-of-plane magnetization curves for a CoFeB layer with thickness 1.3 nm. Abrupt transition in the out-of-plane curve holds evidence for a perpendicular easy axis. Inset: t_{CoFeB} dependence of the product of K and t_{CoFeB}, where the intercept to the vertical axis and the slope of the linear extrapolation of the data correspond to K_i and $K_b - \frac{M_s^2}{2\mu_0}$. Circles and squares are obtained from magnetization and FMR measurements, respectively.

An iron rich ferrimagnetic layers ($Co_{20}Fe_{60}B_{20}$) are used here which is the key ingredient to enhance the interfacial perpendicular anisotropy (IPMA) that originates from hybridization of Fe_{3d} (from CoFeB) and O_{2p} (from MgO) orbitals. Fig. 2.5.a, presents the device that was studied where the evolution of the easy-axis was monitored as the thickness of the ferromagnet is varied. Fig. 2.5.b and c illustrate the evolution of a single layer magnetization upon an external field applied in-plane and out-of-plane for layer thicknesses 2.0 nm and 1.3 nm respectively. For layer thickness of 2.0 nm the easy-axis has been in-plane as evident by the sharp transition of the magnetization with in-plane field sweep while that has been out-of-plane for layer thickness 1.3 nm which demonstrates the realization of a perpendicular easy axis by reducing the layer thickness. To isolate the interfacial contribution of the anisotropy, total anisotropy constant has been considered as follows,

$$K = K_b - \frac{M_s^2}{2\mu_0} + \frac{K_i}{t_{CoFeB}} \tag{2.25}$$

Here K, K_b, K_i, M_S, μ_0 and t_{CoFeB} are perpendicular anisotropy energy density, bulk crystalline anisotropy energy density, interfacial anisotropy energy density, saturation magnetization, permeability of free space and free layer (CoFeB) thickness respectively. Inset of Fig. 2.5.b presents t_{CoFeB} dependence of the product of K and t_{CoFeB} and is fitted according to the above equation. From the intercept, K_i is determined to be 1.3 mJm^{-2}. By comparing bulk contribution to the demagnetization energy density, K_b is estimated to be negligible concluding that the perpendicular anisotropy of the system is entirely due to CoFeB/MgO interface.

2.5 Magnetic Skyrmions

As described in chapter 1, magnetic skyrmions are topologically stable localized spin spiral structures of which normalized magnetization can be mapped on to a unit sphere covering an entire sold angle of 4π where this winding can be characterized by a topological number S as given by

$$S = \frac{1}{4\pi} \int_A \hat{m}. \left(\frac{\partial \hat{m}}{\partial x} \times \frac{\partial \hat{m}}{\partial y} \right) dxdy \tag{2.26}$$

where A is the surface area, $\hat{m}$ is the normalized magnetization vector and x and y are spacial coordinates [55]. A topological number $S = +1$ represents a single skyrmion while a topological number $S = -1$ represents an anti-skyrmion. A topological trivial configurations such as a ferromagnetic state has a topological number of $S = 0$. Skyrmions can be stabilized in magnetic systems lacking inversion symmetry that lead to an asymmetric exchange namely, Dzyaloshinskii–Moriya interactions (DMI) [52, 53] induced by spin–orbit coupling (SOC). Contribution to the total hamiltonian by this DMI takes the form,

$$H_{DMI} = \left(\overrightarrow{S}_1 \times \overrightarrow{S}_2 \right) \cdot \overrightarrow{d}_{12} \tag{2.27}$$

where, $\overrightarrow{S_1}$ and $\overrightarrow{S_2}$ are neighboring spins and $\overrightarrow{d_{12}}$ is the corresponding Dzyaloshinskii–Moriya vector. The latter can be written in the form

$$\overrightarrow{d_{12}} = d_{12} \cdot (\hat{z} \times \hat{u}_{12}) \tag{2.28}$$

where, $\hat{z}$ and $\hat{u_{12}}$ are unit vectors perpendicular to the interface in the direction of the magnetic layer and pointing from site 1 to site 2 respectively. This is illustrated in Fig. 2.6 which is adopted after A. Fert et al. 2013. By the symmetric exchange energy alone, the neighboring spins will align either in parallel (ferromagnetism) or in anti-parallel (anti-ferromagnetism) to minimize energy. However, in the presence of an anti-symmetric exchange, hamiltonian is modified as above where neighboring spins will be rotated around d_{12} to minimize energy. Chirality of this rotation depends on the sign of d_{12} where $d_{12} > 0$ will induce an anti-clockwise rotation while $d_{12} < 0$ will induce a clockwise rotation. This twisting of the local magnetization ultimately forming a spin spiral can then be thought of as resulting from a competition between the conventional exchange interaction and DMI. For interfacial DMI, DMI vector lies on the plane of interface and the final effect can be summarized in to a micromagnetic energy per unit volume as,

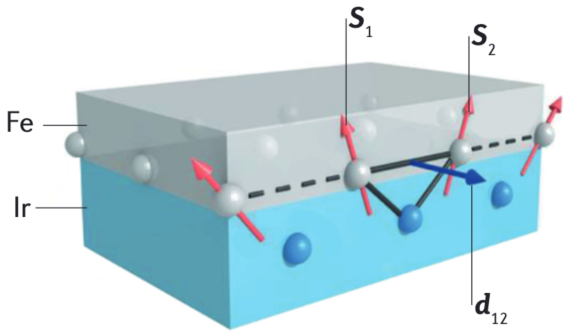

Figure 2.6: Interfacial DMI between a ferromagnet (Fe) and a metal with strong spin orbit coupling (SOC) (Ir). The DMI vector d_{12} related to the triangle composed of two magnetic sites and an atom with a large SOC is perpendicular to the plane of the triangle (after A. Fert et al. 2013).

$$E = D\left(m_z\partial_x m_x - m_x\partial_x m_z + m_z\partial_y m_y - m_y\partial_y m_z\right) \tag{2.29}$$

where D is the DMI constant, which is related to the pair interaction d_{12} in aforementioned hamiltonian.

CHAPTER 3

Experimental Setup

3.1 Device Structure

Magnetic tunnel junctions (MTJ) are most commonly designed with two layers while three layer devices are also sometimes considered. My studies involve both of these two kinds, first with three layers and the second with two layers. The layout of the designs are shown in the Fig 3.1. The UCLA owned device is a stack of several layers making up a top polarizer (top $Co_{20}Fe_{60}B_{20}$), precession layer (middle $Co_{20}Fe_{60}B_{20}$) and bottom polarizer (bottom $Co_{20}Fe_{60}B_{20}$) the latter performing as the reference layer as well. To make the devices, first, films were deposited using a Singulus TIMARIS PVD system and annealed at 300^o C for 2.0 hours in a magnetic field of 1 T applied perpendicular to the film. The films were then patterned into nano pillars with different aspect ratios using electron-beam lithography and ion milling techniques. The Avalanche owned devices consist of two layers (free and fixed) both are designed as heterostructure.

The key technique to characterize an MTJ is to make DC transport measurements with applied magnetic field. This allows one to figure out the magnetization directions of each layer of the device at equilibrium. Once the basic characteristics are known, the experiments are designed to study the high frequency dynamics of these devices. This dynamics can mainly be categorized into, DC induced RF response or RF induced DC/RF response. For these tasks we have two different setups one for the studies at room temperature and the other for the studies at cryogenic temperatures. The tabletop setup for the room temperature experiments will be discussed first as follows.

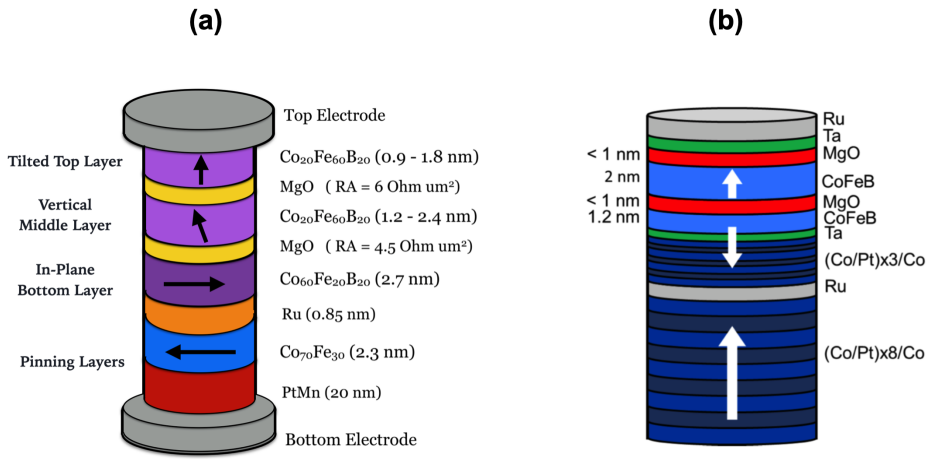

Figure 3.1: MTJ device layout. (a) Layout of the tri-layer UCLA samples. The bottom layer is in-plane, top and middle layers are vertical but the middle layer is tilted out owing to the dipole coupling from the bottom layer. (b) Layout of the two layer Avalanche samples. Both the fixed and the free layers are vertical.

3.2 Room Temperature Setup

For both room temperature and cryogenic setups, the device should be probed in a way which is compatible for both DC and RF measurements. Room temperature setup has the advantage of having sufficient space to use a state-of-art high frequency ground signal ground (GSG) probe which is designed for DC to 40 GHz. A picture of this room temperature probing system is shown in Fig. 3.2. The device is located on the top of GMW 3D projected magnetic which can be moved in x, y and z direction and rotate around the vertical axis to apply a magnetic field in the preferred direction at the location of the device. The calibration curves are provided and we also use 3-axis magnetic field calibration sensor to confirm the calibration. The delicate Ground- Signal-Ground (GSG) probe to make electrical connection with the device is mounted to another stage which can be moved up and down to touch down the device. To perform this task, the device is looked through a microscope and great care is taken not to damage the tip of the probe by having it pressed too hard against the chip.

Making electrical connection with the device to the DC and RF instruments is not trivial.

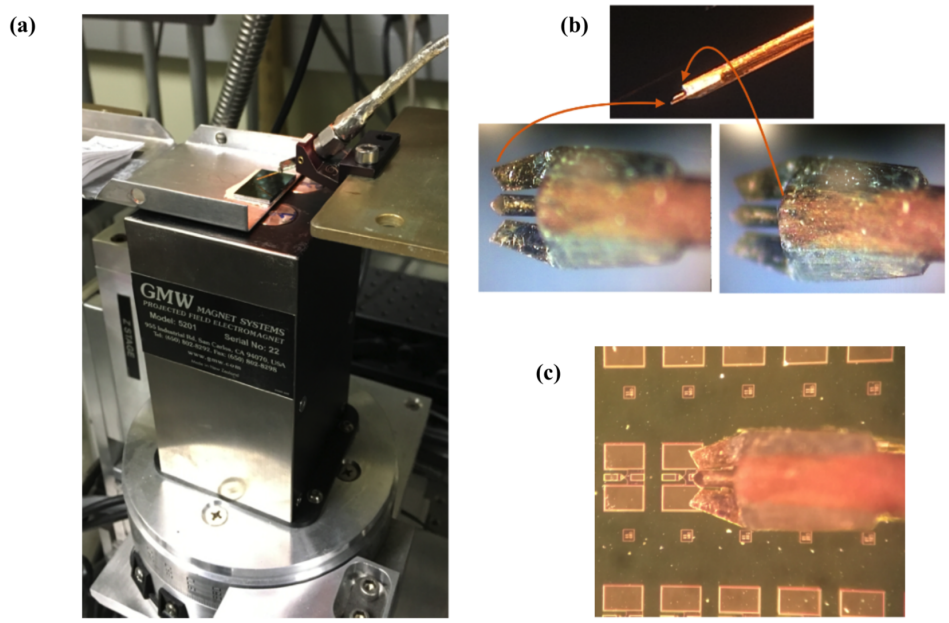

Figure 3.2: Tabletop Experimental setup to apply magnetic field and make electrical connection with the device. (a) GMW 3D projected magnetic which can be moved in x, y and z direction and rotate around the vertical axis to apply a magnetic field in the preferred direction at the location of the device. The calibration curves are provided in the manual and we also use 3-axis magnetic field calibration sensor to confirm the calibration. (b) Ground-Signal-Ground (GSG) probe to make electrical connection with the device. The probe is designed for signals ranging from DC to 40 GHz. (c) Microscopic view of the probe connecting to the device. In the picture all three terminals of the probe are connected to the ground pads of the device. In normal operation probe's terminals are sitting on the two big ground pads and the small pad which is sandwiched by the ground pads.

One needs to consider transition line theory and appropriate actions need be taken when separating and combining the DC and RF channels. There are three main RF devices we use, namely, bias-tee. directional coupler and combiner/splitter. Bias-tee is a three way junction which accepts the DC+RF signal from the device end and then pass it through a high frequency and a low frequency filter to extract the RF response and the DC response respectively. Bias-tee is required for all experiments except magnetoresistance measurements. However practically, for convenience, we leave the bias-tee in place for all the experiments. It is also safer to do so as every time you connect and disconnect the device, you risk it being burnt out by static electricity. Directional coupler is a three terminal device that has a bidirectional channel between two terminals and uni-directional channeled coupled to one of the aforementioned terminals. This is specially used in injection locking experiments where the RF pump from the signal generator is only made to transmit towards the device and the emission of the device is directed towards the spectrum analyzer. Combiner/ Splitter (both referred to the same device) is a three terminal bidirectional device where it is used either to combine two RF signals together or to split an RF signal (for example the emission from the device) to two channels to be fed into two different instruments.

Fig. 3.3.a shows the layout of the experimental setup for FMR measurements. As described earlier, the DC channel separated via the bias-tee is connected to a current source , a voltmeter and a lockin amplifier. The current source provides the bias current and the voltmeter measures the voltage across the device. The lockin measures the rectified DC voltage across the device in response to the RF stimulation from the signal generator which accepts a modulation from the lockin amplifier. The RF from the signal generator is modulated with a frequency of choice (ex. 200 kHz) and as a result, the rectified voltage across the device also modulates at the same frequency. The lockin amplifier can then extract that signal from the noisy background. There is an optional attenuator at the output of the signal generator to attain lower power levels below the minimum power the instrument can offer (-20 dBm).

Fig. 3.3.b shows the experiment setup for the emission and injection lockin experiments. Same as previously explained, the DC channel of the bias-tee is connected to the current

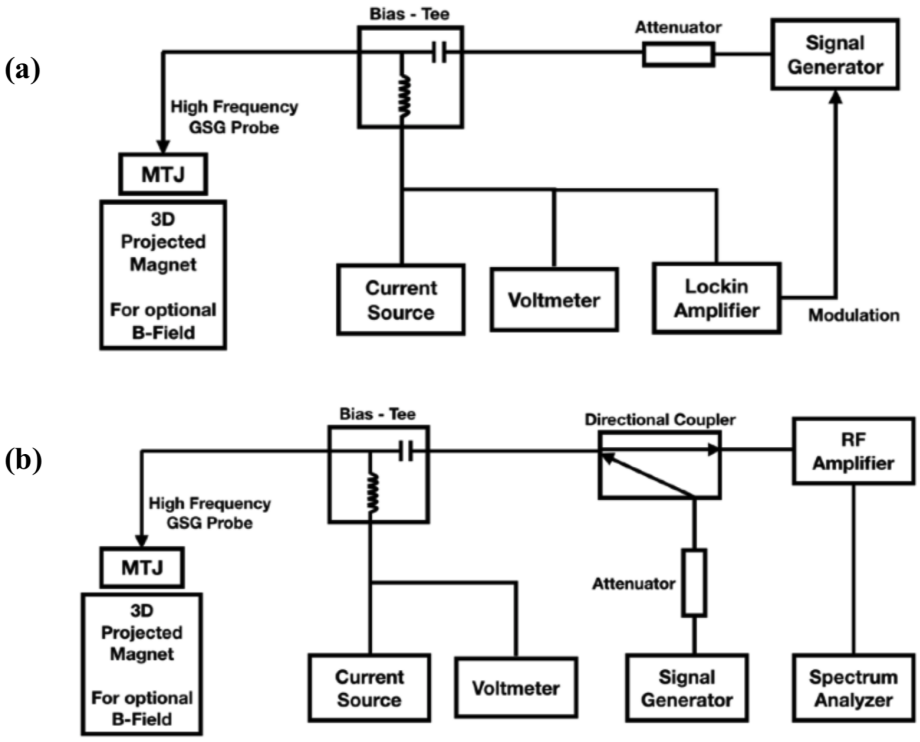

Figure 3.3: Tabletop experiment layout for microwave experiments. Device is mounted on the top of the 3D projected magnet which applies B_x, B_y, B_z as requires. The device is probed with a high frequency (DC to 40 GHz) Ground-Signal-Ground probe which is then connected to a Bias- Tee which separates DC to 300 kHz signal/bias and high frequency response/stimulant. DC channel from the Bias-Tee is connected to a current source for DC bias and a voltmeter for simultaneous device voltage measurements (a) Specific setup for FMR experiments. The AC channel from the Bias-Tee is connected to the signal generator which also accepts the modulation output from the Lockin for AM modulation. The input of the lockin is connected to the DC channel of the bias-tee. (b) Specific setup for emission and injection locking experiments. A Direction-Coupler is used to connect the high frequency line from the Bias-Tee to the spectrum analyzer via an RF amplifier and to the signal generator for optional RF stimulant (for injection locking experiments). An optional attenuator is placed at the output of the signal generator to attain low power levels than the signal generator can produce.

source and the voltmeter. The AC channel of the bias-tee is connected to the signal generator and the spectrum analyzer. The former would pump RF for injection locking and the latter would record the emission under the stimulation. The directional coupler may be removed for the emission only experiments.

3.3 Cryogenic Temperature Setup

We decided to conduct some experiments at liquid nitrogen temperature for a couple of reasons. For UCLA owned samples we were interested in studying the thermal induced emission and for Avalanche owned samples, it was required to reduce the temperature to have a perpendicular free layer for the desired experiments. Our lab is equipped with three cryogenic fridges but the scope of those are far beyond what I need to have for my experiments. Therefore I decided to build a crystat of my own to accommodate the requirements of my experiments. Liquid Nitrogen temperature (77 K) is a suitable base temperature for my purposes. And it was preferred to have the temperature control from 77 K to room temperature.

To achieve this I used one of the old probe setups our lab had and converted that in to what I needed with custom made parts. It mainly consists of two concentric cylinders hosting two vacuums that are connected to the house pump or to a vacuum pumper if better vacuum is required. The printed circuit board (PCB) containing the device is placed in the inner vacuum. By controlling the amount of exchange gas in these two vacuums the thermal contact of the device with the liquid nitrogen bath can be controlled. To mount a device on this PCB the main chip had to be cut in smaller pieces. It was done by cleaving from diamond tip scribe after depositing a photoresist protective layer. After cutting, the protective layer is removed from Acetone, IPA, and distilled water. Fig. 3.4.a shows some cut chips ready to be mounted on the PCB. A heater resistor and a temperature sensor are also placed on the PCB and are connected to LakeShore temperature controller which is capable of maintaining a set temperature via a feedback loop. Fig. 3.4.b shows the PCB accommodating the device, heater resistor and the temperature sensor. Electrical connection

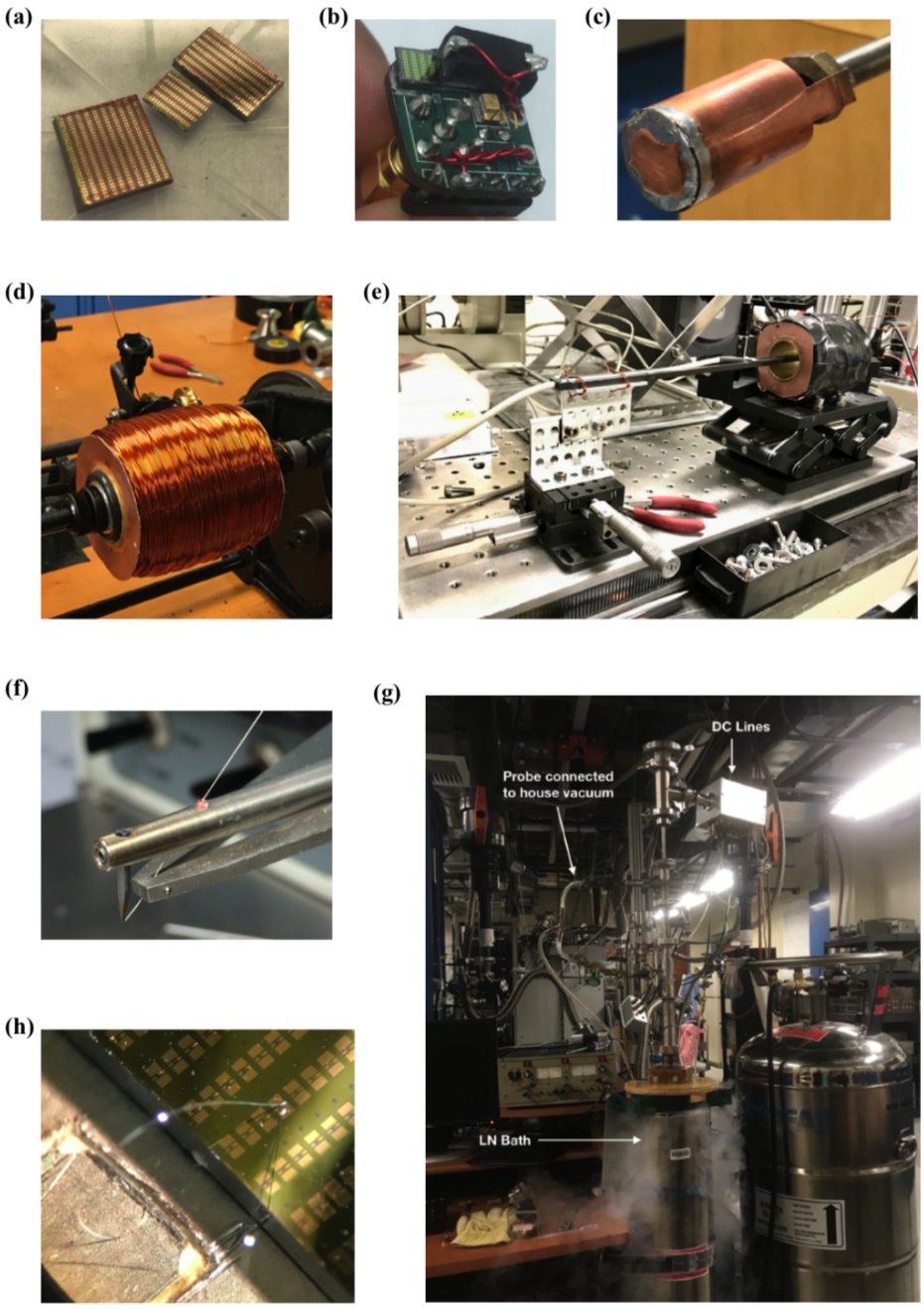

Figure 3.4: Construction of the Setup for the cryogenic measurements. (a) Main chip containing about 600 devices cut in small pieces to fit in the cryostat probe. (b) Cut chip glued to the PCB containing the heater resister (black) and the temperature sensor (gold). (c) Housing for the PCB made to protect the PCB with the device to go inside the vacuum cylinder. (d) Homemade electromagnet. (e) Calibration of the electromagnet. (f) Wirebonding needle with the wirebonding Al wire. (g) Picture of the actual setup (h) Wirebonded device.

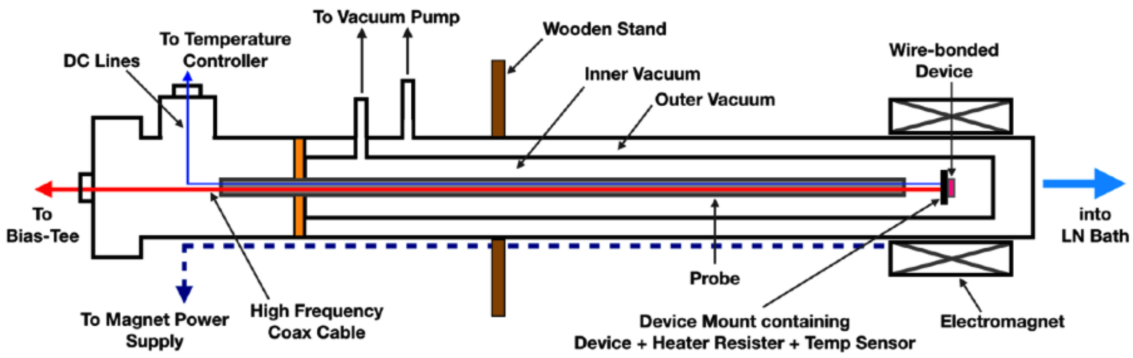

Figure 3.5: Design of the cryostat chamber. The chamber mainly consists of two co-centric cylinders hosting inner and outer vacuum. The probe with the device sits at the center of the inner vacuum. DC and high frequency lines are wired through the probe connecting to the vacuum-tight ports accessible from outside. The magnet is placed co-centering the two cylinders outside of the outer cylinder and the device is placed at the center location of the magnet. Both the vacuums are connected to the house vacuum and are being constantly pumped out.

to the device were made through wire bonding.

Fig. 3.4.f and h show the wirebonding needle. and the wire bonded device respectively. This PCB is connected to the Coax cable and the DC lines and enclosed in custom made copper housing for protection. Fig. 3.4.d and e show the construction of the custom designed electromagnet and its calibration setup respectively. The electromagnet is designed to achieve a maximum of 60mT steady field and a maximum of 80 mT of short time field in liquid nitrogen. At the room temperature the coil has a resistance of 16 Ω which is reduced by a factor of 10 at 77 K. The calibration for the field is 14.2 mT/A. Fig. 3.4.g shows the picture of the setup once put together.

Fig. 3.5 shows a detailed design of the cryostat chamber. The main probe carries the DC lines and the Coax cable for the temperature sensor, resistor heater and the device respectively. The probe is then placed inside the inner vacuum. The electromagnet is placed outside of the chamber and the power line is routed from outside. Fig. 3.6 shows the

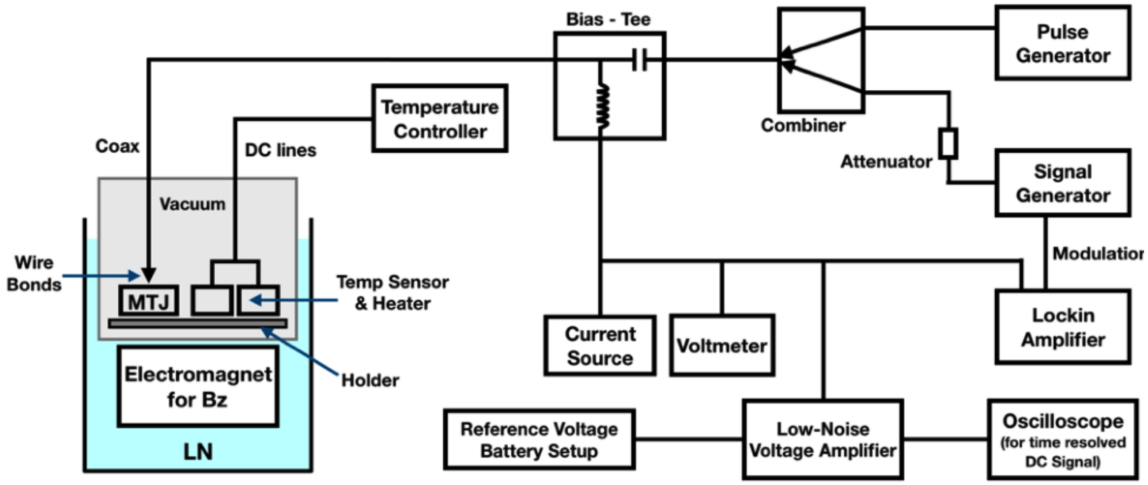

Figure 3.6: Measurement setup for the low temperature measurements. The temperature sensor and the heater resistor are connected to the Lakeshore temperature controller that maintains a set temperature with the aid of a feedback loop. The DC/RF connection from the device is connected to a bias-tee to separate the DC and the RF channel. The RF channel of the bias-tee is connected to a combiner which combines the input from the signal generator and the pulse generator. The DC channel of the bias-tee is connected to a current source, voltmeter, lockin amplifier and a low-noise voltage amplifier. The lockin amplifier is used in FMR experiments while the low-noise voltage amplifier is used for random telegraph signal experiments. This voltage amplifier accepts a reference voltage for signal truncation and outputs the signal to an oscilloscope to record the signal in time domain.

experimental setup for this cryogenic experiments. The temperature sensor and the heater resistor DC lines are connected to the Lakeshore temperature controller that maintains a set temperature with the aid of a feedback loop. The DC/RF connection (via Coax) from the device is connected to a bias-tee to separate the DC and the RF channel. The RF channel from the bias-tee is connected to a combiner which combines the input from the signal generator and the pulse generator. The DC channel of the bias-tee is connected to a current source, voltmeter, lockin amplifier and a low-noise voltage amplifier. The lockin amplifier is used in FMR experiments while the low-noise voltage amplifier is used for random telegraph signal (RTS) experiments. For RTS experiments, monitoring of the DC signal in time domain for small variations is required hence the low-noise voltage amplifier is used. The dynamical signal in the DC background in interest is a small fraction hence to avoid saturation at the amplifier a signal truncation is required. The amplifier itself offers the truncation option as an additional reference voltage at the input. For this reference voltage a battery setup was used as it is the most steady voltage source available. After the truncation is done the amplifier outputs the amplified signal to an oscilloscope to record the signal in time domain. The oscilloscope is operating in a slower sampling rate at about 10 Hz. Apart from that as previously explained, the DC channel from the bias-tee is also connected to a lockin amplifier for FMR measurement along with the modulation technique implemented.

CHAPTER 4

Zero-Field Microwave Emission in a Tri-Layer MTJ

4.1 Magnetoresistance Loops

Magnetic tunnel junctions (MTJ) are most commonly designed with two layers or three layers where one of them acts as a fixed layer and the remaining being free layer(s). Main characterization of an MTJ is to assign the equilibrium magnetization directions at zero external magnetic field. To perform this task, an external magnetic field is swept in a specific direction (x, y or z) at a time while monitoring the MTJ resistance. With the evolution of this resistance with external magnetic field in all three directions, one can uniquely determine the individual layer magnetizations in equilibrium, i.e., at zero external field. This exercise for a two layer MTJ is quite straight forward however, for a three layer MTJ it can be complicated. Reason is, in the latter case there are two free layers (hence more degrees of freedom) compared to the former case where there is only one.

Conceptually, a tri-layer MTJ consist of three layers however, to realize that requires quite more detailed design following material engineering techniques. To discuss the physics of an MTJ as a spin transfer torque and a tunnel magnetoresistance device, only key layers are required. In this chapter, tri-layer UCLA devices are discussed which have top, middle and bottom principle layers. Fig. 4.1 illustrates these principle layers in the context of the actual device layout demonstrating its functional abstraction.

In Fig. 4.1.a is the complete device structure with layers in their nominal thicknesses. Top and bottom sections in grey color are buffer layers as designed by material engineers. Colored layers are the actual functional layers that are usually included in published literature. As shown, direction of positive conventional current is from top to bottom layer, i.e., for positive

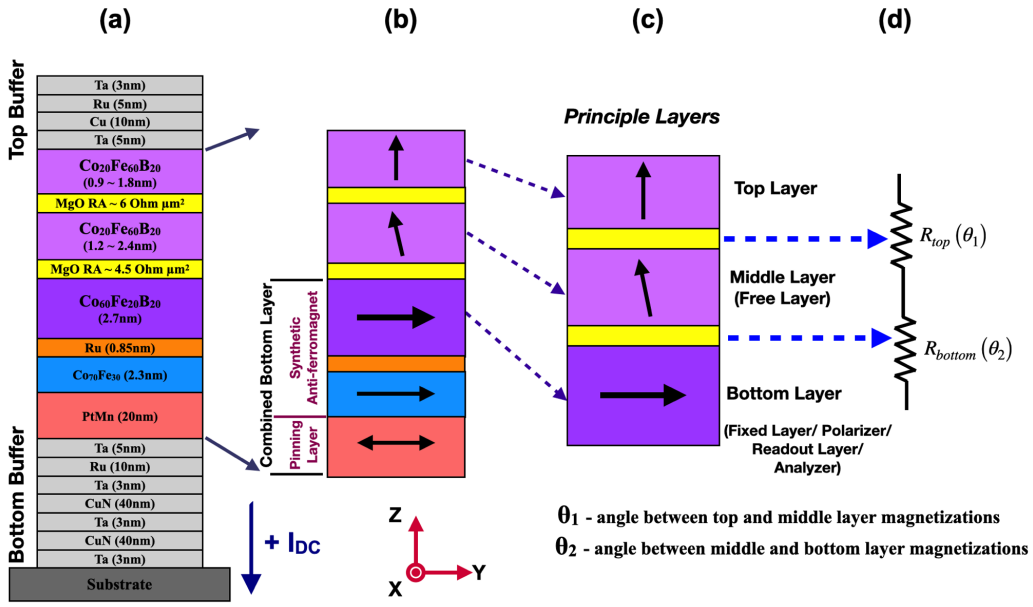

Figure 4.1: Tri-Layer MTJ structure with definitions of coordinate system and positive conventional current. (a) Complete layout of the fabricated device including buffer layers. Within the parentheses are the nominal thicknesses. As denoted, positive conventional current flows from top to bottom buffer layer. (b) Reduced version of the device structure included in published literature. The bottom layer is a heterostructure which consists of four layers. Bellow, the convention of the axis system is shown for later reference. (c) Model containing only the principle layers (active layers) that will be referred to explain the properties and dynamics of the device. Bottom layer is also called fixed layer, (bottom) polarizer, readout layer or analyzer in published literature. Top and middle layers process perpendicular (to plane) easy axis however, middle layer is slightly tilted out owing to the dipole coupling from the bottom layer. (d) Electrical point of view of the device. TMR caused by each MgO layers is modeled as a resister each depending on the mutual angle between the magnetizations of respective layers.

bias, electrons flow from bottom to top layer. Fig. 4.1.b shows this reduced version of the structure. First two layers are physically individual layers while the bottom layer of the MTJ is a composite of several layers together making the functional bottom layer. Top three layers of this composite bottom layer structure construct a synthetic anti-ferromagnet (SAF) via the RKKY coupling through the Ru layer. Bottom layer of this SAF is pinned by an anti-ferromagnet to enhance the stiffness (The latter is hence called "pinning layer"). Top most layer of this combined bottom layer is the principle bottom layer as seen by layers above. Fig. 4.1.c illustrates the three principle layers of the tri-layer structure that will be referred repeatedly later in the text. The bottom layer is also called fixed layer, (bottom) polarizer, readout layer or analyzer in published literature. Both top and middle layers process perpendicular (to plane) easy axis however, the middle layer is considered to be slightly tilted out owing to the dipole coupling from the bottom layer. The two MgO layers sandwiched by the three layers create two tunnel magnetoresistors. This tri-layer MTJ consisting of two MgO tunneling barriers can hence be modeled as two resistors each representing one tunneling barrier. Since the current through the MTJ has to pass through one barrier at a time, these two resistors are connected in series therefore, the final MTJ resistance will be the summation of those two. The resistance of such a junction depends on the mutual angle between the magnetizations of the neighboring layers. In this case, θ_1 is the angle of between the top and the middle layer magnetizations while θ_2 is that between the middle and the bottom layer magnetizations. The convention for coordinate axis system for later referencing is shown below Fig. 4.1.b.

Fig. 4.2 presents some sample magnetoresistance loops obtained from various samples for all three field directions. The volume of the top and middle layers are small enough to be single domain, however, defects can occur which could lead to many irregularities as seen in the preliminary results shown in Fig. 4.2. This is always the case for MTJ experiments and in a tri- layer system such additional footprints of defects along with already existing extra degrees of freedom make it quite challenging to identify and extract the generic behavior. From Fig. 4.2.a, for x-axis MR loops (MR_X loops), the generic behavior can be seen as

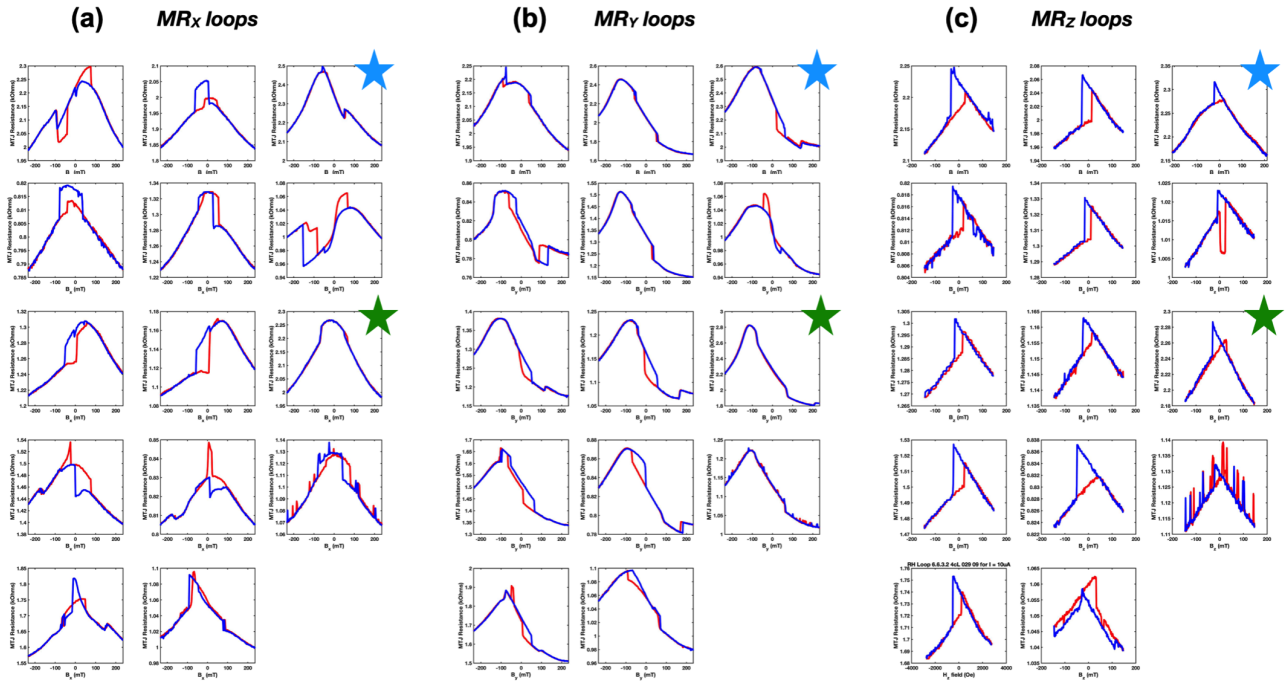

Figure 4.2: Magnetoresistance (MR) loops obtained for various devices. (a) MR loops for the x direction. (b) MR loops for the y direction. (c) MR loops for the z direction. The green and blue stars shows the two devices that the analysis is made on.

reduction in resistance as the field swept for both directions. As seen in Fig. 4.2.b, for y-axis MR loops (MR_Y loops) the resistance fairly decreases along the positive B_y direction while along the negative B_y direction, it initially increases and then decreases. As seen in Fig. 4.2.c, z-axis MR loops (MR_Z loops) are more feature rich. To further study these 3-axis MR loops towards understanding the zero field tri-layer configuration, I have selected two devices with minimal to non anomalies (from defects) which are pointed out by the green and blue starts in Fig. 4.2. The $MR_{X,Y,Z}$ loops for one of those devices are presented again in fig. 4.3 with more attention to detail.

From fig. 4.3, it can be seen that for each axis direction, TMR variation range of MR loops are different. Therefore, for comparison and to put them in the same context it is

useful to have them on the same plot. Fig. 4.3.d shows all $MR_{X,Y,Z}$ loops on the same plot. It should be mentioned that with the available experimental setup, maximum vertical (z-axis) field obtainable is about 64% of the maximum in-plane field. Among the three layers of the device, the bottom layer is designed to be in-plane fixed by having it pinned to a pinning layer. Then the question is, is the bottom layer along the x or y axis in the aforementioned coordinate system. Looking at fig. 4.3.d it can be seen, both minimum and maximum resistance values are present in the MR_Y loop. This can occur only if the bottom (fixed) layer is along the y-direction. This marks the first assignment of the magnetizations of the tri-layer device. And in the remaining story this bottom layer is assumed to remain fixed in the positive y direction apart from a minor tilting at high orthogonal (x or z) fields causing a little to non contribution towards TMR change.

The top and the middle layers of the device are thinner than 1.7nm and have CoFeB/MgO interface. Under these conditions a significant amount of IPMA is present and both top and middle layers can expected to be vertical having a perpendicular easy axis [40]. Given this, the most crucial MR loop to resolve is MR_Z loop. There are two major qualitative features in this MR_Z loop. First, there exist two quasilinear reversible branches (QRB) in between which two hysteresis transitions are occurring. The location of these abrupt transitions can differ from device to device mimicking triangles or other geometries in the MR loop as can be seen in fig. 4.2.c. The branches are called reversible as once in a given brach the device can brought back and forth up to the hysteresis switch.

An important thing to notice is, the range of the TMR variation of the QRBs is only about 3% which is significantly low for an MgO based MTJ. This suggests that, QRBs are a result of a minor (close to zero) mutual angle evolution of the layer magnetizations. For an MTJ such behavior is usually attributed to the slight tilting of the pinned fixed layer, which is the bottom layer in this device. However for this MR_Z loop the QRB with the observed minor TMR change is present near zero field as well which cannot be explained from a tilting of the fixed layer as it is only justifiable within the high field regime. A minor TMR change in an MR_Z loop can also occur in a perpendicular free layer that is canted out of its

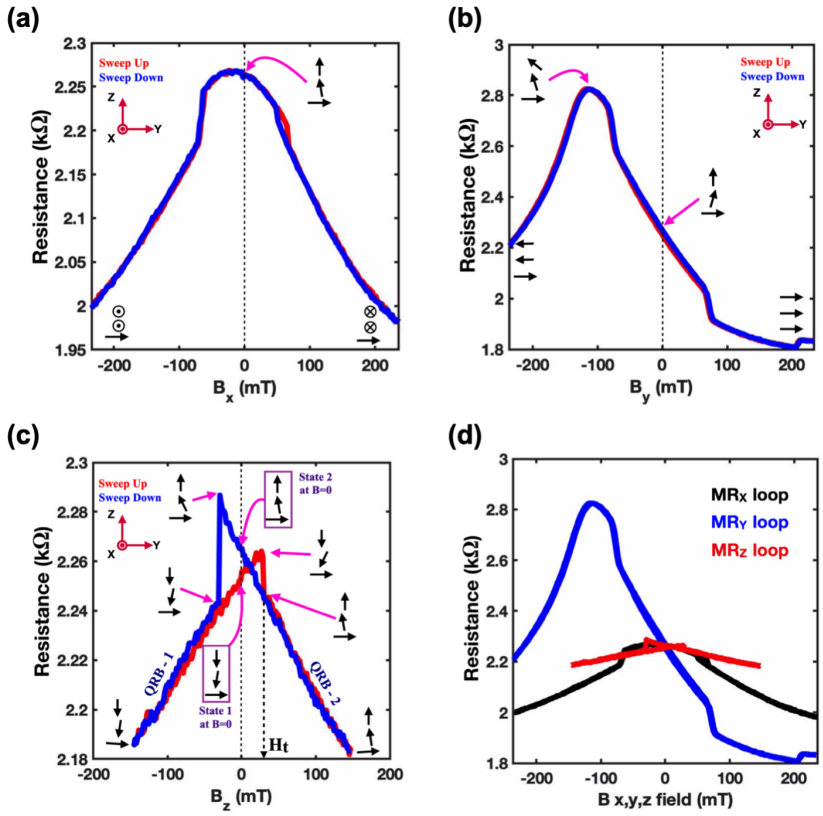

Figure 4.3: Magnetoresistance loops for x, y and z axises. Magnetic field is first brought to the negative maximum and then swept in positive and negative directions recording the device voltage (to calculate resistance). Applied bias current is $10\mu A$. Curve corresponding to field sweeping along positive field is in red while that for field sweeping along negative field is in blue. Insets illustrate the tri-layer magnetization configuration at different key positions on each MR loop. Convention of axis system is also shown. (a) MR_X loop which is near symmetric around the x-axis. (b) MR_Y loop. (c) MR_Z loop. Two quasi-linear reversible branches (QRB) are present in between which two hysteresis transitions occur. The device can be initialized in two different states as shown. To initialize the device in picture 1 (2) a large negative (positive) field should be applied (after which the field brought to zero). QRBs are labeled as shown for later reference. The field at which the right-hand-side hysteresis transition occurs is defined as H_t for later reference. (d) All three axis MR loops plot in same axis system for dynamical TMR comparison. MR_Y possesses both highest and lowest TMR observed. MR_Z has very small TMR variation which will be discussed later.

vertical axis due to any dipole coupling from an adjacent in-plane layer and such a canted angle is usually about 10 degrees [75, 76, 77]. In this device, it is true for the middle layer under the dipole coupling of the bottom layer. However, even though the middle is under in-plane dipole coupling, the layer itself already has high IMPA field (due to double MgO layers) and also under a vertical dipole coupling from the top layer. Hence the canted angle of this middle layer is expected to be even less than 10 degrees causing even smaller linear TMR change in the MR_Z loop (this canted angle in the plots are exaggerated for clarity). Therefore, the final resulting QRB can be considered to have caused by minor tilting of both middle and the bottom layers.

Another important thing to notice is that, the changes in TMR through the hysteresis switching are quite low as well. This is very abnormal for a MgO based MTJ if the mutual angles between layer magnetization reorient significantly. Therefore, the only option to explain such a behavior is having both top and middle layers switching up and down simultaneously during the transitions. At first this sounds like a big coincidence but is possible with the aid of mutual dipole coupling between top and middle layer. The idea is, even though top and middle layers may have different coercivity field, once the layer with the smaller coercivity field switches first, the modified dipole field will trigger the switching of the other layer as well. The field at which the right-hand-side hysteresis transition occurs is defined as H_t. This will be referred again in "microwave emission at finite field" section to pinpoint the direct correspondence between this and a key observation made in the aforementioned section.

Having the MR_Z loop explained we move on to MR_Y loop. In fact, this is the remaining MR loop that is required to have explained to conclude the layer structure as the azimuthal asymmetry of this circular device originates from the bottom layer which is in the y-direction. MR_Y shows significant asymmetry around the y-axis. The generic behavior can be understood as follows. The device resistance drops as the field is swept in the positive y-direction. When the field is swept along the negative y-direction, first the resistance increases to the global maximum after which it gradually decreases. Additional minor details present on

the right hand side (small jump down and up of the resistance) are considered be irrelevant to have the basic layer magnetizations assigned. Since the device resistance attains global minimum (as seen in fig. 4.3.d) the bottom layer magnetization is concluded to be along the positive y-direction. Both upward oriented top and middle layer magnetizations gradually tilt along that of the bottom layer causing the device resistance to drop. On the other hand, when the field is swept in the negative y-direction, top and middle layer magnetizations start to tilt in the opposite direction to that of the bottom layer. The initial increase in the resistance is explained as follows. As the field is swept in the negative y- direction, top layer will tilt at a faster rate than the middle layer as the middle layer has higher IPMA field. During this process both R_1 and R_2 (as defined in fig. 4.1.d) will increase until the total resistance reaches the global maximum. When the field swept further beyond this point, both top and middle layers will eventually settle (top layer first and then middle layer) along the negative y-direction hence bringing the mutual angle between them back to zero. During this process R_1 will decrease but R_2 will still continue to increase. However, the resistance-area product (RA) for R_1 is higher than that for R_2 (fig. 4.1.a) therefore causing the final resistance to decrease.

After having both MR_Z and MR_Y loops explained, the MR_X loop shall also be considered even though, MR loop along such direction (direction along which non of the layer magnetizations are aligned) is not included in published work. As the field is increased in both positive or negative x-directions the resistance is observed to decrease. For the MR_Z loop explanation, the bottom layer was assumed to not tilt much along the out of plane as it is pinned. The argument is valid for MR_X explanation as well. However, since the bottom layer has easy-plane (since the device is circular), it is reasonable to expect that even though it is small, the horizontal tilting of the bottom layer would be more than the vertical tilting for MR_Z loop. This is required to explain the MR_X loop. The decrease of resistance along both field directions in MR_X loop can then be justified as shown in fig. 4.3.a. In fact, near zero-field the decrease of resistance is quite small and becomes significant only when the field becomes higher which is consistent with the above explanation. Also from fig. 4.3.d it can

be seen that, the dynamical TMR of MR_X is somewhat larger than that for MR_Z but still significantly less than the range seen in MR_Y loop. This is again consistent with having the tilting of bottom layer in the above MR_X explanation.

This concludes the resolving of the tri-layer magnetic structure validated with consistently explaining all three axis MR loops. We now continue to analyze the emission data which has promising features in the interest of real world application.

4.2 Microwave Emission at Zero and Finite External Field

As have explained in the theoretical background chapter, STT is capable of driving stable precessions of a nanomagnet [25, 26]. Once the bias current is above the critical current, STT, which opposes in direction to damping for that particular current direction, can overcome the damping, facilitating Larmor precessions of the magnetization around the local effective field [78]. During such a precession, the average energy dissipated in the system via damping is replaced by the average energy provided by STT. In this section of the chapter I will present the results of microwave emission experiments obtained for the tri-layer structure followed by the explanation. Emission has been recorded for many devices with varying parameters which have shown qualitatively similar behavior. First of all, I will present the experimental observations as they are, noting down key features prior any explanations. After, I will proceed to explain the physics behind each of those key features observed.

In fig. 4.4.a, microwave emission recorded for some select devices are shown. Emission has been observed in both current directions which will later be emphasized as one of the key significances of these devices compared to the work reported by others. Emission trace resembles an inverted parabola that is slightly shifted towards the positive current direction. As a result, the magnitude of critical current (current at the onset of emission) for positive current direction is slightly higher than that for negative current direction which will formally be derived later in this chapter. Furthermore, for a given current magnitude, the frequency offered from a positive current is slightly higher than that from a negative current. Redshift

of frequency with magnitude of current is present for both current directions along with an increase of the emission power. To choose the range of the bias current for an emission experiment, first the current is swept in a particular direction while monitoring the voltage across the device. The typical breakdown voltage of a 1nm thick MgO tunneling barrier is about 1V [79]. Since this device has two such barriers in series, 2V can be assumed to be a safe boundary. However, to be on the safer side, current for each device was limited not to exceed 1V across the device. Further increase of current was done for some devices and many of them burnt out well below 2V. In some of the emission plots, at the end of the inverted parabola shaped emission, a sudden increase of emission power is observed. However, this emission is relatively much lower in frequency with a very broad peak. For these reasons, this part of the emission has no interest in practical applications but can be useful in understanding the dynamics of the precessions inside. Usually such discontinuous and qualitatively different emission appearing in the spectrum is attributed to the onset of a different mode of incoherent oscillations. Even for the devices that have not produced such broaden emission at the spectrum ends, they are expected to do so if the current is further increased and the device survived. Furthermore, in some emission recordings, a slight discontinuity (a drop) of the emission frequency can be observed as is present in the top left plot of fig. 4.4.a (in the negative branch). It turned out that, every device is capable to produce that signature once initialized with either a high current or a high vertical field with a specific polarity prior recording the emission. In fact, this is the indication of current induced switching (CIS) of the device between the states of 'state-1' and 'state-2'.

As mentioned above, such bidirectional emission has been recorded for numerous devices. Fig. 4.4.b, c and, d summarize the maximum emission frequency of a particular device in the context of the middle and the top layer thicknesses respectively. Blue stars and red squares represent data taken from devices from different wafers. In Fig. 4.4.d., maximum frequency variation on top layer thickness same as (b) but zoomed in with in the range of 1.35 nm and 1.5 nm. Device of which the emission is reported in the latter part of this chapter is denoted. Orange rectangular region is included for context presenting the frequency reported

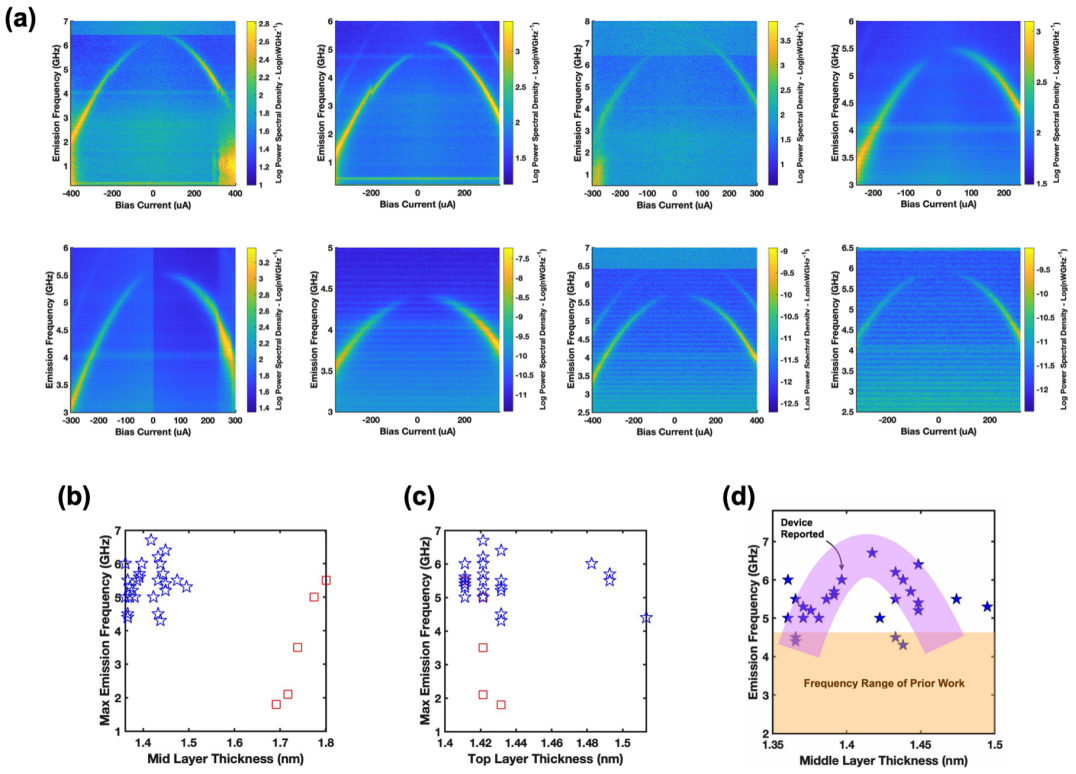

Figure 4.4: Microwave emission at zero bias-field. (a) Microwave emission spectrum for both current polarizations for various devices with different parameters. (b) Maximum frequency variation on middle layer thickness. Blue stars and red squares represent data taken from devices from different wafers. (c) Maximum frequency variation on top layer thickness (d) same as (b) but zoomed in with in the range of 1.35 nm and 1.5 nm only. Device of which the emission is reported in the latter part of this chapter is denoted. Orange rectangular region is included for context presenting the frequency reported in prior work conducted at zero bias field.

in prior work conducted at zero bias field. The attempt was to infer a correlation between the max frequency and layer thickness but unfortunately such correlation could not be seen. The motivation for this exercise is, the emission frequency is proportional to the local field of the precessing layer (top or middle or both) and the interfacial perpendicular anisotropy (IPMA) of such thin layers directly depends on their thicknesses. However, defects can again play a significant role here. Defects, grain roughness, material diffusion can affect the local magnetic properties inside the already ultra thin layers sometimes causing magnetically dead regions. In such a case, the effective thickness of a layer is less than its physical thickness [40]. Furthermore, the IPMA of these devices solely originate from the CoFeB/MgO interfaces and hence susceptible to the interface quality. A typical consequence is that, even though the middle layer has two such interfaces hence theoretically the IPMA should be as twice as that for a single interface but, work has been reported where the IPMA of a layer sandwiched by two MgO layer (hence two interfaces) is in fact less than the theoretical predicted value and sometimes even less than that from a single interface [40]. In such cases, the cause is attributed to the bad quality of the CoFeB/MgO interface in terms of uneven interface plane, defects, grain roughness or/and material diffusion. Therefore such conditions could have indeed buried any correlation expected.

In Fig, 4.5 detailed observations are presented on a select single device emission. Fig. 4.5.a presents the bidirectional emission below which the calculated emission power and simultaneously measured device resistance (Fig. 4.5.b) are presented aligned for comparison. In the emission plot, a sudden broaden but increased in power emission is present for both current directions. This event on the positive current side has occurred at a relatively lower current magnitude than that on the negative current side. The vertical dash line serves to pinpoint the simultaneous footprints at the emission power and device resistance at the onset of this secondary mode (broaden, low frequency and high power). At the occurring of this event, a noticeable discontinuity is present for both emission power and device resistance. Specifically, a chaotic behavior can be noticed in the device resistance plot suggesting incoherent dynamics in the active (precessing) layer. Furthermore, as the magnitude of the current is

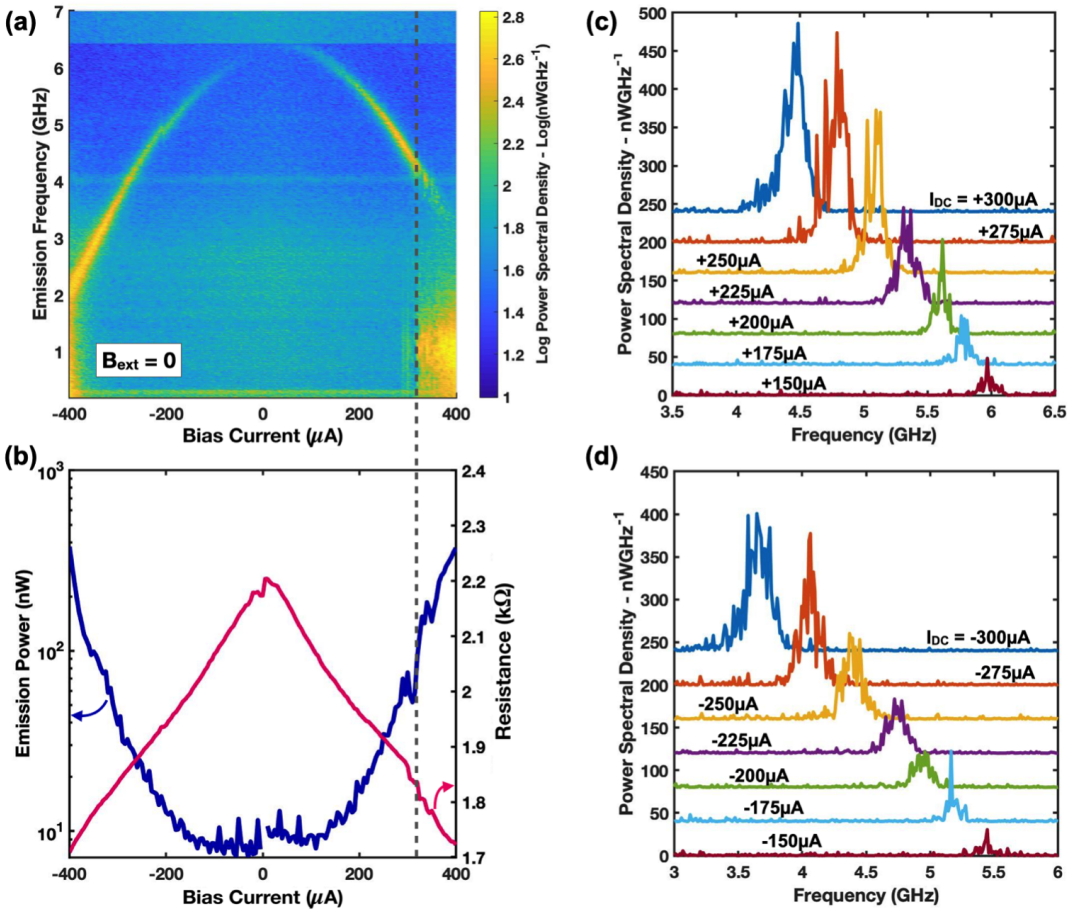

Figure 4.5: Microwave emission at zero bias-field. (a) Microwave emission spectrum for both current directions. (b) Integrated power delivered to a matched load (left axis) and, simultaneous resistance measured during experiment (right axis). Vertical dash line is included as a guide to identify the footprints at onset of incoherent emission. (c) Individual traces of the emission in the frequency domain for select positive bias current values. (d) Individual traces of the emission in the frequency domain for select negative bias current values.

increased in both directions, a significant drop in device resistance has occurred which is near symmetric around zero bias current. It should be emphasized that, this drop in resistance is significantly larger than the dynamical resistance change (or range) for both MR_X and MR_Z loops. This suggests increase of the current magnitude, significantly tilts the magnetization of the precessing layer causing significant changes in the mutual angles between the layer magnetizations that are not occurring for MR_Z or MR_X loops. This fact will later be used to understand the oscillation modes for example, in-plane oscillations or out of plane oscillations. In Fig. 4.5.c and d, individual emission traces (each corresponding to a vertical segment in the spectrum) for both positive and negative bias currents are shown. The traces are vertically offset with a constant gap for clarity. The redshift in frequency and the increase of emission power are again observed with these traces.

Having zero bias field emission presented, I continue to present the observations made on the emission manipulated with an external field applied along z-direction. For real world applications, having to apply an external bias field is least favored. That being said, it should be emphasized that, the motivation behind these set of experiments is to investigate in to the oscillation modes based on the device's response in emission to an external field. As foreseen, this section is feature rich and careful attention has been given to infer the hidden facts needed. Fig. 4.6 summarizes the observations obtained for two select devices. Fig. 4.6.a, b and c are from one device and Fig. 4.6.d is from a different device. For all the devices studied, two major behaviors are observed each occurring with a certain initialization namely, either applying a large vertical positive or negative field prior to the experiment. First kind of the behavior (behavior number one), Fig. 4.6.a, is a continuous linear blueshift in frequency with the applied vertical field which occurs upon a positive vertical field initialization. Second, Fig. 4.6.b, is a linear redshift followed by a discontinuous frequency jump which then followed by a continuous blueshift (behavior number two). For both of these figures, for the emission recording, external field is swept in the positive direction. However, if the device is initialized with a positive field after which the emission is recorded for field sweeping in the negative direction, behavior number two (redshift and the blueshift) is observed.

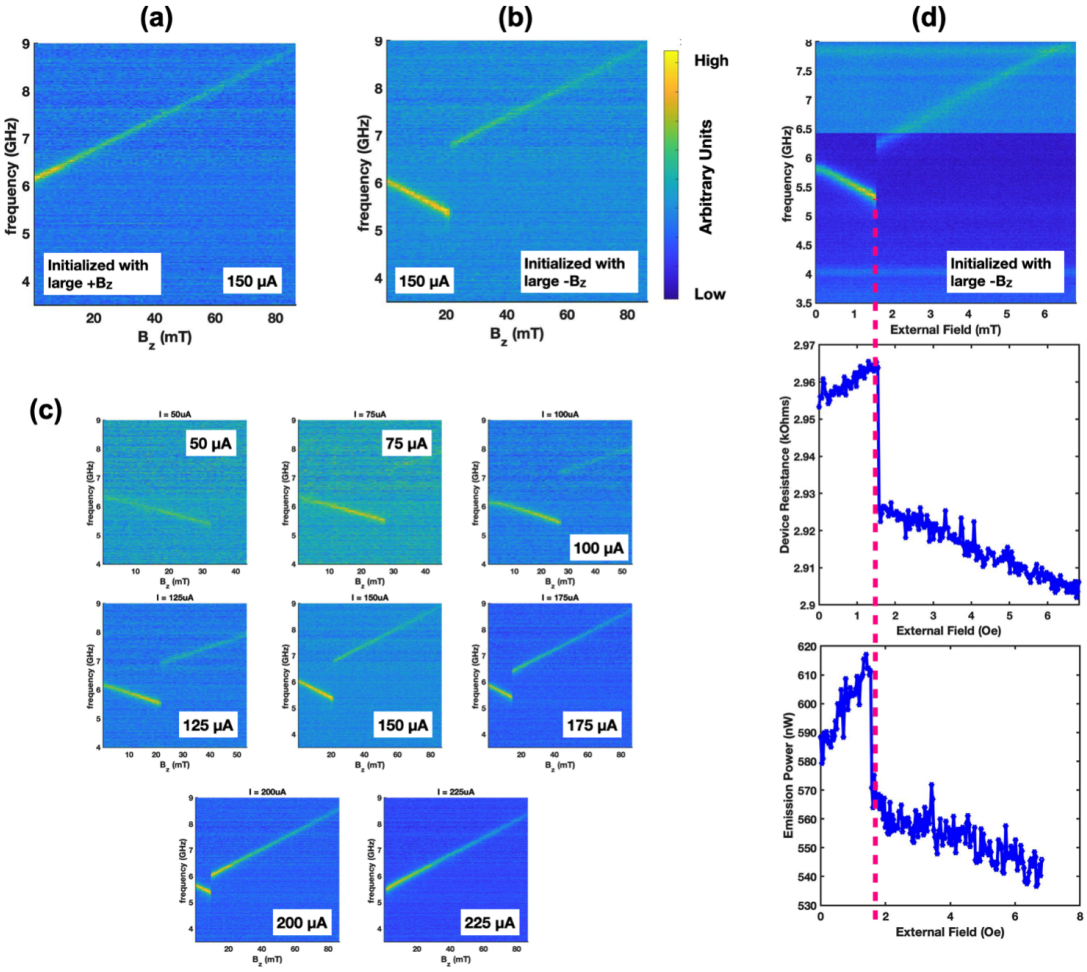

Figure 4.6: Microwave emission at finite bias-field upon different initializations. (a) Device initialized by large $+B_z$ field and then emission with B_z swept in positive direction for a bias current of $+150\ \mu A$. (b) Device initialized by large $-B_z$ field and then emission with B_z swept in the positive direction for a bias current of $+150\ \mu A$. (c) Large $-B_z$ field initialized emission evolution for positive B_z field sweep for different bias currents. (d) Data from a different device than for a, b, and c. $-B_z$ initialized emission evolution for $+B_z$ sweep at a bias current of $+125\ \mu A$. Simultaneously measured device resistance and calculated power plot shown below for comparison.

Another key feature observed is, for the second-kind behavior (with a negative field initialization), the field at which the discontinuity occurs depends on the bias current under which the emission vs external field is obtained at. This field at the discontinuity is named as "transition field" and will later be referred in explaining the dynamics. Fig. 4.6.c illustrates the emission vs external z-field plots obtained upon negative field initialization for different bias current values. First thing to notice is that, starting from a lower bias current, as the current increases, the transition field decreases. It was found that at $+205\ \mu A$, even upon negative field initialization, the behavior number one is present. Later this will be put in direct comparison with MR_Z loops obtained at different bias currents. Fig. 4.6.d shows the evolution of the emission power and simultaneously measured device resistance through the behavior number two. The segment of the redshift corresponds to a monotonic increase in both device resistance and emission power. In contrary, blueshift corresponds to a monotonic decrease in both device resistance and emission power. This observation will later be used to explain the evolution of the precession cone angle in response to an external vertical field, hence revealing the primary nature of the cone itself in the zero-field setting.

4.3 Explanation for Experimental Observations

Once the observations have been made, I continue to explain the physical dynamics inside the device to explain the emission produced by this tri-layer device. The key features to be explained are bidirectional emission and producing high frequency emission at zero external bias field.

Conventional bilayer MTJs come in various structures in terms of layer magnetization orientations. Namely, "in-plane collinear" where both fixed and free layers are in-plane and collinear, "out of plane collinear" where both fixed and free layers are out of plane and collinear, "in-plane out of plane orthogonal" where fixed layer is in-plane but the free layer is out of plane hence mutually orthogonal and finally, "out of plane in-plane orthogonal" where fixed layer is out of plane but the free layer is in-plane. It should be mentioned that in orthogonal devices, the free layer is usually tilted out from the axis owing to the mutual

dipole coupling between fixed and free layers. Thermally induced microwave emission is available in any of these devices at low current regime for both current directions however, the emission power is usually in sub 1 nW range [80]. In contrast, STT induced microwave emission is observed only for one current direction. The reason lies in the mechanism of how STT facilitates Larmor precessions which then produces the microwave output. The Larmor precession will occur whenever the magnetization of the precession layer is tilted away from the local field. However, in the absence of STT, such a tilted away magnetization will precess but losing the energy to dampening, will eventually settle in to its equilibrium position. Given this picture, STT is capable of counteracting this damping torque in specific cases hence maintaining a persistent tilt-away of the magnetization hence making persistent oscillations possible. In a simple circular geometry without any higher order anisotropy terms, STT is collinear with the damping torque and is either parallel or anti-parallel depending on the direction of the current flow. Even with non-circular geometries (elliptical) and with higher order anisotropy terms, overall effect of STT can still be understood either as enforcing or as overcoming the inherit damping in the system depending on the direction of the current. The aforementioned persistent tilt-away is possible whenever the direction of the current is right such that STT overcomes the damping. In the other current direction, STT having added to damping, increases the effective damping leaving the magnetization virtually immobile. This explains the reason as to why STT induced microwave emission is present only for one current direction for a conventional bilayer MTJ. Therefore one of the important features of this tri-layer device is offering bidirectional emission along with emission power up to 60 nW which is well above what thermally induced emission can offer.

Resolving the MR loops, it is understood that, the bottom layer is almost fixed in-plane and both middle and top layers have PMA hence are vertical. The top is expected to be practically vertical while middle layer is expected to be tilted out towards the fixed layer due to the dipole coupling. In a conventional bilayer orthogonal MTJ such a tilt is about 10 degrees [25, 26]. However, for this tri-layer device, the middle layer already having high IPMA field of its own and also being under the dipole coupling from the vertical top layer,

this tilt angle is expected to be much less than 10 degrees as mentioned earlier in this chapter.

Having two unpinned layers (top and middle compared to stiffen bottom), in the attempt to explain the bidirectional emission, one suggestion could be that, one out of the top or middle layers oscillates for one current direction and the other layer oscillates for the other current direction hence producing STT induced persistent oscillations in both current directions. However, in the emission plots obtained for all devices, the emission peak frequency is continuous around zero current. Of course the emission is not present near around zero current yet, above claim can be justified by visualizing the aforementioned inverted parabola in Fig. 4.5.a. The emission frequency is directly proportional to the local field present in the precessing layer [81]. This suggests that, if both top and middle layers are precessing each for each current direction, then the local field inside both the layers at zero current should be the same. This is a big coincidence to be true for all the devices studied. Hence this eliminates the possibility of two different layers precessing at a time to produce bidirectional emission. Therefore to continue on, only one out of top or middle layers is considered to produce emission for both current directions.

Next thing to pay attention is to precessional modes which can be qualitatively categorized as either in-plane oscillations (precession cone with horizontal axis) or out-of-plane oscillations (precession cone with vertical axis or tilted axis) [5]. Certain MTJ structures are capable of one or both of these kinds depending on the fixed/polarizing layer direction, free layer anisotropy, magnitude of the current and presence of an external bias-field. Argument to narrow down the precessional modes are presented in Fig. 4.7. It turns out that, in-plane precessional modes cannot successfully explain the observed behavior of emission upon external vertical field manipulation, however, out-of-plane oscillation modes can consistently explain all the features as illustrated with insets of Fig. 4.7.a and b. Considering OOP precessional modes observed redshift and blueshift is explained as follows. For device in state-1 with a field applied upwards, magnitude of internal field (B_{int}) is $\mu_0(H_k - M_S)m_z - B_z$ where H_k, M_S, m_z and B_z are IPMA field, saturation magnetization, vertical magnetization component and external field respectively. For state-2 with B_z remaining upwards, this is

modified to $\mu_0(H_k - M_S)m_z + B_z$. Increase of B_z will decrease the magnitude of B_{int} in former case while the opposite will occur in the latter. Oscillation frequency being directly proportional to B_{int}, redshift branch in Fig. 4.7.a can thus be explained. At the end of this redshift, device undergoes field induced switching (FIS) after which the oscillation cone will point upwards where B_{int} will now increase with B_z leading to the observed blueshift. As seen in Fig. 4.7.b., in contrast, device starts off in state-2 (cone upwards) hence no FIS will occur explaining the monotonic blueshift with B_z. Since I_{DC} is held constant, observed (in Fig. 4.6.d.) increase (decrease) in emission power along redshift (blueshift) suggests an increase (decrease) in dynamical TMR during precessions, meaning an increase (decrease) in cone angle. Such increase (decrease) in cone angle does decrease (increase) m_z leading to a decrease (increase) in B_{int} which will further enhance the existing redshift (blueshift). However, this contribution from cone angle evolution is expected to be dominated by that from change in B_{int}.

Furthermore, MR_Z loops for different I_{DC} are obtained and are presented in Fig. 4.7.c. For both cases, corresponding H_t values are derived as defined in Fig. 4.3.c and Fig. 4.7.a. It turns out that H_t derived via both of these methods decrease with increase of I_{DC}. This is explained as follows. With increase of I_{DC}, STT rotates the magnetization further away from vertical axis hence facilitating the completion of the switching at a lower external field than otherwise. In fact it is found for I_{DC} greater than 200 μA (at around 205 μA), only the continuous blueshift is present even upon state-1 initialization indicating the current itself has completed the switching without any aid of external field. Comparison of H_t derived from these two independent methods demonstrates good correlation as seen in the inset of Fig. 4.7.a., suggesting the specific event of switching from redshift to blueshift directly corresponds to the switching event on the MR_Z loop which further validating the OOP oscillation model. It should be mentioned that, all the data presented in fig. 4.7, are for positive bias currents however, same set of features have been observed for negative currents as well. These together suggest, the precessional modes for both current directions are out-of-plane.

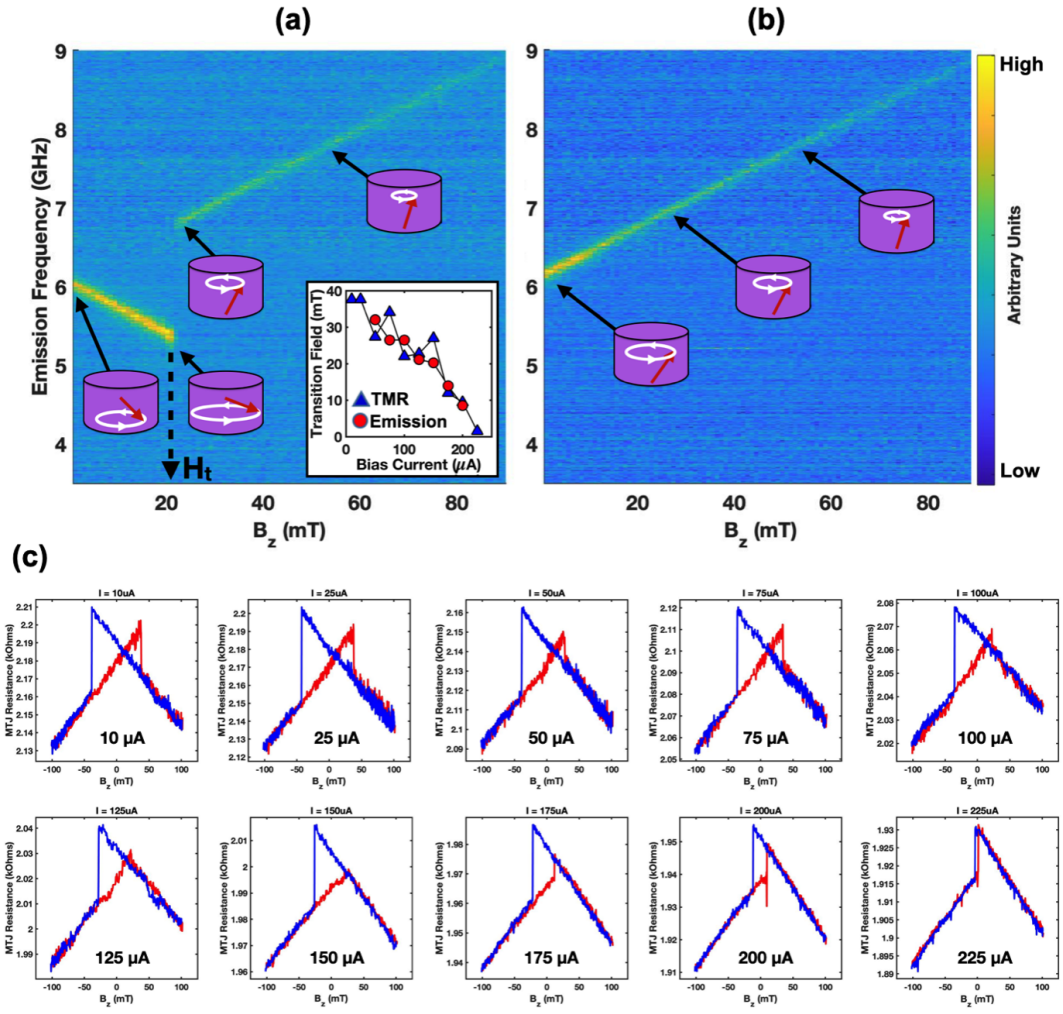

Figure 4.7: Manipulation of the emission with z-field at a fixed bias current of 150 μA. (a) Emission frequency vs B_z upon state-1 (negative large B_z) initialization. Insets of the precessing layer illustrate the evolution of the cone angle which has been exaggerated for clarity. Definition of the transition field H_t is shown. Inset plot presents the correlation between the transition fields at different bias currents derived from emission cone flipping method and magnetoresistance measurements. (b) Emission frequency vs B_z upon state-2 (positive large B_z) initialization. Insets of the precessing middle layer illustrate the evolution of the cone angle. (c) MR_Z loops obtained at different bias currents to derived MR_Z loops based H_t as defined in Fig 4.3 .

So far I have narrowed down to the following two conclusions. For both current directions, only one out of either top or middle layers are precessing producing the emission. Whichever that layer is, the oscillation modes are out-of-plane for both current directions. The next task is to figure out which layer (out of top and middle) in fact is precessing for both current directions. To proceed, I eliminate the case where the top layer precessing producing emission with the following indirect argument. When the magnetization of the free layer in an MTJ precesses while an adjacent layer is fixed (i.e still) , a time varying resistance is built up as a result of TMR. Since the bias current is already passing through the device, this oscillating resistance is then converted in to an oscillating voltage signal via Ohms law. This is the produced microwave signal. However in certain conditions, a noticeable resistance oscillation will not be built up even with a significant free layer oscillation. The explanation goes as follows. The resistance of an MTJ depends on the mutual angle between the two layers. Consider the situation where the fixed layer vertical and free layer perform out-of-plane oscillations with the precessing cone axis being near vertical. In this situation, regardless of the free layer precession, the mutual angle between the fixed and the free layers is fairly constant which is the half cone angle of the precession cone. Same happens with in-plane fixed layer and free layer oscillating with the cone axis parallel to the fixed layer (i.e in-plane oscillations). In these situations, regardless of the free layer precession, the device resistance does not pick that oscillating signature hence will not produce any microwave signal. This is exactly the situation for this tri-layer device if the top layer is claimed to perform out-of-plane precessions while the middle remaining fairly vertical. The dynamics of top layer precession on a vertical cone will be left unnoticed by the TMR with the middle layer hence producing no emission. (There can be small TMR coupling between the bottom and the top layers due to the finite partial spin polarization/modification of the middle layer. However such indirect TMR cannot be as comparable to a direct TMR hence fails to justify the fairly equal emission power on either sides of the current directions.) In contrary, emission is present for both current directions in the observations. Therefore this leaves the picture with the only other option where the middle layer precess. When the middle layer precess out-of-plane, while having the bottom layer fixed in-plane and adjacent, the latter can successfully act as a

monitoring layer to the former hence resulting in microwave emission. In other words, during the out-of-plane precession of the middle layer (in both current directions), the mutual angle between the middle and the bottom layers changes significantly resulting in a high TMR variation. Therefore, the near symmetry of the power around zero current can be justified.

The final combined conclusion of all the above arguments is that, for both the current directions, the middle layer precesses while the bottom layer acts as the monitoring layer. In literature such layer is also called as an analyzer, readout, recording or reference layer. Now the task is to explain the spin transfer dynamics in this tri-layer device to explain the precession of the middle layer for both current directions. The equation governing the magnetization dynamics in a STT device is described by the well known Landau–Lifshitz–Gilbert–Slonczewski (LLGS) equation. The equation is as follows.

$$\frac{d\overrightarrow{m}}{dt} = -\gamma\left(\overrightarrow{m} \times \overrightarrow{H}\right) + \alpha\left(\overrightarrow{m} \times \frac{d\overrightarrow{m}}{dt}\right) - \gamma H_s\left[\overrightarrow{m} \times (\overrightarrow{p} \times \overrightarrow{m})\right] - \gamma\beta H_s\left(\overrightarrow{m} \times \overrightarrow{p}\right) \tag{4.1}$$

where

$$H_s = \frac{\hbar\eta I}{2e\left(1 + \lambda\overrightarrow{m} \cdot \overrightarrow{p}\right) M_S V} \tag{4.2}$$

m - unit magnetization vectors of the free layer p - unit magnetization vectors of the fixed layer

H - local magnetic field

γ - gyromagnetic ratio

α - Gilbert damping parameterh

H_S - spin transfer strength

β - ratio between the spin transfer torque and the field-like torque

I - current

e - magnitude of the electron charge

M_S - saturation magnetization of the free layer

η - spin polarization efficiency

λ - parameter determined by the device structure and geometry

The first term on the right hand side of the LLGS equation is the well known Larmor precession torque which causes a magnetic moment tilted away from a magnetic field to precess around the latter. The second term accounts for the intrinsic dampening in a dissipative system. The third is the in-plane spin transfer torque (STT) term. The fourth term is the field-like torque term. The origin of this is as same as of the in-plane spin transfer torque, but has been named as such due to its similarity to a torque created by a magnetic field (compare with the first term). Here H_S is the spin transfer strength of the system which depends on the device structure (collinear or orthogonal), free layer dimensions (volume), material parameters (free layer saturation magnetization), spin polarization efficiency of the fixed layer and finally the instantaneous angle between the free and polarizer layer magnetizations (i.e. $\overrightarrow{m} \cdot \overrightarrow{p} = cos(\theta)$). Here, λ contains the information of the device structure and other geometrical parameters, where it can either be positive or negative while the former is the case for most reported work. It should be mentioned that this formalism looks different from that presented in chapter two however are identical in physics. Above formalism will be used to proceed with this chapter to avoid confusion with the relevant prior work published that are used to explain the spin dynamics of the tri-layer MTJ.

Given this picture, I will continue to explain the possibility of bidirectional emission as a result of both top and bottom layers acting on the middle. To proceed, STT effects on the middle layer by top and bottom layers will be considered separately before putting the entire picture together. To start with, first the STT interactions between the top and the middle layer are considered. As middle layer is already concluded to be the precessing layer, let's consider it as free layer while the top acting as a polarizer. This picture containing just top and middle layers falls under the category of out-of-plane collinear MTJs. As described in the experimental setup, the current is taken to be positive when the electrons are traveling from the bottom to the middle to the top layer.

Accounting for the STT between top and middle layers, when the electrons are traveling

from middle to top (i.e. positive current), the STT on the middle by the top will try to tilt the magnetization of the former away from that of the latter. This is because, assuming both top and middle layers initialized to be vertical up (state 2), the reflecting electrons from the top/middle interface back into the middle layer are downward spin polarized (due to the top layer being vertical up) injecting STT in the downward direction. This downward spin injection on the middle layer (while being vertical up) will try to reorient its magnetization to be vertical down (i.e to be anti-parallel to the top layer). If this reflecting spin injection is strong enough, the middle layer will completely flip settling into its so called "anti-parallel (AP)" position (current induced switching) but, if it is significant enough yet not large enough to complete the switching event, the middle layer magnetization would remain tilted to the vertical axis (of course in a precessing dynamical equilibrium in the context of the whole picture). This argument is valid for state-1 initialized case as well where both top and middle layers initialized to be vertical down. In the meantime, whenever the magnetization is away from its equilibrium position (hence initiating Larmor precession making '$\frac{dm}{dt}$' non zero), the damping torque comes into play. Being dissipative in nature, the damping torque will always try to bring the magnetization back to its equilibrium position. Therefore to put both STT and damping effects together, STT on the middle magnetization tries to take it away from the equilibrium (vertical axis) while damping tries to bring it back. This is illustrated in Fig. 4.8.a and b for both initializations. Given this picture, if the STT is greater in magnitude than the damping, a sustainable tilt angle is possible leading to sustainable self oscillations. On the other hand, if former is smaller in magnitude than the latter, damping will dominate to bring the magnetization to be vertical up or down depending on the picture (in general to its original equilibrium position). The conclusion is that, STT by the top on the middle layer can support self oscillations when the electrons are flowing upward (positive current) if the current is large enough for the STT to overcome damping, i.e. if the current is about the critical current.

Now consider the case for the negative current direction where the flow of the electrons will be from the top to the middle layer. In this case, electrons flowing through the top layer

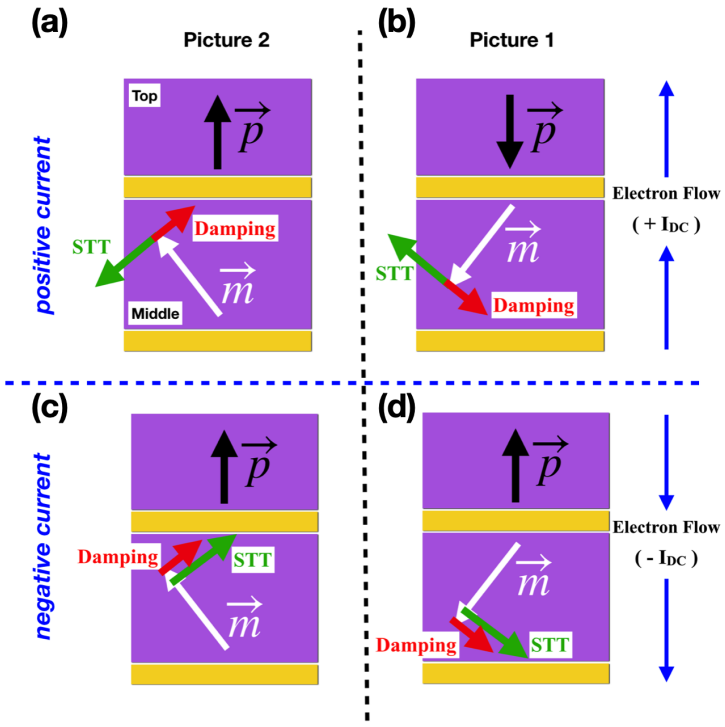

Figure 4.8: Spin transfer torque dynamics between the top and the middle layers. First (second) column is when the device is initialized with a large vertical up (down) field. First (second) row is for positive (negative) current where the electrons are flowing from the middle (top) layer to the top (middle) layer. (a), (b) In this situation, STT on the middle by the top layer tries to tilt the former's magnetization away from the latter, therefore as a result, STT is opposite in direction to the damping torque. This is the case where STT suppresses the effective damping and once the former's magnitude is greater than the latter's, the free layer magnetization will sustain a finite tilt angle resulting in self-oscillations. (c), (d) In this situation, STT on the middle by the top layer tries to align the former's magnetization parallel to the latter, therefore as a result, STT is in the direction as of the damping torque. This is the case where STT enhances the effective damping and the free layer magnetization becomes immobile.

get spin polarized in the vertical up (down) direction in picture 2 (1), injecting corresponding STT into the middle layer in up (down) direction. In this situation the direction of the STT along with the damping is shown in fig. 4.8.c and d. In contrast to the previous case where STT opposes damping, here STT is aligns in parallel to the damping hence enhancing the effective damping. Therefore any initial tilt of the middle layer magnetization will be brought to its equilibrium position more rapidly than with the damping alone. The conclusion is that, STT by the top on the middle layer creates a damping effect (hence no self oscillations) when the electrons are flowing downwards (negative current) regardless of the magnitude of the current.

Having the STT effects by the top on the middle layer qualitatively understood, I move on to examine the STT effects by the bottom on the top layer. For this purpose, the middle and bottom layers will be taken alone which falls into the category of out-of-plane free layer, in-plane fixed/ polarizer orthogonal structure. T. Taniguchi et. al. 2014 [82], have reported a comprehensive computational study for this case which I will refer to in the following section.

Without the field-like term included in the LLGS equation, simulations have shown that self oscillations are not possible in orthogonal devices (in this case, out-of plane free layer and in- plane polarizer) unless applying an external magnetic field. However, once the field-like term is included, T. Taniguchi et. al. has shown that the device can support self oscillations under certain circumstances. They have conducted macrospin simulation (entire free layer to behave as single spin/ magnetic moment) for a circular device where the STT torque is either parallel or anti- parallel to damping depending on free layer magnetization position. However, in general case, even for non-circular devices and for micromagnetic simulations, STT can still be understood as either enhancing or suppressing damping on average over precessions. Therefore the results predicted in the above study are still qualitatively valid for the general situation. On the other hand, the devices studied in my work are indeed circular and are of the size of 80 to 100 nm which is small enough to be single domain (apart from defects). Therefore it is reasonable to expect that the results derived by T. Taniguchi

et. al. can qualitatively explain the dynamics between the middle and the bottom layers of my device.

T. Taniguchi et. al. has studied the possibility for self oscillations for various cases regarding 'β' (ratio between the field-like torque and STT). The signed numerical value of 'β' can either be equal to zero or greater or smaller than zero as shown in Fig. 4.8. When $\beta = 0$ (i.e. with no field-like torque included), and when $\beta > 0$, the average energy dissipated by damping is greater than that input by STT. On the other hand, when $\beta < 0$, the average energy dissipated by damping is smaller than that input by STT hence facilitating self oscillations. In the first two cases, as shown in Fig. 4.9.a and b, the free layer would temporarily precess after which it is settled into the anti-parallel (AP) state. On the other hand, for $\beta < 0$, as shown in Fig. 4.9.c, self oscillations are sustained. This condition on 'β' to be negative is required for self oscillations in such a structure regardless of the current direction. That being settled, the authors investigate into the two possible current directions to see which can persist self oscillations. It has turned out that, the required sign of the current does depend on 'λ' which as mentioned earlier depends in the structure, geometry and material parameters. They have found that, for $\lambda > 0$, a current where electrons flow from free layer to the polarizer would produce self oscillations while for $\lambda < 0$, electrons flow from polarizer to the free layer would produce self oscillations. Prior reported work regarding simulations on MTJs similar in structure and layer thicknesses to my middle/ bottom layer combination (i.e. CoFeB/MgO/CoFeB orthogonal MTJ) have used $\lambda > 0$ to successfully reproduce experiment observations [14, 83]. In-fact in some cases 'λ' is taken to be the square of the spin polarization efficiency (i.e η). Therefore I use the results of T. Taniguchi et al under $\lambda > 0$ to continue on the explanation.

The conclusion is that, when the electrons flow from middle (free) to the bottom (polarizer) self oscillations are possible while for the other current direction, STT will contribute to enhance the damping. Having the dynamics between the top/middle and middle/bottom considered separately, I will continue to put the entire picture together to explain the observed high power, high frequency and current bidirectional STT emission of these tri-

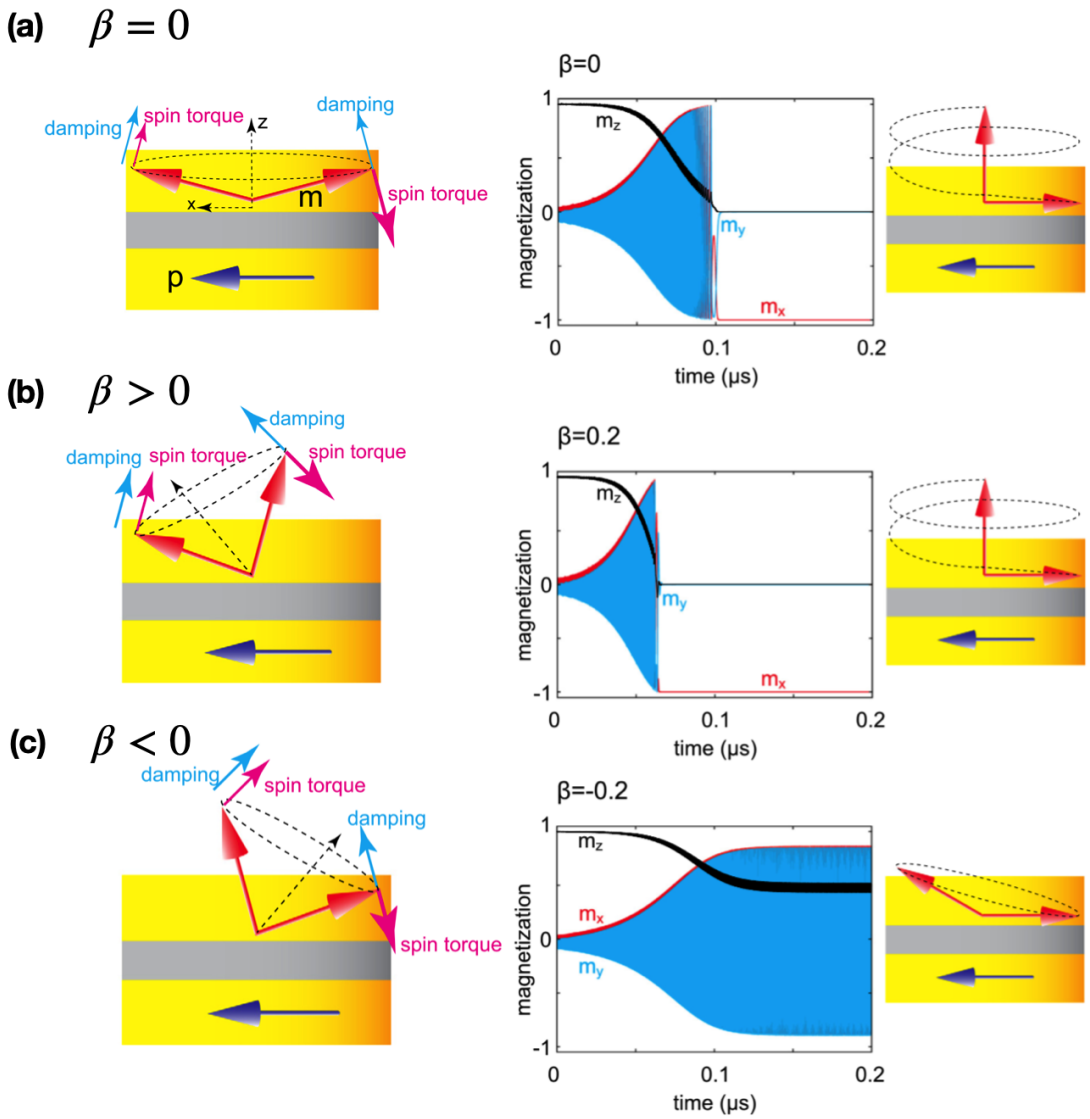

Figure 4.9: (After T. Taniguchi et al 2014) Magnetization precession picture for self oscillations for different values which is the ratio between the field like torque the spin torque. The directions of the spin torque and the damping are indicated by red and blue arrows, respectively. The spin torque strength near the anti-parallel alignment of m and p is larger than that near the parallel alignment for $\lambda > 0$ which is as defined in the main text. (a) Schematic view of the magnetization dynamics in the absence of the field-like torque, i.e. $\beta = 0$. (b) magnetization dynamics with the field-like torque and $\beta > 0$. (c) with $\beta < 0$.

layer devices. The picture constructed in both Fig. 4.8 and Fig. 4.8 are put together in the Fig. 4.10. When electrons flow from top to the middle layer, it exerts STT with a dampening effect on the latter as explained in Fig. 4.8.c and d. On the other hand when the electron flow continues to the bottom via the middle, the reflected electrons (from the middle/bottom interface) exert STT with an anti-dampening effect on the middle as illustrated in Fig. 4.9.c. If the magnitude of the latter is greater than the former plus the intrinsic dampening, self-oscillations could persist. When electrons flow from bottom to the middle layer, it exerts STT with a dampening effect on the latter (following the results of T. Taniguchi et al 2014). On the other hand when the electron flow continues to the top via the middle, the reflected electrons (from the middle/top interface) exert STT with an anti- dampening effect on the latter as shown in Fig. 4.8.a and b. If the magnitude of the latter is greater than the former plus the intrinsic dampening, self-oscillations could persist.

In the created picture, for both current directions, both top and bottom layers will either enforce a damping or an anti-damping effect. The bottom line is, for both current directions, among the two spin torques (coming from top and bottom) injected into the middle layer, one will be a dampening effect while the other being an anti-dampening effect. If the overall anti-dampening is canceled by the effective dampening (intrinsic damping and STT damping), no self oscillations would occur. However, the magnitudes of these STTs, from both top and bottom either as a damping or an anti-damping effect, do depend on the instantaneous mutual angles of the corresponding layer magnetizations. i.e the mutual angle between the magnetizations of top and middle, and that of middle and bottom, which are constantly changing. To make the picture even more complicated, given the top layer is not pinned as the bottom, dynamics can be induced in the top layer as well. However, those dynamics if any, would remain unnoticed since the top layer does not have an appropriate readout layer as mentioned earlier. However, those top layer dynamics do affect the mutual angle between the top and middle magnetizations hence affecting the strengths of the damping or anti-damping STT from the top on the middle. Given this situation, there is significant room for the following scenario. When electrons flow from top towards the

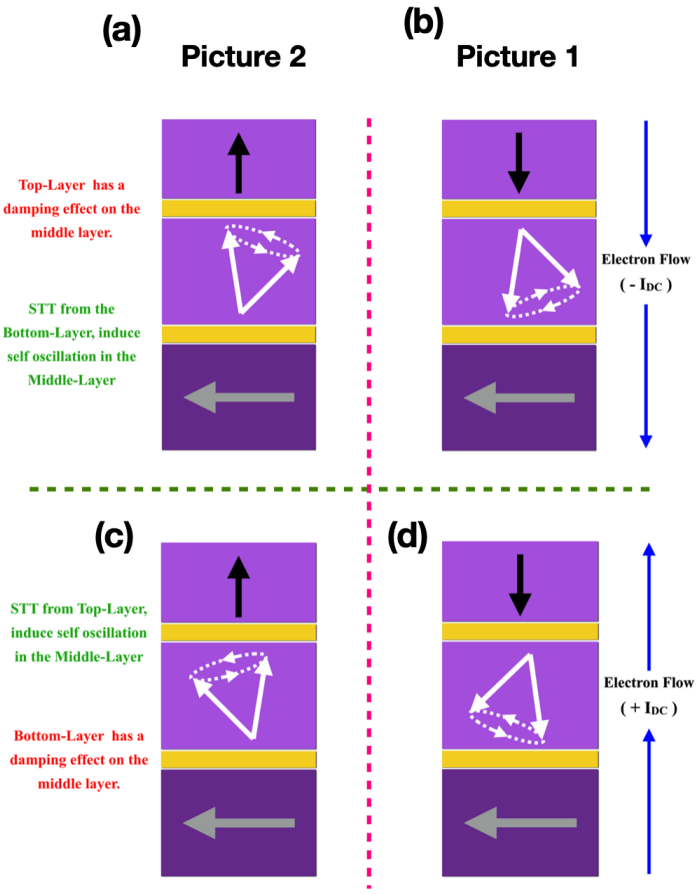

Figure 4.10: Magnetization dynamics of the middle layer for both current directions. First (second) column indicates the case where both top and middle layers having initialized to be vertical up (down) . First (second) row indicates the dynamics where electrons are flowing from top (bottom) layer to the bottom (top) layer. (a), (b) Electron flow from top to middle layer exerts STT with a dampening effect on the latter. On the other hand when the electron flow continues to the bottom via the middle, the reflected electrons exert STT with an anti-dampening effects. If the magnitude of the latter is grater than the former plus the intrinsic dampening, self-oscillations will persist. (c), (d) Electrons flow from bottom to to middle layer exerts STT with a dampening effect on the latter. On the other hand when the electron flow continues to the top via the middle, the reflected electrons exert STT with an anti-dampening effects. If the magnitude of the latter is grater than the former plus the intrinsic dampening, self-oscillations will persist.

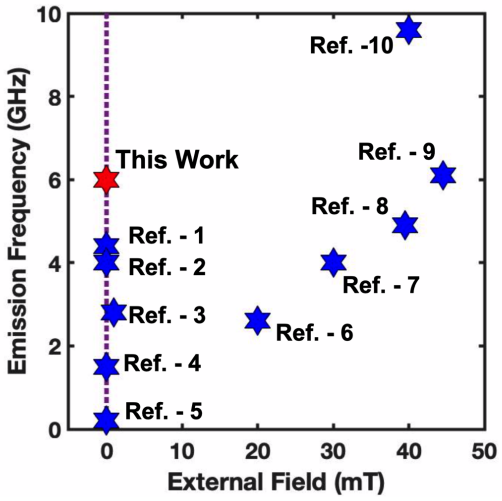

Figure 4.11: Comparison of work presented in this paper with existing work done at room temperature at zero bias field or below 50 mT. The vertical line is a guide for the work done at zero field. Emission studied in this chapter is shown with the red start. References shown in figure 1 through 10 are [11], [12], [13], [14], [15], [16], [17], [18], [19], [20] respectively.

bottom, the strength of the overall STT anti-damping by bottom on the middle is greater than the overall STT damping from the top on the middle therefore leading to sustained self oscillations. On the other hand, for the other current direction, i.e. when the electrons flow from the bottom towards the top, the entire orientation of the cone and other angles will get modified that, the strength of the overall STT anti-damping by top on the middle is greater than that of the overall STT damping from the bottom on the middle therefore leading to sustained self oscillations. To find the exact quantitative conditions to realize this possibility, a detailed micromagnetic simulation is required which will contain two polarizers. The task becomes even more complicated if the top layer dynamics (if any) have to be included hence mimicking a fixed polarizer (bottom layer) and an oscillating polarizer (top layer) in the micromagnetic simulation. Such complicated simulations with two polarizers (one fixed and the other oscillating) have not yet been investigated by any group to date.

Having a qualitative picture in place, it is worthwhile to see how it can qualitatively explain the observed results. The explanations for each observation found on all studied devices will qualitatively be summarized as follows.

4.3.1 Emission frequency being continuous around zero bias current

Middle being the layer responsible for microwave generation for both current directions, the continuity of the inverted parabola around zero current in all emission plots can be explained. Emission frequency is directly proportional to the internal field of the precessing layer [81] hence having the two parts of the parabola from the positive and negative current sides smoothly connecting around zero (for all emission plots on different devices), requires the same layer to be active in microwave generation in both current direction. This is consistent with the concluded picture.

4.3.2 High frequency emission at zero bias field

As already mentioned above, the precession frequency is directly proportional to the internal (local) field of the precessing layer which is middle layer in the concluded picture. In the absence of any external field this relation can explicitly be given as,

$$f = \frac{\mu_0 \gamma}{2\pi}(H_k - M_S)m_z \tag{4.3}$$

where μ_0 is magnetic permeability in free space, H_k is anisotrpy field, M_S is saturation magnetization and m_z is the vertical component of the magnetization of the free layer which may also be written as $cos(\theta)$. Here θ is the tilt away angle of the magnetization from the vertical axis hence the half cone angle of the out-of-plane precession. The effective local field (in the absence of any external field) that was mentioned above is $B_{eff} = \mu_0(H_k - M_S)m_z$. The proportionality constant is $\frac{\gamma}{2\pi} = 28$ GHz/T in relation to Lamor precession formula leading to eq.4.3.

$$H_k = \frac{2K_i}{t_{CoFeB}M_S} \tag{4.4}$$

In MgO based MTJs, owing to IPMA generating from CoFeB/MgO interface, when free layer (CoFeB) thickness is reduced below a certain threshold (typically 1.7 nm), a perpendicular easy axis can be realized leading to a corresponding anisotropy field given by eq.4.4 [40]. Here t_{CoFeB} is the thickness of free layer (CoFeB) to which anisotropy field (H_k) is inversely proportional. Given this scenario, theoretically, anisotropy field can arbitrarily be increased with no bound by reducing free layer thickness and hence enhancing precession frequency as in eq.4.3. However, practically as the layer thickness is reduced, any interface defects present start to dominate comprmising device's overall performance hence introdcing a practical lower bound to free layer thickness which is about 1.3 nm [40]. This leads to a practical upper bound for precession frequency that can be achieved by a single CoFeB/MgO interface.

To overcome this limitation, an additional such CoFeB/MgO has been introduced in the device presented in this thesis. In such situation, IPMA fields generated by each interface is added to each other i.e., in an ideal situation, in the presence of two CoFeB/MgO interfaces, the right hand side of eq.4.4 will be multiplied by a factor of two.

$$H_k = \left(\frac{2K_i}{t_{CoFeB}M_S}\right) \times 2 \tag{4.5}$$

However, practically a complete factor of two is not expected yet a significant improvement can be expected leading to better performance compared to what a single interface can offer. This has allowed us to achieve the highest frequency (6 GHz) reported to date at zero external bias field for an MTJ to the best of our knowledge. We have put this in comparison to some select work [11, 13, 14, 15, 16, 17, 18, 19, 12, 20] reported that are conducted at either zero field or below 50 mT as presented in Fig. 4.11. In the figure, the vertical line is included as a guide for the work done at zero field and emission studied in this chapter is shown with the red star. To repeat, such high frequency at zero bias field is owing to middle layer having two CoFeB/MgO interfaces, hence having significantly large IPMA producing

the large perpendicular field leading to the high frequency. This is again consistent with the derived picture where middle layer producing out-of-plane oscillations to produce recorded microwave emission for both current polarities.

I have studied devices with thicknesses down to 1.35 nm of which observed emission frequency is summarized in Fig.4.4.d. As seen with aid of the included purple belt, a device is likely to offer the highest frequency at around 1.42 nm. In fact I came across some devices that offered emission frequency even higher than 6 GHz (close to 7 GHz) however the data presented here is those of the device (denoted in Fig.4.4.d) that had the best overall performance. Additionally, when the thickness is further reduced close to 1.35 nm no clear improvement is observed instead, many of the devices show lower performance. As mentioned above, this can be attributed to any interface defects that tend to dominate in the low thickness regime.

4.3.3 Near symmetry in emission power for both current directions

When a free layer of an MTJ precesses, as mentioned earlier in this chapter, the microwave signal is the result of having a monitoring/recording layer adjacent to it so the bias current converts the oscillating TMR into an oscillating voltage signal via Ohms law. That being said, the amplitude of the emerging microwave signal or the power of the microwave emission directly depends on the TMR ratio between the precession and the monitoring layer. Observed near symmetry of the emission power for both current directions requires this precession and monitoring pair to be the same for both current directions which is again consistent with the derived picture.

4.3.4 Slight asymmetry in magnitudes of critical current for the positive and negative currents

Critical current is the minimum current required so that the overall STT anti-damping will overcome overall intrinsic damping leading to self oscillations. This critical current is proportional to the spin polarization efficiency of the corresponding polarizing layer [25, 26].

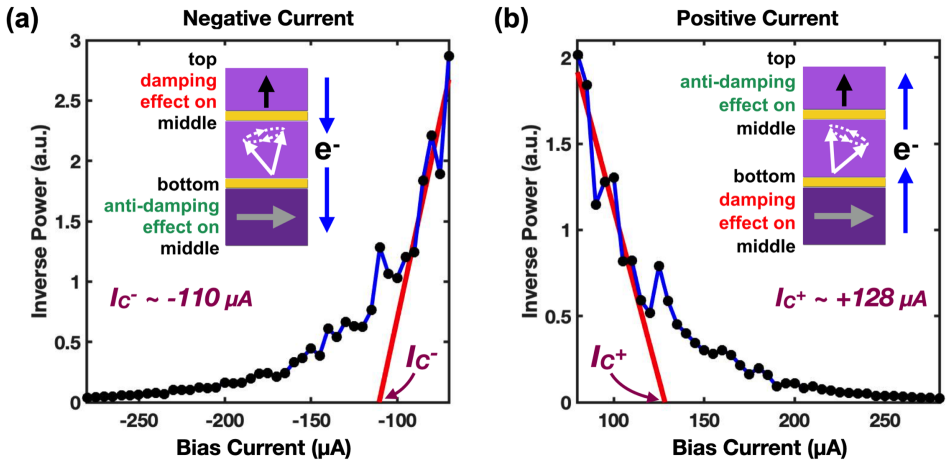

Figure 4.12: Critical current for different polarities and action of top and bottom layers on the middle. (a) Inverse power against negative bias current. Extrapolation of linear fit in subcritical regime estimates critical current to be about -110 μA. Inset illustrates individual roles of top and bottom layers on the middle for negative bias. (b) Same as (a) but for positive bias where critical current is estimated to be about +128 μA. As shown in inset, roles of top and bottom layers are now switched.

As observed in Fig. 4.5.a, emission parabola is slightly shifted towards positive current directions indicating a larger critical current for positive current than for negative current. Critical current for an STNO can formally be estimated by plotting inverse emission power against bias current [84] as shown in Fig. 4.12. Here critical currents are derived with a linear fit to inverse power plot against bias current in the subcritical regime. Estimated critical currents for positive and negative polarities are about +128 μA and -110 μA respectively. Critical current for $+I_{DC}$ is about 16% larger than that for $-I_{DC}$ which is consistent with the active polarizer assignment (insets of Fig. 4.12). For $+I_{DC}$ top layer creates anti-damping and is not expected to be as strong as the bottom layer which is a well-established polarizer. Therefore, $+I_{DC}$ would require a larger current to stabilize precessions compared to that for $-I_{DC}$.

4.3.5 Increase in power and the frequency redshift with current magnitude in both current directions

As explained in Fig. 4.8.a and b, for positive current direction, STT from the top tilts the precessing magnetization away from the vertical axis hence increasing the precessing cone-angle. This causes two effects. First as the cone angle increases and then the vertical component of the internal field is reduced hence causing the redshift. Same applies for the other current direction as well according to the study of T. Taniguchi et al. Apart from this, with a larger cone angle, the dynamical TMR will be greater hence the microwave power increases with the current magnitude in both directions. This further validates the derived picture.

4.3.6 Appearance of redshift and blueshift in emission at finite field

The explanation for this is well established in Fig. 4.7., considering OOP precessional modes in middle layer. Linear redshift and blueshift are explained with magnitude of internal field (B_{int}) of middle layer which is $\mu_0(H_k - M_S)m_z - B_z$ and $\mu_0(H_k - M_S)m_z + B_z$ for state-2 and state-1 respectively. Direct comparison between transition fields (from state-2 to state-1) confirms the discontinuity between redshift and blueshift is due to field induced switching (FIS).

4.4 Micromagnetic Simulations

To conclude the chapter, I present some example micromagnetic simulations conducted to present the nature of the OOP induced in perpendicular free layer due to an in-plane polarizer. Micromagnetic simulations were carried out using Mumax3 [85] which integrates the LLGS equation in the format defined as follows.

$$\overrightarrow{\tau}_{LL} = \frac{\gamma_{LL}}{1+\alpha^2}\left(\overrightarrow{m} \times \overrightarrow{B}_{eff} + \alpha\left(\overrightarrow{m} \times (\overrightarrow{m} \times B_{eff})\right)\right) + \overrightarrow{\tau}_{SL} \tag{4.6}$$

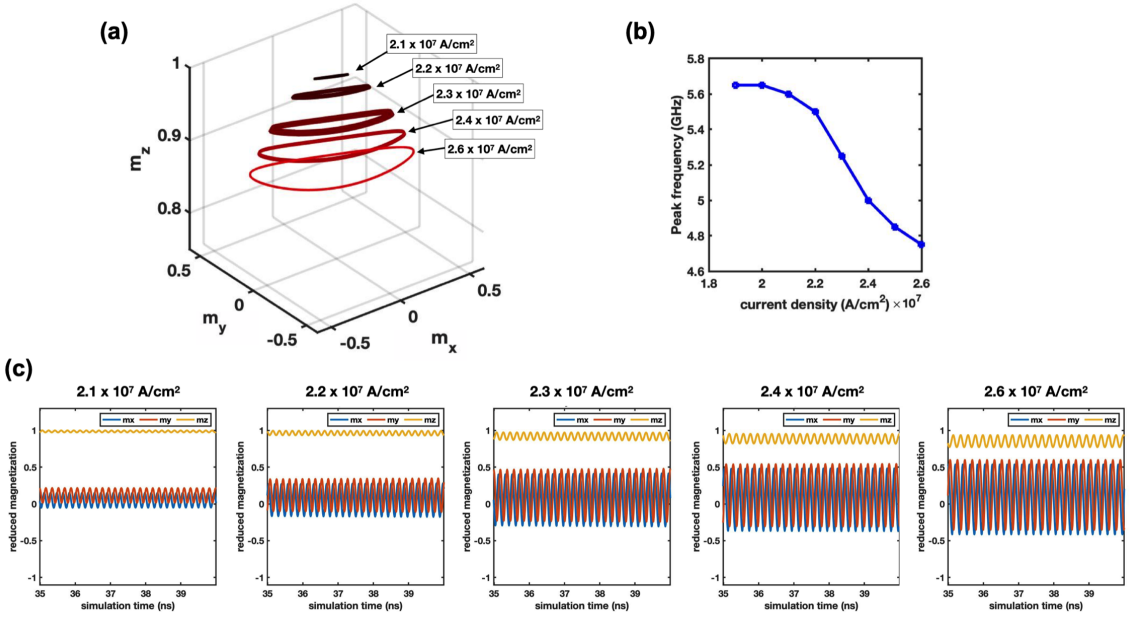

Figure 4.13: Example micromagnetic simulation conducted at zero external field. (a) OOP oscillation modes induced in a perpendicular free layer due to an in-plane fixed layer (polarizer). As the magnitude of the current is increased, out of plane oscillation cone expands. (b) Redshift of peak emission frequency with the current. (c) Components of the precessing magnetization in time domain for the current densities presented in (a).

$$\overrightarrow{\tau}_{SL} = \frac{j_z \hbar}{M_s e d}\left[\frac{\varepsilon - \alpha\varepsilon'}{1+\alpha^2}\left(\overrightarrow{m} \times (\overrightarrow{m}_p \times \overrightarrow{m})\right) - \frac{\varepsilon' - \alpha\varepsilon}{1+\alpha^2}\left(\overrightarrow{m} \times \overrightarrow{m}_p\right)\right] \tag{4.7}$$

$$\varepsilon = \frac{p\Lambda^2}{(\Lambda^2+1) + (\Lambda^2-1)\left(\overrightarrow{m} \cdot \overrightarrow{m}_p\right)} \tag{4.8}$$

Here m, m_p, B_{eff}, M_S, j_z, e and d are reduced free layer magnetization, unit vector along polarizer, effective magnetic field inside the free layer, saturation magnetization of the free layer, current density, electronic charge, and free layer thickness respectively. Furthermore, γ_{LL}, α, p, Λ, and $\epsilon^{'}$ are gyromagnetic ratio, damping parameter, polarization efficiency, Slonczewski Λ parameter and secondary spin-torque parameter respectively. Simulation is performed on a cylindrical free layer with 100 nm in diameter and 1.4 nm in thickness which

is discretized in to a mesh of 64×64×1. In Fig. 4.13, simulated dynamics induced in a perpendicular free layer (at zero external field) due to an in-plane fixed layer (polarizer) are presented with simulation parameters, 9.5 x 105 A/m, 2 x 10-11 J/m, 6.3 x 105 J/m^3, 0.02, 0.64, 0.8 and 0.1 for saturation magnetization, exchange constant, uniaxial anisotropy constant, damping parameter, lambda, polarization and secondary spin transfer torque term respectively. Fig. 4.13.a, presents OOP trajectories for select current densities where the enlarging of precession cone is seen with increase of current. Fig. 4.13.b, illustrates the frequency dependence of the bias current for the modes in Fig. 4.13.a, where the expected redshift is observed as present in Fig. 4.5.a. Origin for this redshift in the simulation done at zero temperature and at zero external field is the reduction of Bint due to reduction in m_z as cone angle is increased. Decrease of IPMA and M_S due to Joule heating can be another cause to enhance the inherit redshift.

CHAPTER 5

Topological Excitations in MTJs

Magnetic skyrmions are topologically distinct spin textures that can be realized under special conditions with broken inversion symmetry. The most pursued method of realizing this condition is with making use of Dzyaloshinskii-Moriya Interaction (DMI) [52, 53] where the ferromagnet (the free layer hosting spin textures) brought in contact with a heavy metal for example Pt. In a practical point of view, most of the first experiments were done regarding racetrack designs for computer memory applications where the skyrmions are transported back and forth with an applied current [55]. In the meantime numerical studies have been reported on utilizing skyrmions for logic gates [61] and neuromorphic computing [62]. The latter out of these two in fact is of great interest in the ongoing expedition towards brain inspired non-conventional computing in the face of ever increasing computational demands. On the other hand skyrmions created in magnetic tunnel junctions (MTJ) for memory application have also been computationally exploited pointing out its significant advantage in energy efficiency compared to more conventional utilization of parallel (P-state) and anti-parallel (AP-state) in MTJs [43]. Yet it has been challenging to realize these concepts experimentally due to the challenge in designing such an MTJ meeting the demanding conditions from a material engineering point of view.

Recently first evidence for skyrmion signature has been observed in a commercially available MTJ at cryogenic temperatures [10]. The MTJ used in this work lacked DMI due to the symmetric boundaries of the free layer used (MgO/CoFeB/MgO). However, there had already been evidence that requirements to stabilize a skyrmion can be met in confined geometries (for example, a ferromagnetic nano disk) without the aid of DMI [63, 64]. In this reported study, even in the absence of DMI, the required condition is shown to have met owing to the

spatially nonuniform stray field on the free layer from the pinning layer beneath the fixed (reference) layer. Strong evidence on creation and annihilation of a Bloch type skyrmion has been observed through DC and AC measurements which are then qualitatively backed with numerical simulations. In a different experimental study [9] demonstrating writing and deleting of magnetic skyrmions on to a thin ferromagnetic layer, stochastic effects have been observed where the free layer switching between ferromagnetic and skyrmionic states back and forth producing the well know random telegraph signal. In the meantime, recently an another experimental demonstration [86] has been reported where, the random probabilistic switching of an MTJ between its P and AP states are utilized to build an artificial neural network (ANN) which could successfully recognize images of numbers.

These findings encourage to further study the aforementioned skyrmionic signature created in an MTJ towards understanding their robustness and the time evolution. Interestingly both possible outcomes, first, strong robustness to thermal fluctuations and lattice defects and secondly, weak robustness leading to probabilistic switching between states are in great importance in the application world. High robustness is important for memory applications and probabilistic switching generating RTS is important for brain inspired computing. For the latter, control over the time averaged probability of the states is important as it has been used as the activation function in training the ANN of the aforementioned study. This has motivated us to first obtain skyrmionic signature in an MTJ and then move on to generate controlled RTS.

5.1 Device Structure and DC Characterization

The devices reported in this chapter are a property of Avalanche Technologies. These bilayer devices fall under the category of perpendicular co-linear devices where both free and fixed layer magnetizations are vertical and perpendicular to the plan at the base temperature of study which is 77 K. The devices are patterned into circular pillars with diameters ranging from 80 nm to 400 nm. The detailed device structure is shown in Fig. 5.1.a where the key layers are indicated with arrows representing their magnetization in single domain approxi-

mation. The top of those three is the free layer and is sandwiched between two MgO layers. Interfacial perpendicular magnetic anisotropy arising from the CoFeB/MgO layers creates a perpendicular easy-axis [40] allowing its magnetization at zero external field to be vertical. The coercivity field of this free layer is low enough that its magnetization can be manipulated by an external magnetic field less than 50 mT. The middle of the three layers is the fixed layer and it is pinned by a pinning layer locating below the former which is the third out of the aforementioned three layers. These middle and bottom layers are coupled via a thin (0.85 nm) Ru via RKKY coupling forming a synthetic anti-ferromagnet (SAF). Compared to this pinning for an in-plane magnetized layer, that for perpendicular layers is hard to achieve and exhibits poor robustness at room temperature. This is the main reason for having all the experiments under this chapter performed at cryogenic temperatures. That being said, the main layers required for understanding the functionality of this MTJ are the aforementioned top and middle layers which are referred to as free and fixed layers reflecting their roles in the device.

All the devices studied, with diameters ranging from 80 to 400 nm possess a square hysteresis loop under perpendicular magnetic field (B_z) at 77 K while the coercivity (half width of the MR_Z rectangular loop) decreases with increasing diameter. The temperature response of the MR_Z loops has also been studied and Fig. 5.1.b illustrates those for a device with a diameter of 250 nm under a bias of $I_{DC} = 10\ \mu A$. As seen, with the increase of temperature, coercivity field reduces narrowing the hysteresis loop. After 120 K, AP to P transition (as the field is swept right to left), has produced multiple steps in contrast to a single abrupt transition that was observed at lower temperatures. Those states with resistance values in between R_{AP} and R_P are hence referred to as intermediate resistance states or IRS. The signature of IRS depends on the temperature and for 120 K and 140 K they are only present in the AP to P transition where at 160 K, IRS starts to appear on P to AP transition (field swept from left to right) as well. Variation of coercivity field upon temperature can be fit to Kneller's law as shown in equation 5.1 and 5.2, where H_0 is the coercivity at $T = 0$ K and T_0 is the superparamagnetic blocking temperature of the free

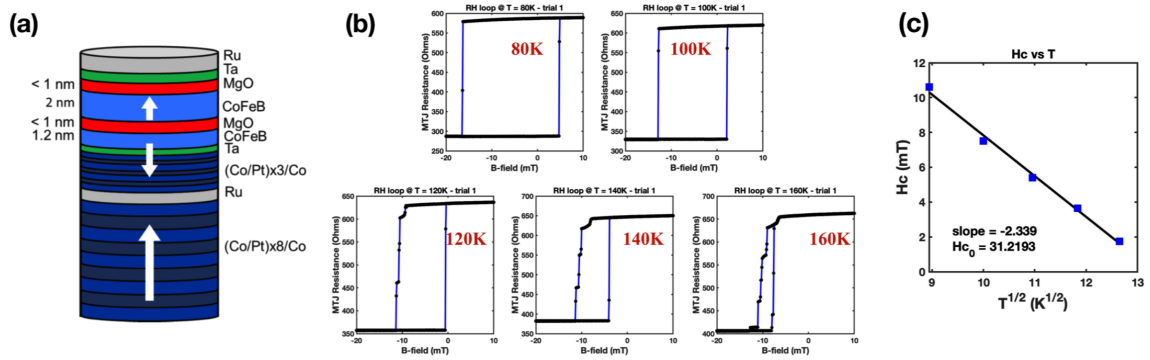

Figure 5.1: Device structure and MR_Z (z-axis magnetoresistance loop) at different temperatures (a) Device structure. The top most arrow indicates the net magnetization (in single domain approximation) of the top layer which is the free layer of this device. Micromagnetic structure of the free layer can be more complicated for example hosting skyrmions or multiple domains. The arrow bellow represents the magnetization of the fixed layer and below that is that of the pinning layer. The principle magnetizations required to understand the basic dynamics and excitations of the device are only those of the free and the fixed layers. (b) Perpendicular magnetoresistance loops (MR_Z) of the device at different temperatures for a device with diameter of 250 nm under a bias $I_{DC} = 10\ \mu A$. As seen, as the temperature increases, coercivity field reduces narrowing the hysteresis loop. After 120 K, AP to P transition (as the field is swept right to left) has produced multiple steps in contrast to a single abrupt transition. Those states with resistance values in between R_{AP} and R_P are hence referred to as intermediate resistance states (IRS). The signature of IRS depends on the temperature and for 120 K and 140 K they are only present in the AP to P transition where at 160 K onwards IRS starts to appear P to AP transition (field sweet from left to right) as well. (c) Temperature dependence of the coercivity field derived from the bottom section of MR_Z loops. The dependence has been fitted according to Kneller's law and H_0 in the extrapolation is the coercivity field at $T = 0$ K.

layer. The results of the fitting is shown in Fig. 5.1.c.

$$H_c(T) = H_0 \left[1 - \left(\frac{T}{T_0}\right)^{\frac{1}{2}}\right] \tag{5.1}$$

$$H_c(T) = -\left(\frac{H_0}{T_0^{\frac{1}{2}}}\right) T^{\frac{1}{2}} + H_0 \tag{5.2}$$

5.2 AC Characterization - Ferromagnetic Resonance

AC response of the device to an external applied microwave current has been studied where the microwave signal is injected to the MTJ via the AC terminal of a bias-tee as explained in chapter 3. This allows to simultaneously probe the DC voltage across the device allowing resistance measurement (with a bias usually about 10 μA) and FMR measurements through a lockin amplifier. This bias (DC background) current is optional and does not qualitatively affect the FMR modes as long as kept low (below 20 μA)) where the DC induced STT effects are not dominant.

The FMR results are obtained for both field sweep directions, AP to P and P to AP upon initializing the device to AP and P states respectively. This initialization is important as the range of the magnetic fields used in FMR measurements are not necessarily sufficient to initialize the device by themselves. Device is initialized to AP (P) state by applying a large positive (negative) field prior to an experiment. Fig. 5.2 presents the summary of results from a typical such FMR experiment carried under RF at -30 dBm and with 0 μA DC bias. The sensitivity and the input integration times used at the lockin amplifier are 200 V/pA and 300 ms respectively. The experiment is conducted at 77K (liquid nitrogen temperature) and all the following data presented under this chapter are obtained at this temperature unless otherwise specified. Fig. 5.2.a presents FMR results for field sweeping from the AP to P state where three Kittel-like [81] linear FMR modes can be seen up to about -6 mT after which qualitatively different modes start to appear. At -6.4 mT, the top two modes seem to have disturbed yet maintaining its Kittel-like linear behavior and are connected (without

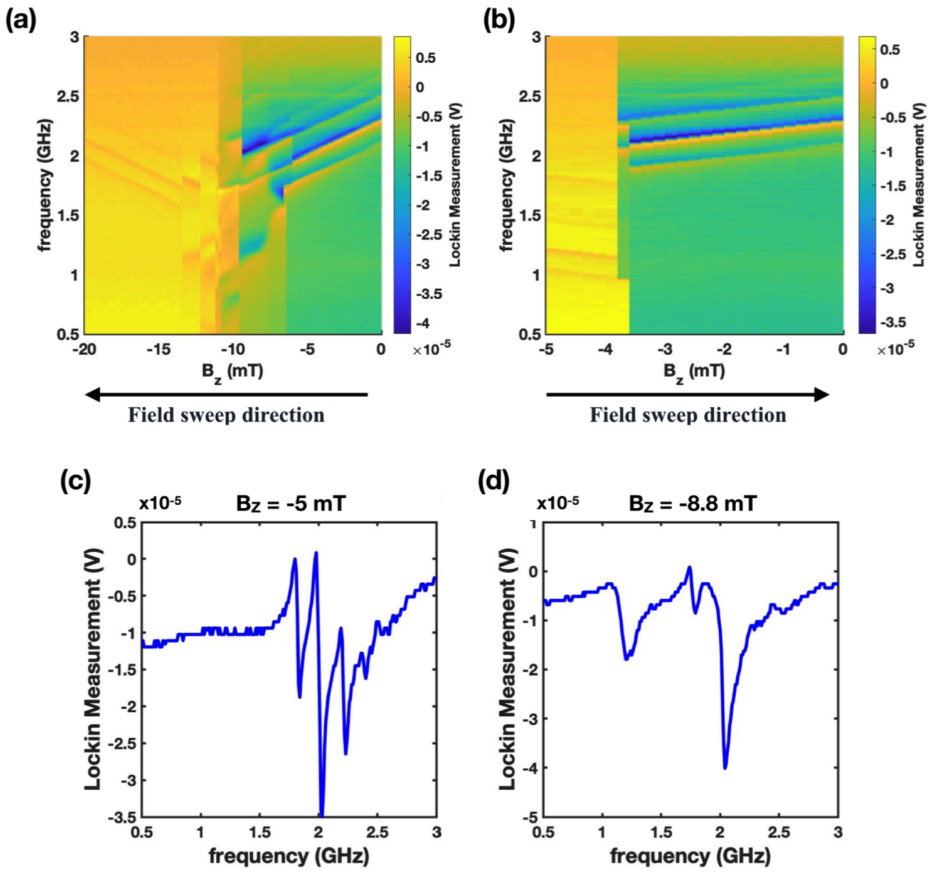

Figure 5.2: Ferromagnetic resonance (FMR) results under RF at -30 dBm for both field sweeping directions. The device was under 0 μA and at 77K and is initialized to AP (P) state prior to field swept towards left (right). (a) FMR results for field sweeping from the AP to P state. Kittel-like linear FMR modes can be seen up to about -6 mT after which qualitatively different modes appear up until about -14 mT. (b) FMR results for field sweeping from P to AP state. In contrast to what observed in (a) reasonably sharp transition of the Kittel-like linear FMR modes occur at the boundary of the P to AP transition, (c) Vertical trace of plot (a) at B_z = -5 mT where the device is about to transit from AP-state to the IRS region. Clear asymmetry of the modes can be seen which is a characteristic nature of spin transfer torque induced ferromagnetic resonance (STT-FMR) owing to the asymmetry of the field like torque. (d) Vertical trace of plot (a) at B_z = -8.8 mT. Three main modes are visible out of which two possess near symmetry which is a signature of skyrmion breathing modes.

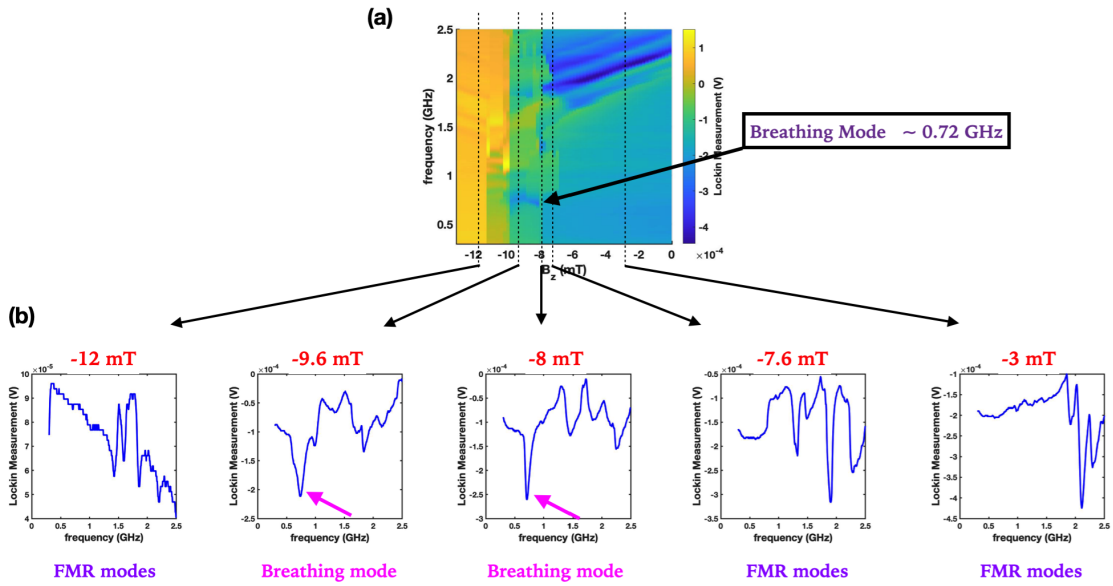

Figure 5.3: Detailed illustration of the breathing mode. Resonance spectrum for AP to P field sweep is obtained at an RF power level of -16 dBm and a DC background of 10 μA. (a) Resonance spectrum as the field is swept from AP to P direction with the device initialized to AP state. Linear spin wave modes are present down to about -7 mT at which those are disturbed. There is a major discontinuity of the spectrum at -8 mT where a prominent negative peak is observed at around 0.72 GHz which is identified as the breathing mode. As the field is further swept towards P state brething mode is eventually replaced by linear spinwave modes. (b) Resonance traces at select field values. Breathing mode at -8 and -9.6 mT is denoted.

any discontinuous abrupt jump) to their corresponding modes that prevailed prior to -6.4 mT. On the other hand, the bottom FMR mode first undergoes a discontinuous transition after which it is further qualitatively modified.

FMR signature at Kittle-like linear region and this modified (intermediate) region are qualitatively different. In Fig. 5.2.c., the trace at -5 mT exhibits three main asymmetric modes which is a signature characteristic of spin transfer torque induced ferromagnetic resonance (STT-FMR) owing to the asymmetry of the current induced field-like torque. In Fig. 5.2.d., the trace for -8.8 mT, there are mainly three modes, two (right and the left one) out of which possess more symmetry compared those in Fig. 5.2.c. In fact, though skyrmion breathing modes are not linear but have more complicated behavior, those modes are mostly symmetric compared to a STT-FMR mode [65]. This is an indirect yet strong supporting observation to suggest these modes are from skyrmion breathing. Another possibility for this state is a magnetic bubble (topologically distinct from a skyrmion). However fundamental resonance frequency of such a magnetic bubble is much larger than those for a skyrmion. In the meantime, in Fig. 5.2.d., it can be seen that the middle mode (between the two breathing like modes), though smaller in magnitude, possesses a STT-FMR like asymmetry. One of the ways to explain such a signature in the FMR plot is to consider coexistence of a domain and a skyrmion. Such domains and any lattice defects acting as skyrmion nucleation points are practically different from device to device making it almost impossible to reproduce identical results even for two devices with same parameters. In other words, FMR plots obtained for two devices having identical nominal parameters and under same experimental conditions, though qualitatively agree, will not match quantitatively. This makes extensive study of domain effects quite difficult. As field is further swept towards the P state, breathing mode like signature disappears recovering linear spin wave modes. In contrast to this feature rich resonance plot during AP to P field sweep, that obtained for P to AP field sweep does not possess such character as seen in Fig. 5.2.b. Only two groups of (each corresponding to P and AP states) linear spin wave modes are present with an abrupt transition indicating the field induced switching.

To further illustrate the breathing mode Fig. 5.3 is presented. In contranst to Fig. 5.2, this has been obtained under an RF power of -16 dBm and a DC background of 10 μA. This plot differs from Fig. 5.2 mainly due to the modified energy landscape due to different level of Joule heating occurring at -16 dBm. Fig. 5.3.a., presents the 2D resonance spectrum (during AP to P field sweep) in which a clear breathing mode is observed at 0.72 GHz. Fig. 5.3.b., present single resonance traces at select field values illustrating the breathing mode at -8 and -9.6 mT.

5.3 Microwave Induced Intermediate Resistance States

FMR results hold strong evidence that during AP to P transition apart from positive slope FMR lines converting to negative slope FMR lines, there exists an intermediate region where much more complicated signatures are present. Linear FMR modes seem to have vertically shifted but there exists one band containing a mode that has complex dependence on the field. This is of great interest as this closely resembles the skyrmion signature that has been predicted and experimentally observed before [10]. Motivated by this I moved on to observe the effect of RF input on the MR_Z loop and the preliminary results are present in the Fig. 5.4. In the FMR plot where the field is swept from AP to P, the tail end of the main FMR linear mode settles around 2 GHz before getting significantly modified. Motivated by this, the AP to P transition (half of the MR_Z loop) is studied under RF input with frequencies around 2 GHz and at different power levels with a bias current of 10 μA. Fig. 5.4.a presents such AP to P transitions for frequencies 1.8, 2.0 and, 2.2 GHz at a power level of -15 dBm. For all the frequency values at the power level used multiple events of IRS are observed while those for 2 GHz seem to be the most feature rich. Next, decreasing power further down for the same select three frequencies, it is observed that 2 GHz RF input is capable of creating IRS even down to -30 dBm (full data not shown), hence 2 GHz is chosen as the frequencies for following experiments where the RF input with fixed frequency is used. Fig. 5.4.b presents effect of RF at 2 GHz at four different power levels. Chaotic behavior can be seen as power is increased which is a consequence of excess Joule heat created. Fig. 5.4.c summarizes the

effect of power on the MR_Z width as derived from the bottom section of the MR_Z loop. Half width of a rectangular hysteresis loop is the coercivity field which is known to decrease with increase in temperature. This explains the decrease in hysteresis width with increase in power. The two different plots are shown for power units in 'dBm' and 'mW'. As already mentioned, the hysteresis width is derived from the lower part of the MR_Z loop as no IRS is formed during P to AP transition for the range of power levels used. I have repeated the experiment with RF power up to -5 dBm where IRS is present during P to AP transition as well with an overall significant distortion in the entire loop. This is assigned to the drastic increase of the device temperature due to the enormous Joule heating. This reason is backed by the observation that, when the temperature of the device is increased beyond 150 K, even with no RF, spontaneous IRS is formed during both transitions of the loop as seen in Fig. 5.1.b.

After this I moved on to perform a more comprehensive study on the AP to P transition under RF within a range of frequencies with small increments. The results are presented in Fig. 5.5. The procedure is, at each frequency, first, device is initialized to AP-state by applying a large $+B_z$ after which the field is swept towards the P-state while the frequency is held fixed. Therefore, each horizontal line of a presented 2D plot is basically an AP to P transition of an MR_Z loop. As usual, the voltage across the device is constantly monitored under a DC bias of 10 μA from which the resistance is calculated. In Fig. 5.5.a., five such AP to P MR_Z 2D plots are presented obtained under different RF power levels ranging from -40 to -20 dBm. At -40 dBm (lowest used in the entire study), no hints of IRS is present however, a triangular shaped feature can be seen located around 2 GHz which is a signature usually seen due to microwave assisted switching [87]. This is a point worth to be noted that even at such a low (-40 dBm) power level, where any Joule heating due to the RF signal is presumably negligible, RF still has an effect inducing microwave assisted switching signature which has originated near 2 GHz. Therefore, for the experiments following, 2 GHz has been used as the frequency to stimulate dynamics at the tail end of the AP-state. As the power is further increased IRS start to form and are embedded in the main triangle described before.

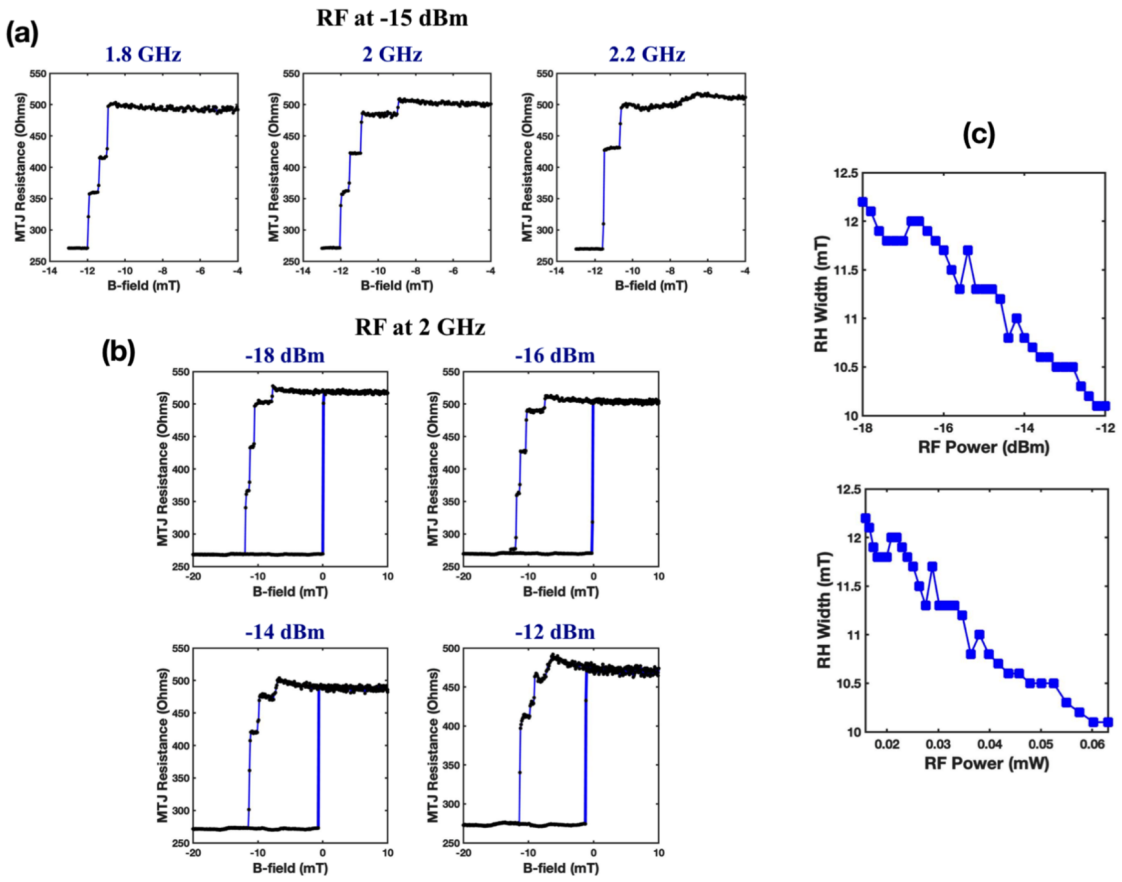

Figure 5.4: Microwave (RF) induced effects on MR_Z (half) loops with $I_{DC} = 10\ \mu A$. (a) AP to P transitions of MR_Z loop under RF input of -15 dBm at three different frequencies derived from the FMR results. The number of intermediate resistance states (IRS) that are induced has varied with the value of the frequency used. (b) Full MR_Z loops under RF input of 2 GHz at different power levels. As the power increased chaotic behavior can be observed probably originating from excess Joule heating. (c) Dependence of MR_Z loop width on RF power at 2 GHz where the width of MR_Z loop (RH width) is derived from the lower part of the MR_Z loop. The width decreases as a direct consequence of increase in the device temperature due to increasing Joule heating.

The plot is a direct measurement from a voltmeter alone yet, at higher power levels FMR lines are still visible and are aligned with the corresponding triangles further supporting the microwave assisted switching phenomenon. Fig. 5.5.b zooms in to the 2D plot obtained at -30 dBm which is a power high enough to induced multiple IRS yet not too high to distort the plot with excess Joule heating. As seen, apart from the AP and P states, three IRS are present that are embedded in to the main triangle. These three IRS process resistance of 360, 470 and 525 Ω respectively while the P and the AP states process 263 and 556 Ω respectively.

During these experiments, specially in obtaining repeated single AP to P half MR_Z loops, I noticed that the traces are not completely reproducible. They all would take a close path but the precise locations of the IRS events are seen to vary in a random fashion when the same experiment is repeated multiple times. This motivated me to think there are indeterministic stochastic effects going on and in fact, the IRS states created are not completely robust. With this motivation I moved on to explore the robustness in such modes by monitoring the stability of the state over time. The observations are presented in the following section.

5.4 Microwave Induced Random Telegraph Signal

The main procedure for the experiments following is to induce IRS using RF as explained in the previous section and then to monitor the device resistance over time. For this purpose, the DC line of the bias-tee (already connected to current source, Lock in amplifier and voltmeter) is connected to a network analyzer with 16-bit high precision digital amplifier. For these set of experiments, lock-in amplifier is not used however, it is left connected all the time as every time the measurement setup is modified taking instruments on an off I am risking the device to be compromised due to potential static electric discharges. Also in contrast to the AC line of the bias-tee, having additional instruments (lock-in in this case with an input impedance of 1 MΩ) connected to the DC line almost has no effect on the final readings. Preliminary tests were conducted using a low noise voltage amplifier, battery bank (as a stable reference for signal truncation) and an oscilloscope but the network analyzer

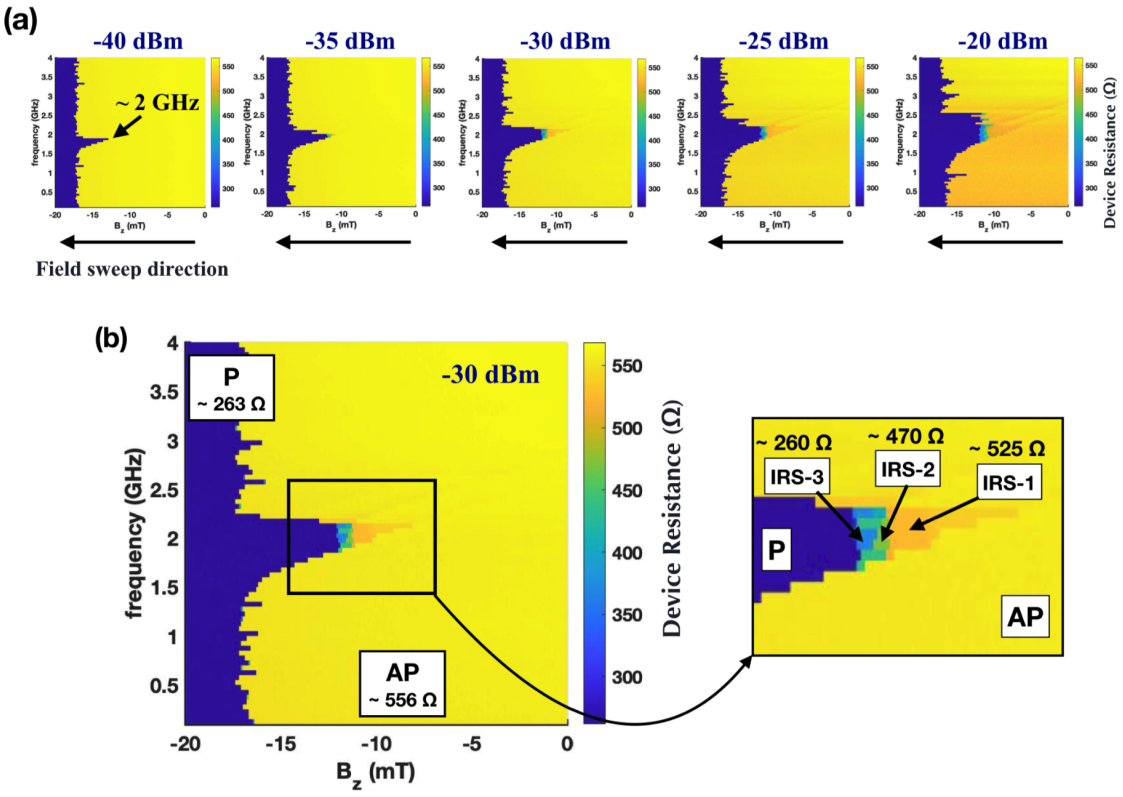

Figure 5.5: AP to P field sweep MR_Z curve (half loop) under RF with varying frequency under $I_{DC} = 10\ \mu A$. The device is first initialized AP-state with a large $+B_z$. The field is then swept towards P-state under RF with one set frequency at a time. Each horizontal trace is an independent AP to P half MR_Z loop for the particular frequency. (a) Five plots are presented obtained at different power levels. When the power is very low, only P (dark blue) and AP (bright yellow) states are present with a triangular shaped feature located near 2 GHz which resembles the microwave assisted switching. As the power is increased multiple IRS regions are induced adjacent to the aforementioned main triangle and even with these data obtained with the voltmeter, FMR lines are visible at high power levels and are aligned with hypotenuse of the triangles.

proved to produce better results and convenient to use.

IRS is produced using RF at different power levels while the frequency is mainly kept at 2 GHz. Then holding the field at the place of the onset of a select IRS event, while RF turned on, the voltage across the device is monitor for different time spans ranging from 30 ms to 40 s. As expected random transitions (switching back and forth) is observed in the device resistance between two resistance values sandwiching the select IRS event. This sharp stochastic back and forth transitions in such nature is well known as the random telegraph signal (RTS) sometimes also referred to as random telegraph noise (RTN). Having seen the evidence for RTS, its evolution is observed as the magnetic field is swept through the IRS event in very high field resolution (up to 20 μT while the Earth's magnetic field is around 50 μT). As expected, field acting as the control factor biasing the device's preference to stay in one of the either two states, has direct effect on the two state populations and the switching rate between the two. Preliminary results for such a collection of RTS traces (under 2 GHz at -16 dBm) with sweeping magnetic field (crossing through a select IRS event) are shown in Fig. 5.6.

The selected event to traverse across is the first transition to occur as the field is swept towards P from AP state where the device's resistance switches from AP-state resistance (509 Ω) and namely IRS-1 resistance (485 Ω). It is seen the AP-state resistance here is less than that observed in Fig. 5.5.b. This is due to the difference in Joule heating created at different RF power levels (hence the device being at two different temperatures), as has already been observed in Fig. 5.4.b. The collection of RTS traces recorded at the network analyzer are combined to form a 2D plot as presented in Fig. 5.6.a. The magnetic field on the device (initialized to AP-state) is swept through IRS-1 event and each vertical segment in the 2D plot represents the RTS recorded at the specific field. Fig. 5.6.b demonstrates select such individual RTS traces for a set of field values. As seen from the further right, device undergoing the process starting from the AP-state, as the field is swept towards the P-state, in contrast to the single transition captured in Fig. 5.4 at much lower field resolution (100 μT compared to 20 μT here), dwelling between the two states can be seen. At higher fields

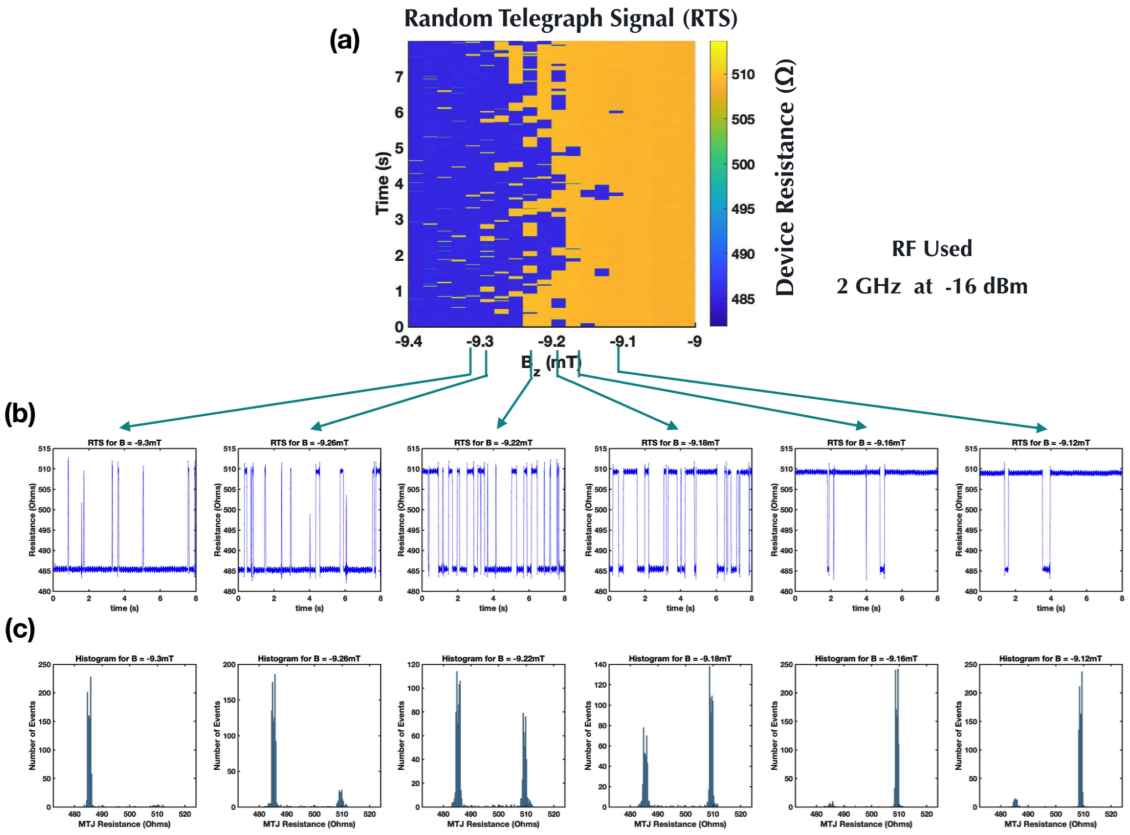

Figure 5.6: Random telegraph signal (RTS) observed under an RF input of 2 GHz at -16 dBm. (a) Color plot of the random telegraph signal. The field is applied in -z direction and swept from low magnitude to high magnitude, i.e., right to left in the plot. The device starts off being in the AP (high resistance) state and as the field is swept stochastic effects are observed with dwelling (switching) between AP and P states. As the field is further swept, the device would spend more time in the P-state than in the AP and eventually settling in to the P-state. (b) Individual traces of the random telegraph signal for select magnetic fields. Each plot corresponds to a vertical line in the color plot as indicated by the arrows. (c) Histogram count for each resistance state at the magnetic fields chosen for (b). The right bin represents the AP-state while the left bin represents the P-state. The population of states can clearly be seen to move from right to left as the magnetic field is swept.

(magnitude wise) for example -9.12 mT, the device prefers to remain in the AP-state than in IRS-1. As the field is further swept this preference gets adjusted that at higher fields for example -9.26 mT the device's preference is to remain in IRS-1 than on AP-state. Fig. 5.6.c presents the histogram counts (population) of the two events for each field value further demonstrating aforementioned observation. Apart from that the switching rate (attempting frequency) between the states vary with the field and attains a maximum around the point where the population is divided half and half between the two states. This is in consistent with probabilistic events in a sample (for example, nuclear decay) where the rate of the events is directly proportional to the number of active states present. In this case, since the probabilistic switching is recurring between two states, the switching rate (frequency) is directly proportional to the product of the two populations in each states, i.e., $f = Ax(1-x)$ where x is the normalized population of one state (say AP) and $(1-x)$ is that for the other state (say P) while A is the proportionality constant. This function (being an inverted parabola) attains its maximum at $x = 0.5$.

Having observed RTS at -16 dBm (2 GHz), I moved on to explore its dependence with RF power. Fig. 5.7. provides a summary of the main observations made. The top panel of Fig. 5.7.a presents the RTS recorded at -16.2, -16 and -15.8 dBm while the middle and the bottom panels present the probability of each state (blue is IRS-1 and red is AP- state) and the switching frequency respectively. The curve of switching rate is fitted with a Gaussian to extract the parameters. As expected, it can be seen that the maximum frequency has occurred around the point where both states are equally populated having 0.5 of probability each. The fitting quality is moderate for lower switching rates but gets better as the frequency increases. The evolution of the RTS for 2 GHz is studied for a vast range of RF power levels and Fig. 5.7.b, (top and bottom plots, frequency plot against power in dBm and mW respectively) demonstrates varying of the maximum frequency with RF power. The most significant observation we have made here is the ultra sensitivity of RTS frequency upon RF stimulation where even within a small increment of power (from -16.5 to -15 dBm) the maximum frequency has changed by almost two orders of magnitude.

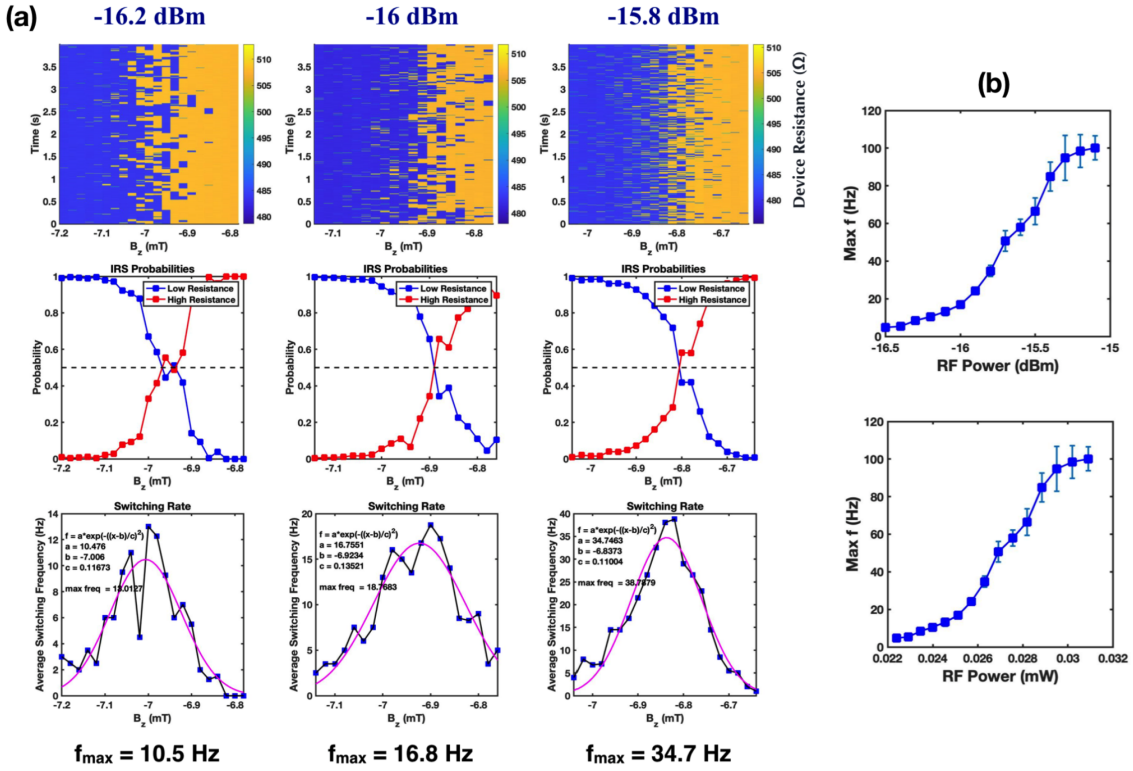

Figure 5.7: Random Telegraph Signal (RTS) frequency dependence with power level at 2 GHz. (a) Random Telegraph Signal for power levels -16.2, -16 and, -15.8 dBm. The top row presents the color plots. The second row plots demonstrate the probability for each state (AP or P) as the magnetic field is swept where the red (blue) represents the AP (P) state. The third row is the switching rate (frequency) plot with the magnetic field where the rate is calculated by a computer algorithm. Pink curve is the Gaussian fitting to the points from which the parameters and their relevant uncertainties are obtained. The maximum switching frequency is achieved at the field where each AP and P states have 0.5 of probability. This point is usually referred to as the detuning point. (b) Maximum switching rate of the random telegraph signal at different power levels representing both in dBm and mW. Maximum frequencies along with their uncertainties are derived from the Gaussian fitting results.

5.5 Discussion

As presented in the preceding sections, RTS is observed between AP-state and IRS-1 when the AP initialized device undergoes a magnetic field sweep crossing the AP to IRS-1 transition. Similar RTS has been observed between different IRS as well but main focus is given to that produced between AP state and IRS-1. Fig. 5.9.a and b., side by side compare two states in the RTS plot to the full MR_Z loop both obtained under the same experimental conditions (in two independent runs). It can be seen that the yellow (blue) state of the RTS plot is practically identical to the AP (IRS-1) state in the MR_Z loop. This comparison has been done to confirm the relevance of the RTS states in the context of the MR_Z loop. In fact, initial tests on MR_Z loops obtained under fast acquisition and no averaging at the voltmeter had hints of such stochastic switching which was one of the main motivations (besides the lack of exact reproducibility of IRS trajectories) to look into the presence of RTS.

First of the main two questions is to identify the potential candidate to represent this IRS. IRS is caused as a result of partial compensation of volume averaged m_z that changes TMR of the MTJ. Such IRS-1 involved in the RTS can be a skyrmionic state, bubble state, multiple domains which are qualitatively shown in Fig. 5.9.c., out of which a bubble state is a less probable as the fundamental resonance frequency of a bubble is much higher than that for a skyrmion. On the other hand this IRS-1 could in fact be a coexistence of a skyrmion and a small domain originating from a defect as hinted by the coexistence of near symmetric breathing-like modes and a small anti-symmetric Kittel-like mode in the FMR plot at -8.8 mT (Fig. 5.2.b). The possibilities (size, location etc.) of such defects could qualitatively alter the FMR spectrum. This makes it quite challenging to reproduce such experimental observations via a micromagnetic simulation where virtually an infinite number of possibilities for defects are possible. Sample micromagnetic simulations are carried out in collaboration with N. E. Penthorn that has identified Bloch type skyrmions to create such experimentally observed IRS. Results are presented in Fig. 5.8 where insets illustrate the micromagnetic configuration of the free layer at different IRS in the sample half MR_Z loop (i.e., AP to P transition). Magnetic disorder interms of grains (of size 30 nm) has

been incorporated to induce IRS. White (black) region of the inset corresponds to the region where m_z is positive (negative). Difference between the sizes of white and black region is directly proportional to the resildual m_z that reflects resistance value of IRS.

In the context of residual m_z at different IRS, transitions can be identified as device's attempt to minimize its energy during the magnetic field sweep. The instantaneous resistance of a bilayer MTJ in terms of its resistance values at AP and P states and the free layer magnetization angle (under single domain approximation) with respect to the fixed layer is given by the following equation and can be rearranged as shown.

$$R_{\theta}^{-1} = \frac{R_P^{-1} + R_{AP}^{-1}}{2} + \frac{R_P^{-1} - R_{AP}^{-1}}{2} cos\,(\theta) \tag{5.3}$$

$$R_{\langle m_z \rangle}^{-1} = \frac{R_P^{-1} + R_{AP}^{-1}}{2} + \frac{R_P^{-1} - R_{AP}^{-1}}{2} \langle m_z \rangle \tag{5.4}$$

$$\langle m_z \rangle = \frac{R_{\langle m_z \rangle}^{-1} - \left(\frac{R_P^{-1} + R_{AP}^{-1}}{2} \right)}{\left(\frac{R_P^{-1} - R_{AP}^{-1}}{2} \right)} \tag{5.5}$$

where $\langle m_z \rangle$ is the net (volume averaged) vertical component of the reduced (normalized) magnetization. This allows the estimation of $\langle m_z \rangle$ at different locations on the MR_Z plot. In the meantime, the free layer is dipole coupled to the effective local field (from external sources) namely from the stray field of the pinning layer and the externally applied field by the electromagnet. Energy arising from such a dipole coupling takes the form,

$$U_{dipole} \sim - \langle m_z \rangle B_{z,eff} \tag{5.6}$$

where $B_{z,eff}$ is the vertical component of the effective field at the free layer. Under this single domain approximation net dipole energy of the free layer can be estimated in arbitrary units for qualitative purposes. Fig. 5.10.a and b present the estimations for the $\langle m_z \rangle$ and U_{dipole} respectively in the context of the AP to P MR_Z curve. In Fig. 5.10.c., a zoomed in version of the estimated dipole energy in the context of the AP to P MR_Z

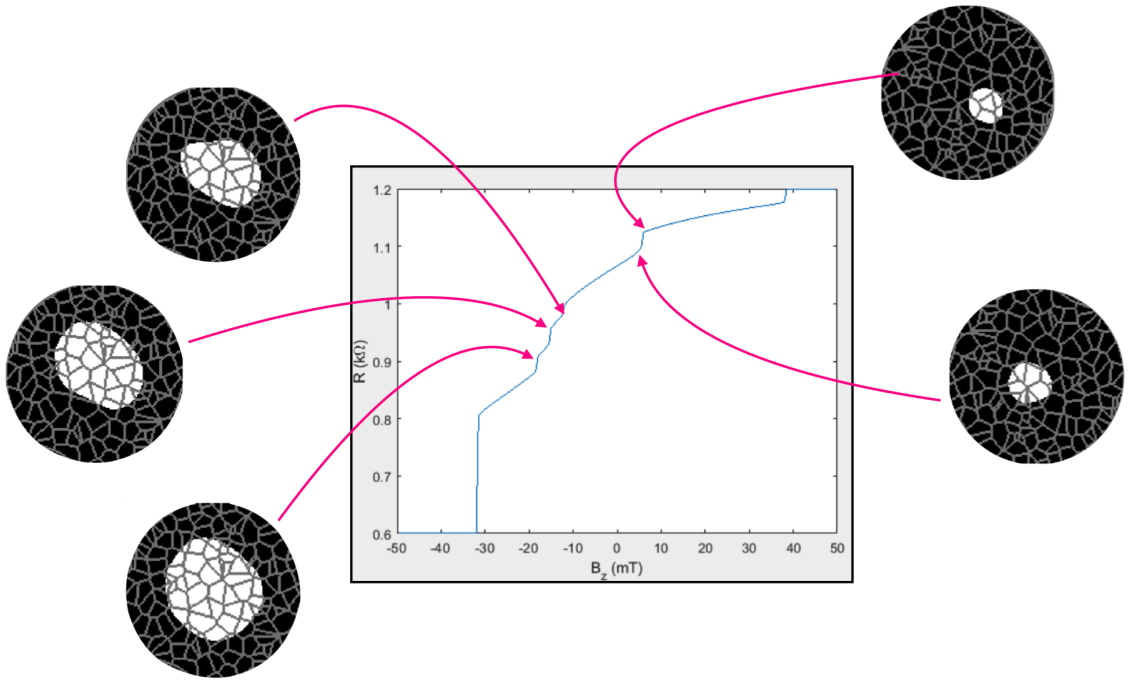

Figure 5.8: Micromagetic simulations corresponding to different IRS occurring in a sample MR_Z loop generated in simulation. Grains with size 30 nm are considered to generate IRS. Insets present snapshots of the free layer micromagnetic configuration during simulation where skyrmionic signature is observed. White (black) region corresponds to where the m_z is positive (negative). Modification of the size of the white region has caused IRS. (in collaboration with N. E. Penthorn)

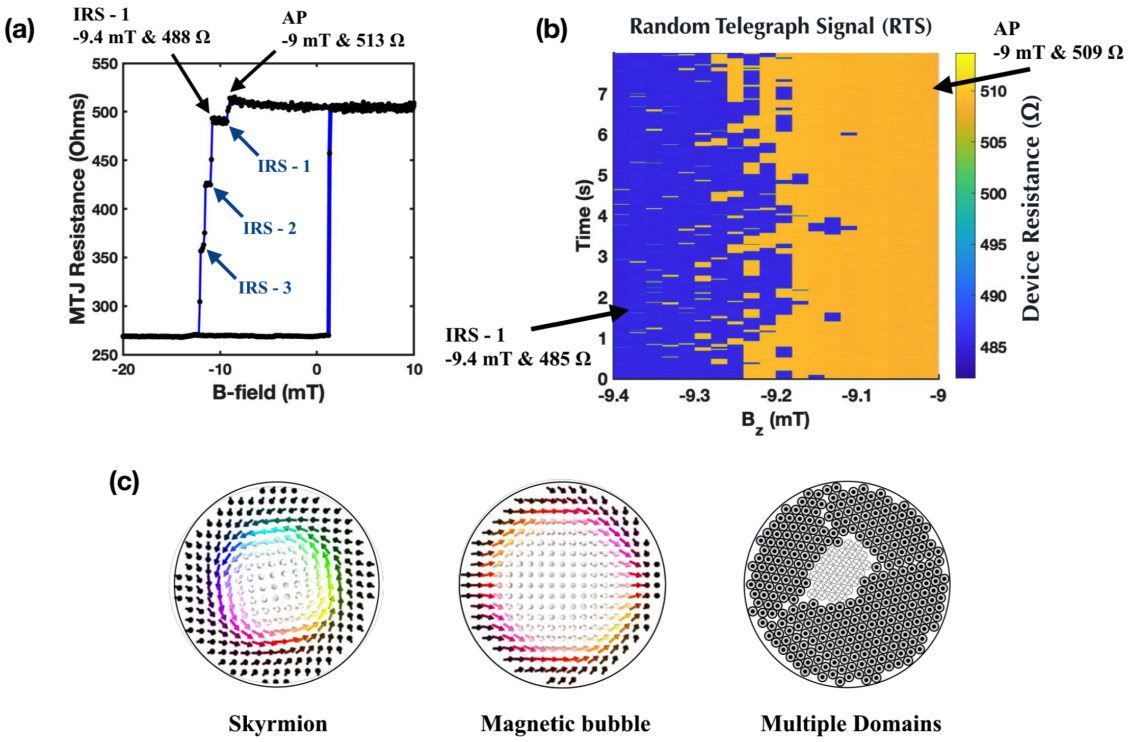

Figure 5.9: Random telegraph signal (RTS) in the context of the MR_Z loop both under RF of 2 GHz and at -16 dBm. (a) Full MR_Z loop producing there intermediate resistance states (IRS) as a result of the injected RF. To compare with the RTS plot, tail ends of the AP-state and the IRS-1 are read to be at -9 and -9.4 mT producing a resistance of 513 Ω and 488 Ω respectively. (b) Random telegraph signal plot for magnetic field sweep from right to left (AP to P). The bright yellow resistance at -9 mT is read to be 509 Ω while the bright blue resistance at -9.4 mT is read to be 485 Ω which are in good agreement with the values read from the MR_Z loop. (c) Possible candidates to represent IRS-1 state, namely, skyrmionic (bloch-type) state, magnetic bubble state and, ferromagnetic multiple domain state. Here the skyrmionic state is topologically distinct from the other two. In this device the fixed layer is pointing along the negative z direction as the P(parallel)-state is realized at a more negative field than the that for the AP(anti-parallel) state. In this picture, P (AP) - state is when the magnetic moments of the free layer are completely pointing in the negative (positive) z direction. For IRS events the net normalized vertical component of the magnetization, i.e $\langle m_z \rangle$ lies between -1 and +1 which can be realized in either form of shown skyrmion, bubble or multiple domains.

curve is presented for better visualization where U_{dipole} presented in arbitrary units and is offset and scaled for clear comparison. As pointed out with the vertical arrows, out of the four transitions, (namely, AP to IRS-1, IRS-1 to IRS-2, IRS-2 to IRS-3 and IRS-3 to P) the onset of first three transitions correspond to local maxima in the U_{dipole} curve. This is an indication that the device is undergoing such transitions in attempting to minimize its energy. However, at the onset of the fourth transition no clear local maximum can be seen. In fact the final total energy should also include anisotropy energy and demagnetization energy which is not considered for the current qualitative analysis. For such a detailed energy landscape micromagnetic spin structure of the free layer may be considered which will potentially explain all the four transitions seen in the plot.

Remaining of the main two questions is to answer the ultra sensitivity of RTS frequency upon stimulating RF power. As seen in Fig. 5.7.b., there is a significant correlation between RTS frequency and RF power. The maximum switching rate present in RTS plot where the populations between the two states are equal (also referred to as detuning point) has been increased almost by two orders of magnitude during an increase in power level as small as 1.5 dBm. Given this, it is worth while to consider the ultimate role played by this microwave signal on the free layer and on the formation of IRS. Mainly, this RF input can have two major influences on the magnetization of the free layer. First is the resonance effects while the other is Joule heating. This resonance effect is evident from the first panel of Fig. 5.5.a where microwave assisted switching [87] signature is observed even at a power level as low as -40 dBm where Joule heating effects are assumed to be negligible compared to that at power levels (above -20 dBm) used for RTS experiments. On the other hand, MR_Z loops are obtained with RF input at 100 MHz with power varying up to as high as -5 dBm. Here 100 MHz is chosen because it is well away from any resonance modes observed in the FMR plots so the only effect from such RF can assumed to be Joule heating. These two different contributions from the RF input on the free layer is demonstrated in Fig. 5.11. As seen in Fig. 5.11.c., as the power approaches -10 dBm, significant distortion on the otherwise perfect rectangular loop is present even with a thermally induced IRS as seen in Fig. 5.1.c. Even at

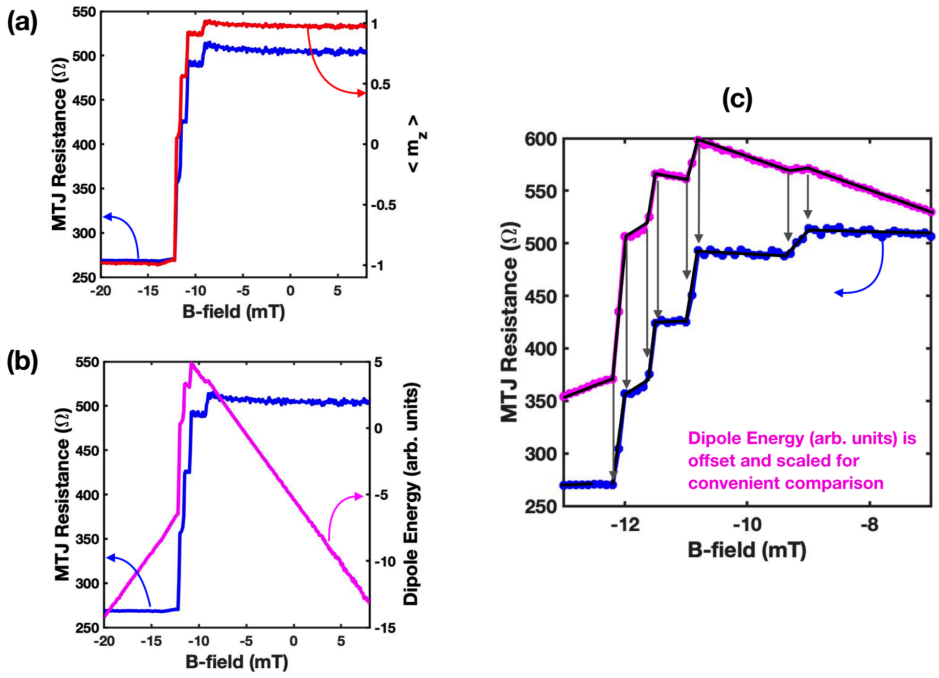

Figure 5.10: Qualitative comparison of reduced z-component of the free layer magnetization and dipole coupling energy with the local effective field (in arbitrary units) in the context of IRS events. (a) AP to P MR_Z half loop (blue) with the corresponding volume averaged normalized z- component of the free layer magnetization (red). (b) AP to P MR_Z half loop (blue) with the dipole coupling energy of free layer with the local effective field (pink) in arbitrary units. It can be seen that the lowest energy gap is between the AP and the IRS-1 while that between IRS-2 and IRS-3 being the highest. (c) Zoomed in version of (b) for clarity. The dipole energy curve (pink) has been scaled and offset for convenience of comparison.

around -15 dBm (around which the RTS experiments were performed) thermal distortions are apparent suggesting significant Joule heating.

Before considering the RF effects, I continue to eliminate the possibility that the ultra sensitivity observed is solely due to thermal effects. To proceed, I first estimate the effective device temperatures at -15 and -16.5 dBm as follows. From Fig. 5.4.c., the coercivity fields of the device under an RF stimulation of 2 GHz at -15 and -16.5 dBm can be read which are then converted into effective temperatures with aid of Fig. 5.1.c. and are found to be 120 K and 116 K respectively. RTS is a thermal process that causes switching between two potential wells seperated by an energy barrier. Frequency of this thermal process can be modeled according to

$$f \propto \exp\left(-\frac{E_b}{kT}\right) \tag{5.7}$$

where f, k, T and E_b are RTS frequency, Boltzmann constant, absolute temperature and aforementioned energy barrier respectively. This equation written for two different temperatures can be rearranged to find E_b as follows.

$$\frac{f_1}{f_2} = \frac{\exp\left(-\frac{E_b}{kT_1}\right)}{\exp\left(-\frac{E_b}{kT_2}\right)} \tag{5.8}$$

$$E_b = \frac{k \ln\left(\frac{f_2}{f_1}\right)}{\left(\frac{1}{T_1} - \frac{1}{T_2}\right)} \tag{5.9}$$

Substitution of 116 K (corresponding to -16.5 dBm) and 120 K (corresponding to -15 dBm) along with corresponding RTS frequencies of 5 Hz and 100 Hz suggests an E_b of 10400 K which is unrealistic. This holds strong evidence for presence of some other factor significantly assisting this boost of RTS frequency and is identified to be the resonance effects of the RF stimulant. It is again emphasized that (in relenvance to Fig. 5.3.a), 2 GHz used for the RTS experiments is the tailend of the first FMR mode just before the transition from AP state to IRS-1 featuring qualitatively different modes in the resonance spectrum. H. Suto et al 2015 [87] has shown that an MTJ under microwave stimulant with frequency

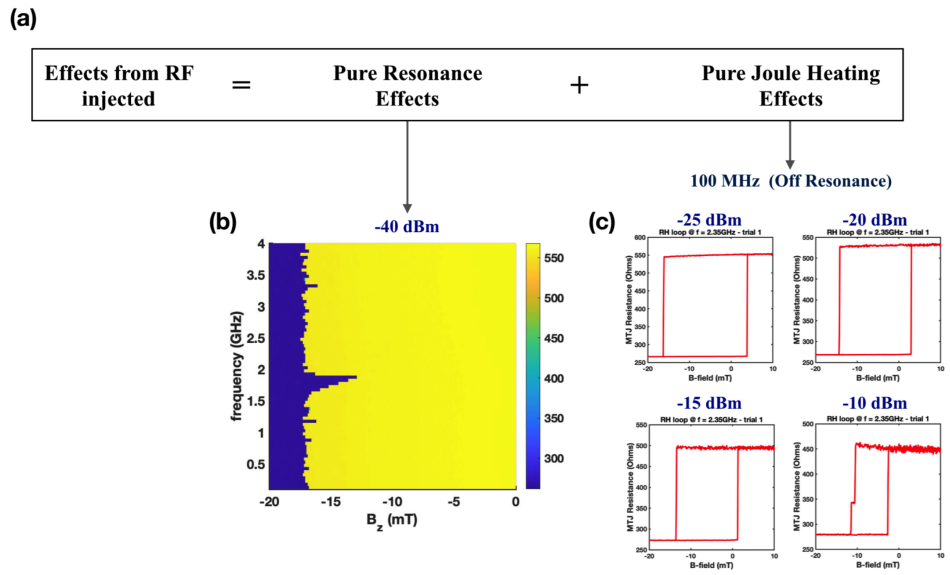

Figure 5.11: Effect of the RF input on the free layer. (a) Net effect of the RF input on the free layer can be understood as a combination of pure resonance effects and pure Joule heating effects. The evidence for each effect can be isolated by using either a very low power level or a frequency at far away from any resonance modes appearing in the FMR plot. (b) Half MR_Z (AP to P sweep) 2D plot with varying frequency with RF held at -40 dBm. Compared to the power levels used for RTS experiments (above -20 dBm), -40 dBm is quite low and any Joule heating produced by such a RF input can be considered negligible. Still a triangular shape can be seen located near 2 GHz which is a clear indication of well studied microwave assisted switching. This is evidence that, even without Joule heating effects, RF still can affect the dynamics of the free layer via resonance effects. (c) MR_Z loops obtained under an RF input of 100 MHz at different power levels. From the FMR plot it can be seen that none of the modes are present around 100 MHz confirming it is far from any resonance, i.e off resonance. For power levels below -15 dBm, the loop preserves its rectangular shape but shows clear variation of the AP resistance and the coercivity field (half width of the rectangle) which are direct consequences of increase in device temperature. At -10 dBm, in addition to the aforementioned variations, a single IRS has been formed while the AP to P transition. This is also a result of increase in device temperature.

matching one of its FMR modes can trigger the switching of the device at a noticeably lower field than otherwise which they called “microwave assisted switching”. Their key finding are summarized in Fig. 5.12.a. AP to P transition obtained for my device under RF stimulant at a power level as low as -40 dBm carries clear indication of such microwave assisted switching as again illustrated in Fig. 5.12.b. At -40 dBm, any Joule heating effects can reasonably be neglected at least compared to that occurring at around -16 dBm where the presented RTS has been studied. This microwave assisted switching has occurred at 2 GHz which is the tailend of the device’s first FMR mode as mentioned above confirming the findings of H. Suto et al 2015. In their work they have claimed that the triggering of microwave assisted switching is caused due to two main reasons. First, microwave stimulant (matching a resonance mode) facilitates pre-switching oscillations but more importantly it lowers the energy barrier between the two states in between which switching takes place. From equation 5.7 it is seen that RTS frequency is exponentially sensitive to the energy barrier separating the states. Therefore even a minor suppression of this energy barrier as suggested by H. Suto et al 2015 can significantly boost RTS frequency explaining the observations presented in this chapter which cannot be explained by thermal effects alone.

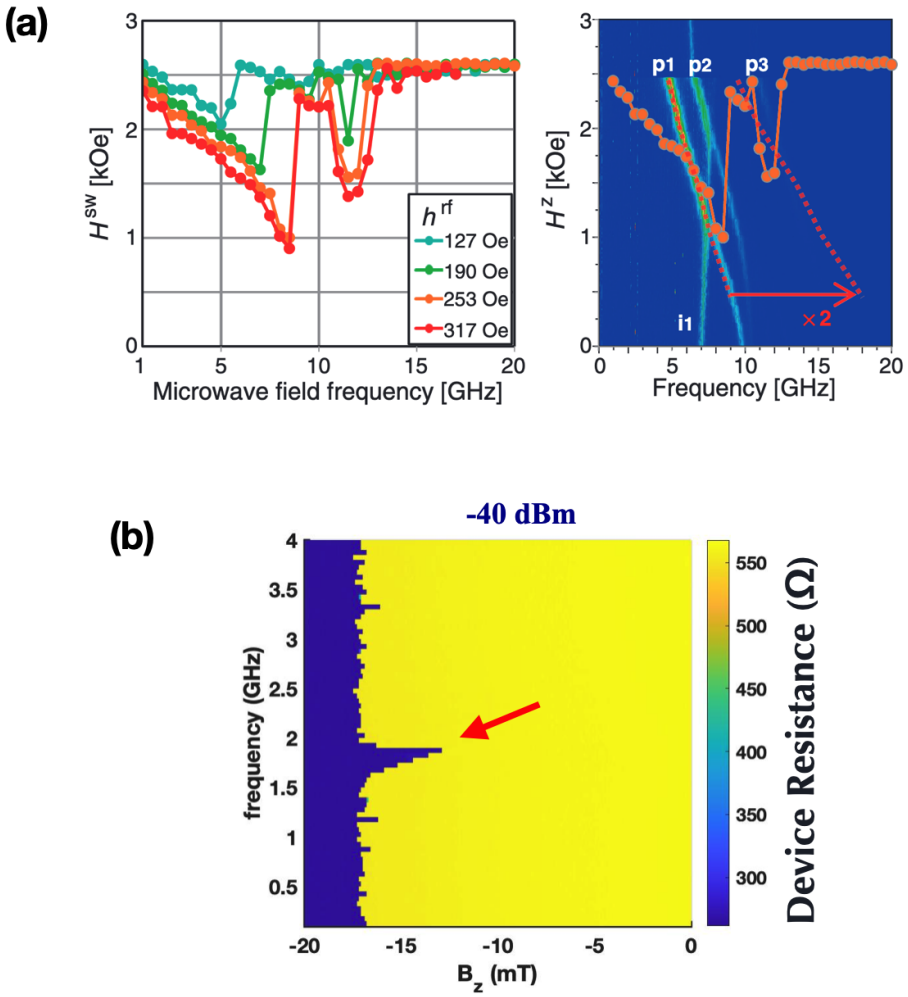

Figure 5.12: Significance of microwave assisted switching. (a) (after H. Suto et al 2015 [87]). Onset of microwave assisted switching that coincides with FMR mode. (b) Microwave assisted switching observed for the device presented in this chapter. Clear microwave assisted signature can be seen even at a power level as low as -40 dBm where Joule heating can reasonably be neglected.

CHAPTER 6

Conclusions and Future Directions

In this chapter I will conclude the finding of the two projects presented in this thesis followed by a brief outlook in which I will discuss how these two projects can be extended along timely interest of the research community.

6.1 Conclusion

6.1.1 Microwave Emission of a Tri-Layer MTJ at Zero Bias-Field

The first project presented here is a demonstration of an STNO that offers microwave emission without need of any external bias magnetic field. The tri-layer structure studied has shown promising potential offering emission up to 6 GHz that is the highest frequency achieved at zero bias field to the best of our knowledge. Usually a bias field is required for in-plane structures to tilt the free layer magnetization away from that of fixed layer so that it will experience a finite STT [25, 26]. After perpendicular spin valves were invented [39, 66] it was shown that bias-field free STNOs can be realized when free layer and fixed layer magnetizations are mutually orthogonal [17]. However with low GMR ratio these spin valves suffered low out put power therefore for real world applications zero-field STNOs made out of MTJs were required. After the S. Ikeda et al. 2010 [40] reported the first successful perpendicular MTJ offering low critical current, high thermal stability (for memory purposes) and high TMR ration simultaneously it became possible and efforts for realizing a better STNO were started again.

However, producing a reasonable high frequency in the absence of any bias-field had still

been challenging. Frequency of precessions in the free layer being directly proportional to the local field therefore, the strategy to increase emission frequency is to enhance the internal field. For perpendicular free layers, this is to enhance the IPMA field. The way to improve IPMA of MgO based MTJs is to reduce the free layer thickness [40]. However, doing so IPMA does saturate below a certain critical thickness and moreover at such low thickness limit interface defects could do more damage for overall device performance. Device reported in this thesis, this issue has been overcome by having two such MgO/CoFeB interfaces additively contributing to the final IPMA value. We studied devices with varying free layer thicknesses ranging from 1.35 nm to 1.5 nm and have found the optimal thickness for highest emission frequency to be about 1.42 nm. Theoretically, as the free layer thickness is reduced, IPMA saturates to a steady value [40] which means the emission frequency should also remain at the high value it attained. However, in contrast we observed a reduction in emission frequency as the thickness is reduced bellow 1.42 nm down to 1.35 nm which is possibly because interface defects starting to dominate at this low thickness limit harming device's overall performance.

In addition to high emission frequency offered, the other key characteristic we observe in this tri-layer device is its capability to produce emission in both current directions. Direction of STT depends on the current polarity through the free layer therefore usually sustainable oscillations are possible for only one current direction where STT counteracts the intrinsic damping while for the other current direction, STT being in parallel to damping will enhance it leaving no room for persisting oscillations [25, 26]. We explain this special capability of our device using spin dynamics involving dual polarizer action on the precessing middle layer. Even though the device has three layers among which only one (bottom) layer is fixed, we started with the open possibility to figure out which layer is producing the observed microwave emission. We eliminated the possibility where recorded microwave being produced by the top layer as it lacks an appropriate monitoring layer to cause sufficient dynamical TMR during precessions even if any. This leaves the scenario where middle layer being responsible for the recorded microwave output which has been explained by induction of

out-of-plane precessions that can successfully be recorded by an in-plane neighboring layer, in this case, the bottom. The evolution of the microwave emission upon an applied external field has provided strong evidence for these suggested out-of-plane oscillations. Once the middle layer is assigned the role of the precessional layer, we continued to fit dual polarizer action for the tri-layer device arguing that top and bottom layer to act as the effecting polarizer per each current direction enabling the bidirectional emission. Slight asymmetry around zero current in the emission spectrum holds evidence for this bidirectional emission where slight difference in critical currents for onset of oscillations are consistent with the expected relative strengths of top and bottom layers performing as polarizers.

6.1.2 RTS and Skyrmion Signature in a Perpendicular MTJ

Second reported project in this thesis is the observation of skyrmionic signature in a commercially available perpendicular MTJ at cryogenic temperatures where RTS was observed during induction of skyrmionic state under a microwave stimulant. In a recent report [10] on the same device structure conducted at 4 K, formation of skyrmion signature is shown with simultaneous monitoring of magnetoresistance and microwave resonance where skyrmion breathing mode like features were present in direct coexistence with intermediate resistance states (IRS) in the magnetoresistance curve. In the work reported in this thesis, we have extended this study to higher temperatures (77 - 200 K) where we observed spontaneous induction of IRS in the magnetoresistance loop (without aid of any RF stimulant) where stochastic effects were present producing a random telegraph signal (RTS).

MTJ devices studied were circular in geometry with diameters ranging from 80 to 400 nm and as the device size was increased, the tendency to form spontaneous IRS (in the absence of an RF stimulant) was found to be greater. That is, devices with 300 nm in diameter and above produced such spontaneous IRS at 77 K while devices with diameters smaller than 200 nm did not. 250 nm size was on the boundary where some devices showed this feature but some did not. For our study, 77 K was the base temperature used (with use of liquid nitrogen) therefore, devices offering a reproducible perfect square magnetoresistance loop

at 77 K were used. This is because, the square magnetoresistive loop at base temperature would be the control experiment with what the formation of IRS under other conditions will be compared. Most of the data taken are of devices with diameters ranging from 150 to 250 nm. Devices smaller than 150 nm were not used as they required higher magnetic fields to switch and the maximum persistence field offered by our homemade electromagnet is about 50 mT.

Devices that offered a perfect square MR loop at base temperature, i.e., that did not produced spontaneous IRS at 77 K, did produced IRS under an RF stimulant (either microwave or fast nanosecond range pulses) with a sufficient power. In addition, all these devices produced spontaneous IRS as the temperature was increased with the aforementioned stochastic effects leading to an RTS. Properties of this RTS were comprehensively studied to understand its behavior upon change of temperature and also under an addition of extra stimulate in terms of a microwave signal. It was found that the attempting frequency of RTS always increased as the device temperature is raised. Increase of the power of the optional RF stimulant was found to have the same effect however, it was challenging to isolate STT effects from Joule heating effects caused by the excess RF power to obtain a direct relation on the behavior of RTS on microwave STT.

RTS observed was occurring between multiple steps of the IRS formed in the magnetoresistance loop. Then the question remaining was to identify the nature of the magnetic configuration in between which this RTS occurs. For a perfect free layer without any defects, domains or grains, any skyrmion formed would shrink in a continuous and smooth fashion under an increasing external field leaving a smooth transition trace in the magnetoresistance curve. However, the observed transition from AP-state to P-state always consisted of multiple IRS providing evidence for discontinuous deformation of the magnetic configuration during the process. We conducted micromagnetic simulations to investigate into possible candidates to represent these IRS where possibilities such as coexistence of multiple domains with magnetic bubbles (a topologically trivial curvature from a ferromagnetic state) or a skyrmion was considered. Simulations carried out with grain effects held evidence that

this discontinuous deformation of the magnetic configuration can in fact be a Bloch-skyrmion by itself however pinned to different grain sites. I.e. even in the absence of magnetic domains (that could individually switch back and forth causing RTS), grains in the free layer can act like pinning sites around which the skyrmion favors to stabilized. Even though the simulation provided strong evidence for possible scenario to explain RTS, exact experimentally observed IRS trace is practically impossible to have reproduced in a computer simulation due to infinite number of possibilities for grain signature that also vary from device to device even for same size. This exploration in to RTS and stochastic effects involving skyrmions is expected to serve for the current interest of the research community where ongoing work regarding unconventional computing utilizing MTJs have started to draw great attention.

6.2 Future Directions

Regarding the tri-layer oscillator, linewidth and output power still have room for improvement. A broader linewidth is usually a result of coexistence of multiple oscillation modes. However, for our device we expect the top layer to have more influence on it because, even though it is considered to act as the polarizer for a certain current direction, it is still not pinned as the bottom layer hence is more susceptible to instability leading to moderate dynamics (still less in magnitude compared to those in the middle layer). In such situation, dynamical TMR occurring between top and middle layers can sabotage the main signal (dynamical TMR between bottom and middle layers) as a noise. To eliminate this problem, we suggest a pinning mechanism for the top layer as well where its perpendicular magnetization will be stabilized. This procedure will need a good involvement of material engineering as pinning a perpendicular layer (at room temperature) has still found to be challenging.

Furthermore, to extend the micromagnetic simulation conducted for qualitative comparison (where only one polarizer was considered at a time), a thorough simulation employing the full hybrid-dual-polarizer would facilitate more insight into crucial parameters of the device which can then be optimized for better performance. Continuing to improve performance of this type of a bias-field free STNO offering high frequency, high quality factor and high

output power will have direct impact on and definitely encourage recent innovative efforts made utilizing STNOs for example, energy harvesting of ambient microwave energy [77], human brained inspired neuromorphic computing [88, 89, 90, 91, 92, 93] and much more.

Skyrmion related RTS project reported in this thesis has more timely interest where unconventional computing has started to gain spotlight in the ever increasing demand for computational needs. For the work done, already commercially available MTJs were used where cryogenic temperatures were required to stabilize skyrmions. Taking the cryogenic temperature experiments reported to room temperature would be a significant advancement having an instant impact on skyrmion based application research. Devices used here lack DMI and have shown to stabilize the skyrmion only with the aid of stray- field originating from the fixed layer. In addition to this stray field assist, introduction of a heavy metal, for example Pt, in direct contact with the free layer could drastically enhance the stability of the skyrmion ultimately paving path to stabilized skyrmions in MTJs at room temperature.

In recent past, there has been tremendous interest on employing skyrmion spintronics and skyrmion induced stochastic effects (RTS) to realize, more energy efficient magnetic memory [94, 43, 55, 95, 60, 59, 96], implementing logic gates [61], building non-linear resistive elements for reservoir computing [97], developing synaptic devices for neuromorphic computing [62], microwave energy harvesting [98] and much more. For all these purposes, networking multiple MTJs is essential. In our experimental setup used to investigate the reported work, only one MTJ can be hosted. Modifying the setup to host multiple MTJs and to have them wire bonded together to form networks of different architecture will instantly open up even more opportunities. This modification along with a second generation electromagnet to facilitate higher magnetic fields (at least up to 100 mT) is in the plan for near future.

Bibliography

[1] M. N. Baibich, J. M. Broto, A. Fert, F. N. Van Dau, F. Petroff, P. Etienne, G. Creuzet, A. Friederich, and J. Chazelas, "Giant magnetoresistance of (001) fe/(001) cr magnetic superlattices," *Physical review letters*, vol. 61, no. 21, p. 2472, 1988.

[2] G. Binasch, P. Grünberg, F. Saurenbach, and W. Zinn, "Enhanced magnetoresistance in layered magnetic structures with antiferromagnetic interlayer exchange," *Physical review B*, vol. 39, no. 7, p. 4828, 1989.

[3] C. Chappert, A. Fert, and F. N. Van Dau, "The emergence of spin electronics in data storage," in *Nanoscience And Technology: A Collection of Reviews from Nature Journals*, pp. 147–157, World Scientific, 2010.

[4] D. C. Ralph and M. D. Stiles, "Spin transfer torques," *Journal of Magnetism and Magnetic Materials*, vol. 320, no. 7, pp. 1190–1216, 2008.

[5] S. I. Kiselev, J. Sankey, I. Krivorotov, N. Emley, R. Schoelkopf, R. Buhrman, and D. Ralph, "Microwave oscillations of a nanomagnet driven by a spin-polarized current," *nature*, vol. 425, no. 6956, pp. 380–383, 2003.

[6] I. Krivorotov, N. Emley, J. Sankey, S. Kiselev, D. Ralph, and R. Buhrman, "Time-domain measurements of nanomagnet dynamics driven by spin-transfer torques," *Science*, vol. 307, no. 5707, pp. 228–231, 2005.

[7] K. Everschor, *Current-induced dynamics of chiral magnetic structures: skyrmions, emergent electrodynamics and spin-transfer torques*. PhD thesis, Universität zu Köln, 2012.

[8] R. Wiesendanger, "Nanoscale magnetic skyrmions in metallic films and multilayers: a new twist for spintronics," *Nature Reviews Materials*, vol. 1, no. 7, p. 16044, 2016.

[9] N. Romming, C. Hanneken, M. Menzel, J. E. Bickel, B. Wolter, K. von Bergmann, A. Kubetzka, and R. Wiesendanger, "Writing and deleting single magnetic skyrmions," *Science*, vol. 341, no. 6146, pp. 636–639, 2013.

[10] N. Penthorn, X. Hao, Z. Wang, Y. Huai, and H. Jiang, "Experimental observation of single skyrmion signatures in a magnetic tunnel junction," *Physical review letters*, vol. 122, no. 25, p. 257201, 2019.

[11] W. Skowroński, T. Stobiecki, J. Wrona, G. Reiss, and S. van Dijken, "Zero-field spin torque oscillator based on magnetic tunnel junctions with a tilted cofeb free layer," *Applied Physics Express*, vol. 5, no. 6, p. 063005, 2012.

[12] S. Jiang, M. Ahlberg, S. Chung, A. Houshang, R. Ferreira, P. Freitas, and J. Åkerman, "Magnetodynamics in orthogonal nanocontact spin-torque nano-oscillators based on magnetic tunnel junctions," *Applied Physics Letters*, vol. 115, no. 15, p. 152402, 2019.

[13] O. Boulle, V. Cros, J. Grollier, L. Pereira, C. Deranlot, F. Petroff, G. Faini, J. Barnaś, and A. Fert, "Shaped angular dependence of the spin-transfer torque and microwave generation without magnetic field," *Nature Physics*, vol. 3, no. 7, pp. 492–497, 2007.

[14] Z. Zeng, G. Finocchio, B. Zhang, P. K. Amiri, J. A. Katine, I. N. Krivorotov, Y. Huai, J. Langer, B. Azzerboni, K. L. Wang, *et al.*, "Ultralow-current-density and bias-field-free spin-transfer nano-oscillator," *Scientific reports*, vol. 3, p. 1426, 2013.

[15] A. Dussaux, E. Grimaldi, B. Rache Salles, A. Jenkins, A. Khvalkovskiy, P. Bortolotti, J. Grollier, H. Kubota, A. Fukushima, K. Yakushiji, *et al.*, "Large amplitude spin torque vortex oscillations at zero external field using a perpendicular spin polarizer," *Applied Physics Letters*, vol. 105, no. 2, p. 022404, 2014.

[16] D. Kumar, K. Konishi, N. Kumar, S. Miwa, A. Fukushima, K. Yakushiji, S. Yuasa, H. Kubota, C. Tomy, A. Prabhakar, *et al.*, "Coherent microwave generation by spintronic feedback oscillator," *Scientific reports*, vol. 6, p. 30747, 2016.

[17] D. Houssameddine, U. Ebels, B. Delaët, B. Rodmacq, I. Firastrau, F. Ponthenier, M. Brunet, C. Thirion, J.-P. Michel, L. Prejbeanu-Buda, *et al.*, "Spin-torque oscillator using a perpendicular polarizer and a planar free layer," *Nature materials*, vol. 6, no. 6, pp. 447–453, 2007.

[18] P. Muduli, O. Heinonen, and J. Åkerman, "Bias dependence of perpendicular spin torque and of free-and fixed-layer eigenmodes in mgo-based nanopillars," *Physical Review B*, vol. 83, no. 18, p. 184410, 2011.

[19] A. V. Nazarov, K. Nikolaev, Z. Gao, H. Cho, and D. Song, "Microwave generation in mgo magnetic tunnel junctions due to spin transfer effects," *Journal of Applied Physics*, vol. 103, no. 7, p. 07A503, 2008.

[20] P. Muduli, O. Heinonen, and J. Åkerman, "Intrinsic frequency doubling in a magnetic tunnel junction–based spin torque oscillator," 2011.

[21] A. Fert and I. Campbell, "Two-current conduction in nickel," *Physical Review Letters*, vol. 21, no. 16, p. 1190, 1968.

[22] A. Fert and I. Campbell, "Transport properties of ferromagnetic transition metals," *Le Journal de Physique Colloques*, vol. 32, no. C1, pp. C1–46, 1971.

[23] A. Fert and I. Campbell, "Electrical resistivity of ferromagnetic nickel and iron based alloys," *Journal of Physics F: Metal Physics*, vol. 6, no. 5, p. 849, 1976.

[24] D. Samal and P. A. Kumar, "Giant magnetoresistance," *Resonance*, vol. 13, no. 4, pp. 343–354, 2008.

[25] J. C. Slonczewski *et al.*, "Current-driven excitation of magnetic multilayers," *Journal of Magnetism and Magnetic Materials*, vol. 159, no. 1, p. L1, 1996.

[26] L. Berger, "Emission of spin waves by a magnetic multilayer traversed by a current," *Physical Review B*, vol. 54, no. 13, p. 9353, 1996.

[27] M. Tsoi, A. Jansen, J. Bass, W.-C. Chiang, M. Seck, V. Tsoi, and P. Wyder, "Excitation of a magnetic multilayer by an electric current," *Physical Review Letters*, vol. 80, no. 19, p. 4281, 1998.

[28] E. Myers, D. Ralph, J. Katine, R. Louie, and R. Buhrman, "Current-induced switching of domains in magnetic multilayer devices," *Science*, vol. 285, no. 5429, pp. 867–870, 1999.

[29] J. Katine, F. Albert, R. Buhrman, E. Myers, and D. Ralph, "Current-driven magnetization reversal and spin-wave excitations in co/cu/co pillars," *Physical review letters*, vol. 84, no. 14, p. 3149, 2000.

[30] J. Grollier, V. Cros, A. Hamzic, J.-M. George, H. Jaffrès, A. Fert, G. Faini, J. Ben Youssef, and H. Legall, "Spin-polarized current induced switching in co/cu/co pillars," *Applied Physics Letters*, vol. 78, no. 23, pp. 3663–3665, 2001.

[31] B. Dieny, V. S. Speriosu, S. S. Parkin, B. A. Gurney, D. R. Wilhoit, and D. Mauri, "Giant magnetoresistive in soft ferromagnetic multilayers," *Physical Review B*, vol. 43, no. 1, p. 1297, 1991.

[32] T. Miyazaki and N. Tezuka, "Tmr in al2o3," *J. Magn. Magn. Mater*, vol. 139, p. 231, 1995.

[33] J. S. Moodera, L. R. Kinder, T. M. Wong, and R. Meservey, "Large magnetoresistance at room temperature in ferromagnetic thin film tunnel junctions," *Physical review letters*, vol. 74, no. 16, p. 3273, 1995.

[34] S. Yuasa, T. Nagahama, A. Fukushima, Y. Suzuki, and K. Ando, "Giant room-temperature magnetoresistance in single-crystal fe/mgo/fe magnetic tunnel junctions," *Nature materials*, vol. 3, no. 12, pp. 868–871, 2004.

[35] S. S. Parkin, C. Kaiser, A. Panchula, P. M. Rice, B. Hughes, M. Samant, and S.-H. Yang, "Giant tunnelling magnetoresistance at room temperature with mgo (100) tunnel barriers," *Nature materials*, vol. 3, no. 12, pp. 862–867, 2004.

[36] W. Butler *et al.*, "X.-g. zhang, tc schulthess, and jm maclaren," *Phys. Rev. B https://doi. org/10.1103/PhysRevB*, vol. 63, no. 63, p. 054416, 2001.

[37] J. Mathon and A. Umerski, "Theory of tunneling magnetoresistance of an epitaxial fe/mgo/fe (001) junction," *Physical Review B*, vol. 63, no. 22, p. 220403, 2001.

[38] M. Julliere, "Tunneling between ferromagnetic films," *Physics letters A*, vol. 54, no. 3, pp. 225–226, 1975.

[39] S. Mangin, D. Ravelosona, J. Katine, M. Carey, B. Terris, and E. E. Fullerton, "Current-induced magnetization reversal in nanopillars with perpendicular anisotropy," *Nature materials*, vol. 5, no. 3, pp. 210–215, 2006.

[40] S. Ikeda, K. Miura, H. Yamamoto, K. Mizunuma, H. Gan, M. Endo, S. Kanai, J. Hayakawa, F. Matsukura, and H. Ohno, "A perpendicular-anisotropy cofeb–mgo magnetic tunnel junction," *Nature materials*, vol. 9, no. 9, pp. 721–724, 2010.

[41] S. Mühlbauer, B. Binz, F. Jonietz, C. Pfleiderer, A. Rosch, A. Neubauer, R. Georgii, and P. Böni, "Skyrmion lattice in a chiral magnet," *Science*, vol. 323, no. 5916, pp. 915–919, 2009.

[42] X. Yu, Y. Onose, N. Kanazawa, J. Park, J. Han, Y. Matsui, N. Nagaosa, and Y. Tokura, "Real-space observation of a two-dimensional skyrmion crystal," *Nature*, vol. 465, no. 7300, pp. 901–904, 2010.

[43] D. Bhattacharya, M. M. Al-Rashid, and J. Atulasimha, "Voltage controlled core reversal of fixed magnetic skyrmions without a magnetic field," *Scientific reports*, vol. 6, no. 1, pp. 1–6, 2016.

[44] B. Engel, J. Akerman, B. Butcher, R. Dave, M. DeHerrera, M. Durlam, G. Grynkewich, J. Janesky, S. Pietambaram, N. Rizzo, *et al.*, "A 4-mb toggle mram based on a novel bit and switching method," *IEEE Transactions on Magnetics*, vol. 41, no. 1, pp. 132–136, 2005.

[45] J. Åkerman, "Toward a universal memory," *Science*, vol. 308, no. 5721, pp. 508–510, 2005.

[46] Y. B. Bazaliy, B. Jones, and S.-C. Zhang, "Modification of the landau-lifshitz equation in the presence of a spin-polarized current in colossal-and giant-magnetoresistive materials," *Physical Review B*, vol. 57, no. 6, p. R3213, 1998.

[47] X. Zhu and J.-G. Zhu, "Bias-field-free microwave oscillator driven by perpendicularly polarized spin current," *IEEE Transactions on Magnetics*, vol. 42, no. 10, pp. 2670–2672, 2006.

[48] T. Devolder, A. Meftah, K. Ito, J. Katine, P. Crozat, and C. Chappert, "Spin transfer oscillators emitting microwave in zero applied magnetic field," *Journal of applied physics*, vol. 101, no. 6, p. 063916, 2007.

[49] T. H. R. Skyrme, "A unified field theory of mesons and baryons," *Nuclear Physics*, vol. 31, pp. 556–569, 1962.

[50] N. Nagaosa and Y. Tokura, "Topological properties and dynamics of magnetic skyrmions," *Nature nanotechnology*, vol. 8, no. 12, p. 899, 2013.

[51] S. Rohart, J. Miltat, and A. Thiaville, "Path to collapse for an isolated néel skyrmion," *Physical Review B*, vol. 93, no. 21, p. 214412, 2016.

[52] I. Dzyaloshinsky, "A thermodynamic theory of "weak" ferromagnetism of antiferromagnetics," *Journal of Physics and Chemistry of Solids*, vol. 4, no. 4, pp. 241–255, 1958.

[53] T. Moriya, "Anisotropic superexchange interaction and weak ferromagnetism," *Physical review*, vol. 120, no. 1, p. 91, 1960.

[54] S. Heinze, K. Von Bergmann, M. Menzel, J. Brede, A. Kubetzka, R. Wiesendanger, G. Bihlmayer, and S. Blügel, "Spontaneous atomic-scale magnetic skyrmion lattice in two dimensions," *Nature Physics*, vol. 7, no. 9, pp. 713–718, 2011.

[55] A. Fert, N. Reyren, and V. Cros, "Magnetic skyrmions: advances in physics and potential applications," *Nature Reviews Materials*, vol. 2, no. 7, pp. 1–15, 2017.

[56] F. Jonietz, S. Mühlbauer, C. Pfleiderer, A. Neubauer, W. Münzer, A. Bauer, T. Adams, R. Georgii, P. Böni, R. A. Duine, *et al.*, "Spin transfer torques in mnsi at ultralow current densities," *Science*, vol. 330, no. 6011, pp. 1648–1651, 2010.

[57] J. Zang, M. Mostovoy, J. H. Han, and N. Nagaosa, "Dynamics of skyrmion crystals in metallic thin films," *Physical review letters*, vol. 107, no. 13, p. 136804, 2011.

[58] J. Sampaio, V. Cros, S. Rohart, A. Thiaville, and A. Fert, "Nucleation, stability and current-induced motion of isolated magnetic skyrmions in nanostructures," *Nature nanotechnology*, vol. 8, no. 11, pp. 839–844, 2013.

[59] R. Tomasello, E. Martinez, R. Zivieri, L. Torres, M. Carpentieri, and G. Finocchio, "A strategy for the design of skyrmion racetrack memories," *Scientific reports*, vol. 4, p. 6784, 2014.

[60] W. Kang, Y. Huang, C. Zheng, W. Lv, N. Lei, Y. Zhang, X. Zhang, Y. Zhou, and W. Zhao, "Voltage controlled magnetic skyrmion motion for racetrack memory," *Scientific reports*, vol. 6, p. 23164, 2016.

[61] X. Zhang, M. Ezawa, and Y. Zhou, "Magnetic skyrmion logic gates: conversion, duplication and merging of skyrmions," *Scientific reports*, vol. 5, no. 1, pp. 1–8, 2015.

[62] Y. Huang, W. Kang, X. Zhang, Y. Zhou, and W. Zhao, "Magnetic skyrmion-based synaptic devices," *Nanotechnology*, vol. 28, no. 8, p. 08LT02, 2017.

[63] Y. Dai, H. Wang, P. Tao, T. Yang, W. Ren, and Z. Zhang, "Skyrmion ground state and gyration of skyrmions in magnetic nanodisks without the dzyaloshinsky-moriya interaction," *Physical Review B*, vol. 88, no. 5, p. 054403, 2013.

[64] K. Y. Guslienko, "Skyrmion state stability in magnetic nanodots with perpendicular anisotropy," *IEEE Magnetics Letters*, vol. 6, pp. 1–4, 2015.

[65] J.-V. Kim, F. Garcia-Sanchez, J. Sampaio, C. Moreau-Luchaire, V. Cros, and A. Fert, "Breathing modes of confined skyrmions in ultrathin magnetic dots," *Physical Review B*, vol. 90, no. 6, p. 064410, 2014.

[66] H. Meng and J.-P. Wang, "Spin transfer in nanomagnetic devices with perpendicular anisotropy," *Applied physics letters*, vol. 88, no. 17, p. 172506, 2006.

[67] T. Kishi, H. Yoda, T. Kai, T. Nagase, E. Kitagawa, M. Yoshikawa, K. Nishiyama, T. Daibou, M. Nagamine, M. Amano, *et al.*, "Lower-current and fast switching of a perpendicular tmr for high speed and high density spin-transfer-torque mram," in *2008 IEEE International Electron Devices Meeting*, pp. 1–4, IEEE, 2008.

[68] N. Nishimura, T. Hirai, A. Koganei, T. Ikeda, K. Okano, Y. Sekiguchi, and Y. Osada, "Magnetic tunnel junction device with perpendicular magnetization films for high-density magnetic random access memory," *Journal of applied physics*, vol. 91, no. 8, pp. 5246–5249, 2002.

[69] H. Ohmori, T. Hatori, and S. Nakagawa, "Perpendicular magnetic tunnel junction with tunneling magnetoresistance ratio of 64% using mgo (100) barrier layer prepared at room temperature," *Journal of Applied Physics*, vol. 103, no. 7, p. 07A911, 2008.

[70] M. Yoshikawa, E. Kitagawa, T. Nagase, T. Daibou, M. Nagamine, K. Nishiyama, T. Kishi, and H. Yoda, "Tunnel magnetoresistance over 100% in mgo-based magnetic tunnel junction films with perpendicular magnetic l1 _{0}-fept electrodes," *IEEE Transactions on Magnetics*, vol. 44, no. 11, pp. 2573–2576, 2008.

[71] G. Kim, Y. Sakuraba, M. Oogane, Y. Ando, and T. Miyazaki, "Tunneling magnetoresistance of magnetic tunnel junctions using perpendicular magnetization l 1 0-co pt electrodes," *Applied Physics Letters*, vol. 92, no. 17, p. 172502, 2008.

[72] B. Carvello, C. Ducruet, B. Rodmacq, S. Auffret, E. Gautier, G. Gaudin, and B. Dieny, "Sizable room-temperature magnetoresistance in cobalt based magnetic tunnel junctions with out-of-plane anisotropy," *Applied Physics Letters*, vol. 92, no. 10, p. 102508, 2008.

[73] J.-H. Park, C. Park, T. Jeong, M. T. Moneck, N. T. Nufer, and J.-G. Zhu, "Co/ pt multilayer based magnetic tunnel junctions using perpendicular magnetic anisotropy," *Journal of Applied Physics*, vol. 103, no. 7, p. 07A917, 2008.

[74] K. Mizunuma, S. Ikeda, J. Park, H. Yamamoto, H. Gan, K. Miura, H. Hasegawa, J. Hayakawa, F. Matsukura, and H. Ohno, "Mgo barrier-perpendicular magnetic tunnel junctions with cofe/pd multilayers and ferromagnetic insertion layers," *Applied Physics Letters*, vol. 95, no. 23, p. 232516, 2009.

[75] B. Fang, J. Feng, H. Gan, R. Malmhall, Y. Huai, R. Xiong, H. Wei, X. Han, B. Zhang, and Z. Zeng, "Zero-field spin transfer oscillators based on magnetic tunnel junction having perpendicular polarizer and planar free layer," *AIP Advances*, vol. 6, no. 12, p. 125305, 2016.

[76] B. Fang, M. Carpentieri, X. Hao, H. Jiang, J. A. Katine, I. N. Krivorotov, B. Ocker, J. Langer, K. L. Wang, B. Zhang, *et al.*, "Giant spin-torque diode sensitivity in the absence of bias magnetic field," *Nature communications*, vol. 7, no. 1, pp. 1–7, 2016.

[77] B. Fang, M. Carpentieri, S. Louis, V. Tiberkevich, A. Slavin, I. N. Krivorotov, R. Tomasello, A. Giordano, H. Jiang, J. Cai, *et al.*, "Experimental demonstration of spintronic broadband microwave detectors and their capability for powering nanodevices," *Physical Review Applied*, vol. 11, no. 1, p. 014022, 2019.

[78] T. J. Silva and W. H. Rippard, "Developments in nano-oscillators based upon spin-transfer point-contact devices," *Journal of Magnetism and Magnetic Materials*, vol. 320, no. 7, pp. 1260–1271, 2008.

[79] M. Schäfers, V. Drewello, G. Reiss, A. Thomas, K. Thiel, G. Eilers, M. Münzenberg, H. Schuhmann, and M. Seibt, "Electric breakdown in ultrathin mgo tunnel barrier junctions for spin-transfer torque switching," *Applied Physics Letters*, vol. 95, no. 23, p. 232119, 2009.

[80] H. Kubota, K. Yakushiji, A. Fukushima, S. Tamaru, M. Konoto, T. Nozaki, S. Ishibashi, T. Saruya, S. Yuasa, T. Taniguchi, *et al.*, "Spin-torque oscillator based on magnetic tunnel junction with a perpendicularly magnetized free layer and in-plane magnetized polarizer," *Applied Physics Express*, vol. 6, no. 10, p. 103003, 2013.

[81] C. Kittel, "Int. to solid state physics, 8th edn., maruzen," 2005.

[82] T. Taniguchi, S. Tsunegi, H. Kubota, and H. Imamura, "Self-oscillation in spin torque oscillator stabilized by field-like torque," *Applied Physics Letters*, vol. 104, no. 15, p. 152411, 2014.

[83] Z. Zeng, P. K. Amiri, I. N. Krivorotov, H. Zhao, G. Finocchio, J.-P. Wang, J. A. Katine, Y. Huai, J. Langer, K. Galatsis, *et al.*, "High-power coherent microwave emission from magnetic tunnel junction nano-oscillators with perpendicular anisotropy," *ACS nano*, vol. 6, no. 7, pp. 6115–6121, 2012.

[84] V. Tiberkevich, A. Slavin, and J.-V. Kim, "Microwave power generated by a spin-torque oscillator in the presence of noise," *Applied Physics Letters*, vol. 91, no. 19, p. 192506, 2007.

[85] A. Vansteenkiste, J. Leliaert, M. Dvornik, M. Helsen, F. Garcia-Sanchez, and B. Van Waeyenberge, "The design and verification of mumax3," *AIP advances*, vol. 4, no. 10, p. 107133, 2014.

[86] J. Cai, B. Fang, L. Zhang, W. Lv, B. Zhang, T. Zhou, G. Finocchio, and Z. Zeng, "Voltage-controlled spintronic stochastic neuron based on a magnetic tunnel junction," *Physical Review Applied*, vol. 11, no. 3, p. 034015, 2019.

[87] H. Suto, T. Nagasawa, K. Kudo, K. Mizushima, and R. Sato, "Microwave-assisted switching of a single perpendicular magnetic tunnel junction nanodot," *Applied Physics Express*, vol. 8, no. 2, p. 023001, 2015.

[88] J. Cai, L. Zhang, B. Fang, W. Lv, B. Zhang, G. Finocchio, R. Xiong, S. Liang, and Z. Zeng, "Sparse neuromorphic computing based on spin-torque diodes," *Applied Physics Letters*, vol. 114, no. 19, p. 192402, 2019.

[89] J. Torrejon, M. Riou, F. A. Araujo, S. Tsunegi, G. Khalsa, D. Querlioz, P. Bortolotti, V. Cros, K. Yakushiji, A. Fukushima, *et al.*, "Neuromorphic computing with nanoscale spintronic oscillators," *Nature*, vol. 547, no. 7664, pp. 428–431, 2017.

[90] N. Bindal, A. Kulkarni, G. Singh, and B. K. Kaushik, "Spin based neuromorphic computing," in *Spintronics XII*, vol. 11090, p. 1109045, International Society for Optics and Photonics, 2019.

[91] C. H. Bennett, N. Hassan, X. Hu, J. A. C. Incornvia, J. S. Friedman, and M. J. Marinella, "Semi-supervised learning and inference in domain-wall magnetic tunnel junction (dw-mtj) neural networks," in *Spintronics XII*, vol. 11090, p. 110903I, International Society for Optics and Photonics, 2019.

[92] A. Mondal and A. Srivastava, "Energy-efficient design of mtj-based neural networks with stochastic computing," *ACM Journal on Emerging Technologies in Computing Systems (JETC)*, vol. 16, no. 1, pp. 1–27, 2019.

[93] T. Greenberg Toledo, B. Perach, D. Soudry, and S. Kvatinsky, "Mtj-based hardware synapse design for quantized deep neural networks," *arXiv*, pp. arXiv–1912, 2019.

[94] D. Bhattacharya and J. Atulasimha, "Skyrmion-mediated voltage-controlled switching of ferromagnets for reliable and energy-efficient two-terminal memory," *ACS applied materials & interfaces*, vol. 10, no. 20, pp. 17455–17462, 2018.

[95] K. Everschor-Sitte, J. Masell, R. M. Reeve, and M. Kläui, "Perspective: Magnetic skyrmions—overview of recent progress in an active research field," *Journal of Applied Physics*, vol. 124, no. 24, p. 240901, 2018.

[96] X. Zhang, G. Zhao, H. Fangohr, J. P. Liu, W. Xia, J. Xia, and F. Morvan, "Skyrmion-skyrmion and skyrmion-edge repulsions in skyrmion-based racetrack memory," *Scientific reports*, vol. 5, p. 7643, 2015.

[97] D. Prychynenko, M. Sitte, K. Litzius, B. Krüger, G. Bourianoff, M. Kläui, J. Sinova, and K. Everschor-Sitte, "Magnetic skyrmion as a nonlinear resistive element: a potential building block for reservoir computing," *Physical Review Applied*, vol. 9, no. 1, p. 014034, 2018.

[98] G. Finocchio, M. Ricci, R. Tomasello, A. Giordano, M. Lanuzza, V. Puliafito, P. Burrascano, B. Azzerboni, and M. Carpentieri, "Skyrmion based microwave detectors and harvesting," *Applied Physics Letters*, vol. 107, no. 26, p. 262401, 2015.